UNIVERSIDADE FEDERAL DO RIO GRANDE DO SUL
ESCOLA DE ENGENHARIA
PROGRAMA DE PÓS-GRADUAÇÃO EM ENGENHARIA ELÉTRICA

THALES EXENBERGER BECKER

ELECTRICAL CHARACTERIZATION AND MODELING OF RANDOM TELEGRAPH NOISE IN MIM-LIKE RESISTIVE SWITCHING DEVICES

Porto Alegre
2022

THALES EXENBERGER BECKER

ELECTRICAL CHARACTERIZATION AND MODELING OF RANDOM TELEGRAPH NOISE IN MIM-LIKE RESISTIVE SWITCHING DEVICES

Thesis presented to Programa de Pós-Graduação em Engenharia Elétrica of Universidade Federal do Rio Grande do Sul in partial fulfillment of the requirements for the degree of Doctor in Electrical Engineering.
Area: Computer Engineering

ADVISOR: Prof. Dr. Gilson Inácio Wirth

Porto Alegre
2022

THALES EXENBERGER BECKER

ELECTRICAL CHARACTERIZATION AND MODELING OF RANDOM TELEGRAPH NOISE IN MIM-LIKE RESISTIVE SWITCHING DEVICES

This thesis was considered adequate for the awarding of the degree of Doctor in Electrical Engineering and approved in its final form by the Advisor and the Examination Committee.

Advisor: _____
Prof. Dr. Gilson Inácio Wirth, UFRGS
Doutor pela Universitaet Dortmund – Dortmund, Alemanha)

Examination Committee:

Prof. Dr. Marcelo Antonio Pavanello, FEI
Doutor pela Universidade de São Paulo – São Paulo, Brasil

Prof. Dr. Ivan Müller, UFRGS
Doutor pela Universidade Federal do Rio Grande do Sul – Porto Alegre, Brasil

Prof. Dr. Fernanda Gusmão de Lima Kastensmidt, UFRGS
Doutora pela Universidade Federal do Rio Grande do Sul – Porto Alegre, Brasil

Coordinator of PPGEE: _____
Prof. Dr. Sérgio Haffner

Porto Alegre, March 2022.

DEDICATÓRIA

Dedico este trabalho a minha esposa, Carolina Möller Neves, em especial pelo suporte e motivação nos momentos difíceis e ao nosso bebê que está por vir. Dedico também aos meus pais e irmãos, em especial pela dedicação que dispenderam a mim durante toda a minha formação.

AGRADECIMENTOS

Ao Programa de Pós-Graduação em Engenharia Elétrica, PPGEE, pela oportunidade de realização de trabalhos em minha área de pesquisa.

Ao meu Orientador, Gilson Inácio Wirth e aos meus colegas do Laprot pelo auxílio nas tarefas desenvolvidas ao longo da minha pesquisa.

Ao CNPQ pela provisão da bolsa de doutorado.

ABSTRACT

Metal-insulator-metal (MIM-like) resistive switching (RS) devices have been increasingly studied for several modern and traditional applications, such as information storage, stochastic computing, and bio-inspired computing. The Random Telegraph Noise (RTN) phenomenon is an important metric regarding the robustness of MIM-like RS devices, and it is intrinsic to any dielectric with defects (traps). In this work, a novel model for anomalous RTN (aRTN) is presented, accounting for the existence of coupling effect between multiple traps regarding current amplitude deviation. It was determined that the contribution of one defect to the current deviation leading to RTN is dependent on the state (i.e., occupied or vacant) of other defects, indicating the presence of coupling effects. A model is proposed to the describe the behavior at low reading voltages (~ 0.1 V) for both low-resistance state (LRS) and high-resistance state (HRS). The model can be applied to help understanding the dynamics of filament distribution and trapping/de-trapping activity. Additionally, a novel observation of trap acitivity is presented, which results in giant random conductance fluctuations, up to 3 orders of mangnitude, resembling RTN in RS devices based on TiO_2, HfO_2 and hexagonal boron nitride (h-BN) under reading voltages. Considering this behavior, presented for three different switching materials, we show that this is a quite general phenomenon and that this significant on/off ratio, in reading conditions, is reproducible and beneficial to ensure recognition of device's two-state in applications such as stochastic computing integrated circuits (ICs). These events were reproducible for all the aforementioned RS device types in sequential measurements and under different bias conditions.

Keywords: Resistive Switching, Reliability, Random Telegraph Noise, Trap Coupling Model, Giant RTN.

RESUMO

Dispositivos de comutação resistiva (RS) estruturados em uma célula do tipo MIM (Metal Isolante Metal) são cada vez mais estudados para diversas aplicações como, por exemplo, no armazenamento de informações, na computação estocástica e na computação inspirada na atividade cerebral. Isso se deve à capacidade desses dispositivos de superar em performance e eficiência os dispositivos atuais, apesar dos desafios relacionados à confiabilidade. O *Random Telegraph Noise* é um parâmetro relevante para avaliar a robustez de dispositivos memresistivos, relativos à atividade de defeitos (armadilhas). Neste trabalho, um novo modelo para RTN anômalo (aRTN) é apresentado, indicando o acoplamento na amplitude da flutuação de corrente produzida por diferentes armadilhas no mesmo dispositivo. Determina-se que a contribuição de um defeito para o desvio de corrente que leva ao RTN depende do estado (ocupado ou vago) de outra armadilha, caracterizando, dessa forma, o efeito de acoplamento. Propõe-se um modelo elétrico capaz de descrever esse fenômeno para operação de leitura do dispositivo ($\sim$ 0,1 V). Esse modelo pode ser aplicado para melhor compreensão da dinâmica da distribuição dos filamentos na célula e da atividade e interação das armadilhas presentes. Além disso, uma nova observação da atividade de defeitos é apresentada: verificou-se, experimentalmente e em condição de leitura do estado, flutuações significativas na condutância desses dispositivos, que alcançam até 3 ordens de magnitude, semelhantes ao RTNs. Os experimentos foram feitos em dispositivos RS baseados em dielétricos compostos por TiO_2, HfO_2 e nitreto de boro hexagonal (h-BN). Considerando este comportamento, apresentado para três diferentes materiais de comutação resistiva, verifica-se que este é um fenômeno bastante recorrente e que a significativa relação entre os estados (LRS/HRS), durante a operação de leitura, é reproduzível e benéfica para assegurar o reconhecimento de estados em aplicações como circuitos integrados de computação estocástica (ICs). Esses eventos se mostram reproduzíveis para todos os tipos de dispositivos RS acima mencionados, em medições sequenciais e sob diferentes condições de polarização de leitura.

Palavras-chave: Resistive Switching, Reliability, Random Telegraph Noise, Trap Coupling Model, Giant RTN.

LIST OF FIGURES

LIST OF TABLES

LIST OF ABBREVIATIONS

aRTN	Anomalous Random Telegraph Noise
CBRAM	Conductive Bridge Ramdom Access Memory
CC	Current Compliance
CF	Conductive filament
DRAM	Dynamic Random Access Memory
ECM	Electrochemical Metallization
EELS	Eléctron Energy-Loss Spectroscopy
FHMM	Factorial Hidden Markov Model
FINFET	Fin Field Effect Transistor
h-BN	Hexagonal Boron Nitride
HfO_2	Hafnium Dioxide
HRS	High Resistance State
LRS	Low Resistance State
MIM	Metal Insulator Metal
MOSFET	Metal Oxide Semiconductor Field Effect Transistor
mRTN	Mutant Random Telegraph Noise
Ni	Nickel
RTN	Random Telegraph Noise
RS	Resistive Switching
RRAM	Resistive Ramdom Access Memory
SRAM	Static Random Access Memory
TiO_2	Titanium Dioxide
tRTN	Temporary Random Telegraph Noise
VCM	Valence Change Memories
Vo	Oxigen Vacancy

LIST OF SYMBOLS

K	Boltzmann's Constant
n	Carrier Density
S_{UF}	Conductive Filament Cross-Section
S_{WF}	Conductive Filament Cross-Section in Weak Filaments
D	Conductive Filament Diameter
L	Conductive Filament Length
ϵ	Conductive Filament Dielectric Constant
ΔI	Current Switching Amplitude
λ_D	Debye Length
q	Elementary Charge
Ω	Ohms
ΔR	Resistance Switching Amplitude
T	Temperature
τ_c	Trap Average Time Required to Capture
τ_e	Trap Average Time Required to Emit
ρ	The Filament Bulk Resistivity

CONTENTS

1 INTRODUCTION

Modern, fast and energy-efficient integrated circuits have been primarily achieved by device dimensional scaling. It has been driving information processing technology into a broadening spectrum of new applications through increased performance and complexity. However, as we approache fundamental physical limits, new technologies and, essentially, new computing principles are explored to support the increasing necessity of data storage and processing. Therefore, through new concepts, researchers and industry plan to extend the scaling trend of integrated circuit technology (ZIDAN; STRACHAN; LU, 2018; ASWATHY; SIVAMANGAI, 2021).

In this context, resistive switching (RS) systems have received much attention in recent years due to their simple structure, high integration density, and outstanding performance. According to INTERNATIONAL ROADMAP FOR DEVICES AND SYSTEMS: BEYOND CMOS (2020), the best parameters designed and demonstrated for this technology are: Feature size: sub-5 nm (demonstrated in LI *et al.* (2014); Retention time: $>$ 10 years (demonstrated in JAMESON *et al.* (2013) by monitoring the cell state for 10000 hours at 200 Celsius); Write cycles: 10^{12} (demonstrated in LEE *et al.* (2011)); Read current: $\sim$100 pA (demonstrated in ZHOU *et al.* (2016)). For instance, metal-insulator-metal (MIM)-like RS devices as Resistive Random Access Memory (RRAM) are faster when compared to hard disk drives and flash memory, while enabling higher density, nonvolatility, and lower cost than static random access memory (SRAM) and dynamic random access memory (DRAM), (ZIDAN; STRACHAN; LU, 2018). Hence, MIM-like RS devices are being studied exhaustively for multiple applications such as information storage and bio-inspired computing, (ZIDAN; STRACHAN; LU, 2018; SHI *et al.*, 2018). Also, they can be employed for the fabrication of stochastic computing integrated circuits (ICs). As an example, random telegraph noise (RTN) signals produced by MIM-like devices under DC bias conditions have been employed in true random generators and physically unclonable functions for advanced encryption systems (PUGLISI *et al.*, 2018).

The most promising RS systems are made of dense crossbar arrays of (MIM) cells, and their conductance can be set at different stable levels by generating defects in the structure of the insulator via electrical stimuli (LANZA *et al.*, 2019). The principle of MIM-like RS

devices is discussed in chapter 2, where the resistive switching phenomenon is detailed, i.e., the property shown by some materials of cyclically changing their electrical resistivity between different stable levels when exposed to specific electrical stresses. Hence, in the fundamental MIM cell there are two well-defined states that may store the information: a Low Resistance State (LRS), and a High Resistance State (HRS). These different, stable, conduction states are achived through specific electrical stress due to the resistance switching phenomenon, discussed in chapter 2. Moreover, a discussion is presented on the physical mechanisms responsible for driving the switching phenomenon in different materials (namely RS medium, which is typically an insulator) showing the RS capability.

A key concern for MIM-like RS devices is the read noise due to the structural, chemical, and electrical modifications at the conductive filaments (CF) formed in the insulator (AMBROGIO *et al.*, 2014). Trapping/emission of electrical charges into/from local defects can produce uncontrollable (i.e., unwanted) current fluctuations in such devices, which are often referred to as random telegraph noise (RTN), i.e., an RTN-like read current instability. Therefore, understanding the effect of RTN on the electrical characteristics of MIM-like RS devices is relevant for the development of this technology (AMBROGIO *et al.*, 2014; GUAN; LI, 2016). Also, even though noise has a considerable impact on the reliability of circuits, it can also be used as a tool to assess the presence of defects and their impact on materials and device's performance (VANDAMME, 2003). In chapter 3, the fundamentals and the different measured RTN patterns shown in the literature are presented. The discussion is focused on MIM-like RS devices to elucidate how this reading instability is modeled for both operation states: HRS and LRS.

The capture and emission of charge carriers by traps, or commonly called defects, is described as the origin of the RTN mechanism, (KIRTON; UREN, 1989). RTN signals are manifested by the random variation of a detectable electrical quantity (most commonly by electrical current) between two well-defined discrete levels (states). A multilevel RTN, 2^N levels, where N is the number of active traps, is defined as the superposition of multiple independent two-level RTN signals, and each of them is related to a specific trap (GONG *et al.*, 2018; PUGLISI; PAVAN, 2013).

Additionally, experimental RTN signals measured in MIM-like RS devices have shown anomalous RTN (aRTN) behavior, i. e., RTN that cannot be modeled as the simple sum of independent two-level RTN signals, which also includes a temporary conductance fluctuation (tRTN) (WANG *et al.*, 2018). Sometimes, aRTN signals produced by different defects may present certain degree of correlation, but this behavior is still far from being completely understood (PUGLISI *et al.*, 2016). The observation of aRTN is widely discussed in the literature and has already been addressed in the context of traditional MOSFETs (GRASSER, 2012), whose study describes the case where the same defect has different charge states, which means that its statistical parameters can vary temporarily and randomly. This characteritic is named as metastable state of a trap. Also, experimen-

tal observations show a coupling effect between traps, resulting in aRTN in MOSFETs and FINFETs devices (WANG *et al.*, 2018; ZHANG *et al.*, 2018). As defect coupling has been widely observed and reported in the literature, the purpose of this work is to provide a model to account for aRTN and the effects of defect coupling. Also, a review of substiantial conductance variations at reading voltages is presented. In some cases, conductance variations of up to 50 $\%$ were recorded (SONI *et al.*, 2010). These atypical RTN patterns are presented in Chapter 4.

The primary methodologies for MIM-like RS device characterization are described in chapter 5, as well as the proper methods to display the obtained data. It is important to note that operating conditions, particularly the reading voltage and the temperature, modify the properties of RTNs. Since RTN parameters are unkown prior to measurement, the sampling window and measurement resolution are defined throughout the characterization, and cannot be predetermined (LANZA *et al.*, 2019). The traditional analysis of a typical multilevel RTN is made by a Factorial Hidden Markov Model (FHMM) algorithm (PUGLISI; PAVAN, 2013), which will be presented.

In this work, the experimental results exhibited evident defect coupling effects. The measurements presented in this study are not explained by the traditional, 2-level RTN theories, or by the multi-level RTN superposition technique. The goal is then to present the simplest possible model that captures the essence of defect coupling in a percolation path. It is particularly useful and instructional that the minimalist model correctly reproduces the observations and many common data in the literature. We have determined that the current deviation of one component of the RTN signal is also dependent on the state in which other components are found, indicating the presence of coupling effects. To account for this behavior, a simple, yet effective, model is proposed. This trap coupling model is presented in chapter 6 and compared to experimental current vs time (I-t) plots collected in Ni/TiO_2/Au, Ni/HfO_2/Au and Ni/h-BN/Au cross-point devices. We also investigate aRTN with coupled amplitude, i.e., when the amplitude of one trap is affected by the state of another. If the trap amplitude increases, we consider that positive coupling effect is taking place; if the amplitude decreases, we consider it to be negative coupling effect. Similar behavior of aRTN has been reported in the context of *MOSFET* and *FinFET* devices (WANG *et al.*, 2018; ZHANG *et al.*, 2018). As defect coupling has been widely observed and discussed in the literature, this work is relevant to provide insight into the conduction mechanism and its interplay with defects (traps). The devices were fabricated by a partner group at the Nanotechnology and NanoElectronics Laboratory of Soochow University, China.

Additionally, this work explored the giant RTN at reading operation, which were stable in the aforementioned cross-point devices. This type of electrical signal may be especially useful for RTN-based ICs, as the high conductance on/off ratio ($\sim$3 orders of magnitude) facilitates the recognition of each state. We also modeled this behavior, in chap-

ter 7, assuming the surface-relaxation model in narrow conductive filaments (IELMINI; NARDI; CAGLI, 2010; AMBROGIO *et al.*, 2014; PUGLISI *et al.*, 2018). Our findings represent a big step towards the manufacturing of stochastic ICs based on RTN signals, since this behavior is reproducible for three different dielectrics, TiO_2, HfO_2, and h-BN and in multiple devices, having important implications in the field of post-silicon electronics.

Finally, the closing remarks of this work are presented in chapter 8.

2 RESISTIVE SWITCHING

2.1 Fundamentals

Resistive Switching (RS) MIM-cells are very promising devices considering the post-CMOS scenario. According to INTERNATIONAL ROADMAP FOR DEVICES AND SYSTEMS: BEYOND CMOS (2020), the best parameters designed and demonstrated for this technology are: Feature size: sub-5 nm (demonstrated in LI *et al.* (2014); Retention time: $>$ 10 years (demonstrated in JAMESON *et al.* (2013) by monitoring the cell state for 10000 hours at 200 Celsius); Write cycles: 10^{12} (demonstrated in LEE *et al.* (2011)); Read current: $\sim$100 pA (demonstrated in ZHOU *et al.* (2016)). The main challenge is to fabricate an unique cell that presents all those parameters regarding variability and reliability issues.

In nanoelectronics, Resistive switching (RS) is the property shown by some materials of cyclically changing their electrical resistivity between different stable levels when exposed to specific electrical stresses in a nonvolatile manner (IELMINI; WASER, 2015). The nonvolatility is achieved when the resistance change is retained for a sufficiently long retention time after the absence of the electrical stimulus that has imposed it. Devices with such capability are commonly called memristors, resistive memory, MIM-like RS devices (Metal/Insulator/Metal), or RRAM (Resistive Ramdom Access Memories), (IELMINI; WASER, 2015). Most studies on RS materials and devices ($\sim 95\%$) reported stable RS between two resistance states, namely, high resistance state (HRS) or OFF state and low resistance state (LRS) or ON state. In addition to the traditional states, some materials and devices show the ability to present multiple stable and programmable their electrical quantity (state 1, state 2, state 3, etc.), which may be used for multilevel information processing applications (LANZA *et al.*, 2019; QI *et al.*, 2012). However, correctly distinguishing each conductive state in multilevel devices is a very challenging task due to the inherent variability of the device electrical magnitudes (shifts of voltage and current), which becomes even harder when studying a multitude of samples (LANZA *et al.*, 2019).

To implement a MIM-like RS device, the material showing the RS property (namely RS medium) is typically an insulator and should be placed between two electrodes, named

top and bottom (usually in the vertical orientation) (LANZA *et al.*, 2019). The typical structure of these MIM cells is presented in Figure 1.

Figure 1 – Typical MIM-like RS device structure in stacked layers.

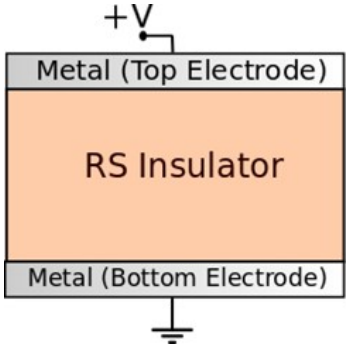

Source: The Author.

Nowadays, there are a multitude of materials that present the RS capability, and that can play the role of the RS medium. The following materais, however, stand out: the transition metal oxides, such as HfO_x, NiO_x, and TiO_x; the chalcogens such as Cu_2S (chalcocite); and 2-D materials such as the Hexagonal Boron Nitride (h-BN), among others (WONG *et al.*, 2012; SAKAMOTO *et al.*, 2003; SHI *et al.*, 2018). The metallic electrodes of MIM-like RS devices, produced in the laboratory, are usually composed of platinum (Pt), gold (Au), silver (Ag), titanium (Ti), nickel (Ni), and copper (Cu) (LANZA *et al.*, 2019; CHEN *et al.*, 2015) although TaN and TiN are preferred in the industry (Chen et al., 2015). These layers must be deposited on a substrate of low roughness, in order to minimize the variability between samples. Typically, this characteristic is obtained from an oxidized silicon wafer, which comprises of thin ($\sim$100 nm) SiO_2 layer with low roughness, and can be obtained at a low cost. The bottom electrode is deposited on the dielectric, and nobel metals, such as gold (Au), are the preferred choice, especially at universities and laboratories in which temperature and humidity control is limited. The interaction of the cell with the environment can lead to a rapid oxidation of low-cost metals such as copper (Cu) and titanium (Ti). Top electrodes are typically comprised of active metals, as Copper and Nickel, as these materials allow, through the action of an electric field, the diffusion of metal ions that form a conductive bridge between the electrodes, and thus collaborate with the resistive switching mechanisms, discussed in the following subsections (LANZA *et al.*, 2019).

There are different operating modes to establish the RS behavior depending on material and methods. Most MIM-like RS devices reported in the literature operate in the bipolar resistive switching mode (Figure 2a). From the HRS, a conductive path is formed when the applied voltage (V = V_{SET}) surpasses the threshold voltage (V_{th1}), which leads the cell to the LRS. This change of HRS to LRS is called SET operation (write state 1). To optimize the process and to avoid any damage, a current compliance (CC) is defined

during the SET transition. In bipolar devices, the HRS is restored when a voltage signal (V = V_{RESET}) of opposite polarity and absolute value larger than a threshold limit (V_{th2}) is applied. This change of LRS to HRS is named RESET transition (write state 0). Some devices operate in a unipolar mode, Figure 2b, characterized by the fact that all write and read operations can be performed with only one voltage polarity. Starting in the HRS, a conductive path is formed when the applied voltage (V = V_{SET}) surpasses the threshold voltage (V_{th1}), with a LRS current compliance (CC). This CC is released in the RESET process and when $V_{RESET} > V_{th2}$ the current can exceed the CC value, which leads the device to changing back into the HRS. The read operation is often performed at a small voltage for both operation modes, V_{rd}, $\sim$ 0.1 V. Usually, the cells write process take place by the sweep curve (characteristic I-V curve), Figure 2a and 2b on the left side, or by the application of voltage pulses over time, Figure 2a and 2b on the right side (IELMINI; NARDI; CAGLI, 2010; GUPTA *et al.*, 2020). It is also important to remark that these cells often require a forming process before stable resistive switching can be achieved, i. e., the conductive filament formation usually involves voltages higher than normal switching conditions (CHEN, 2013).

Figure 2 – Most common operating modes of MIM-like RS devices: (a) Bipolar and (b) Unipolar. This curves represent non-volatile devices.

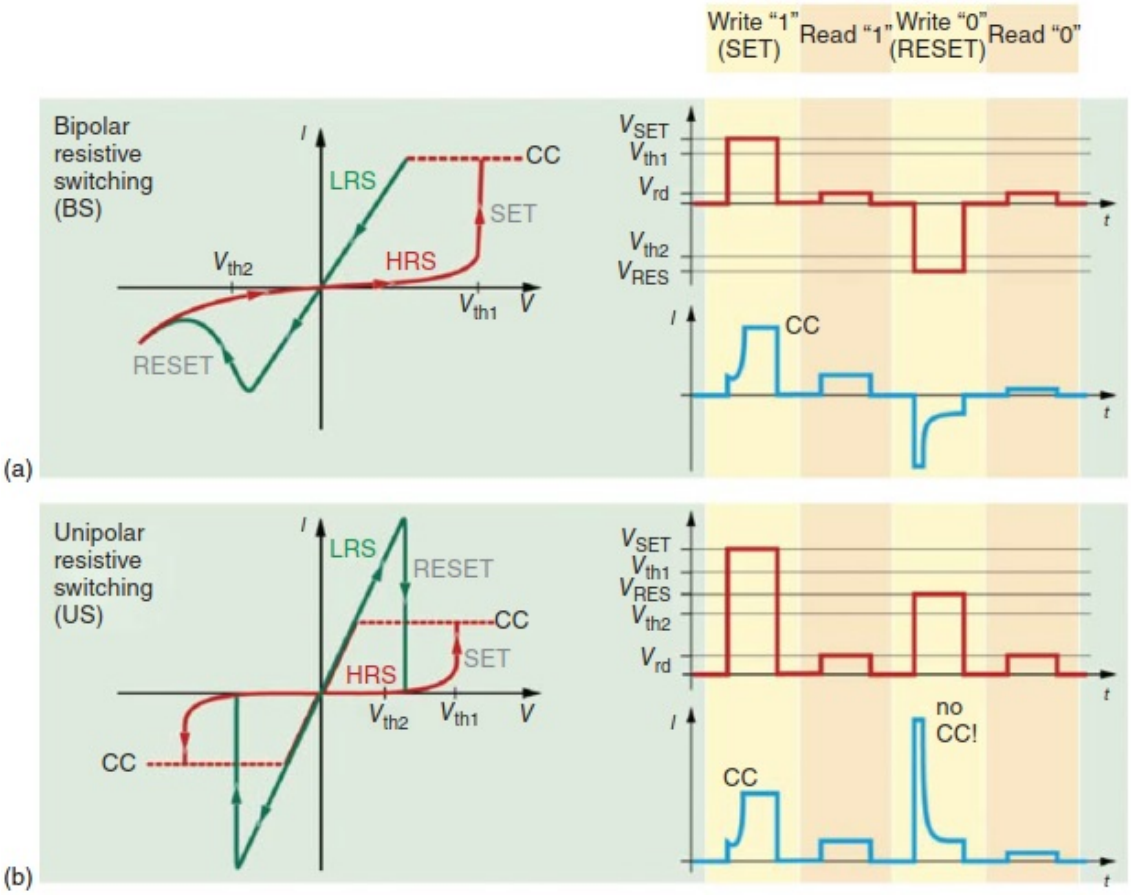

Source: (IELMINI; WASER, 2015).

In materials such as HfO_2 and NiO_2 the writing operations (SET and RESET of the sample) can be perfomed using voltages of both polarities, which characterizes a non-polar process, Figure 3a, (Gupta et al., 2019). Most devices have a non-volatile behavior (i. e., long state retention times). However, certain MIM-like RS cells have a volatile behavior, meaning state retention times ranging from microseconds (μs) up to a few seconds. This usually happens when a low current compliance (CC) is imposed during the SET writing procedure (SHI *et al.*, 2017). This volatile behavior is also observed in the $I \times V$ characteristic curve, shown in Figure 3b. Note that the HRS is restored when the voltage is reduced below a certain voltage magnitude, smaller than the SET write voltage. This behavior was already identified in h-BN based devices and is described in the literature as a threshold RS (LANZA *et al.*, 2019; SHI *et al.*, 2017).

Figure 3 – Particular operation modes of MIM-like RS devices: (a) non-polar and (b) threshold RS.

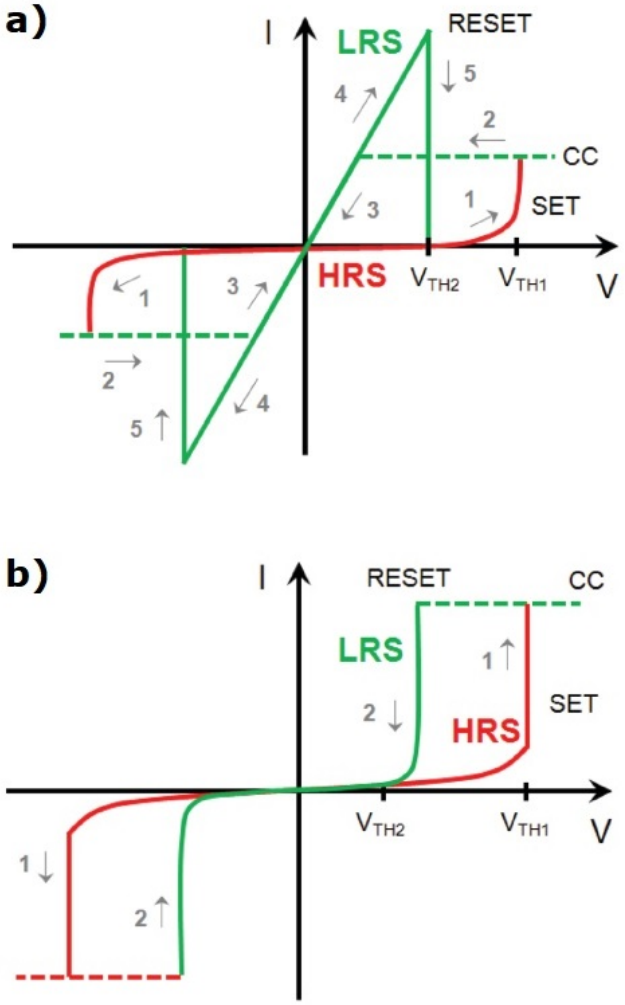

Source: Adapted from LANZA *et al.* (2019).

2.2 Conductive filaments (CF): formation and dissolution

A microscopic analysis of MIM-like RS devices demonstrates that the electrodes and, particularly the RS medium can participate in the resistive switching process. The most common resistance switching mechanism is a result of the formation and dissolution of a single conducting filament (IELMINI; WASER, 2015). A much rare mechanism is the area-proportional switching, that is, a switching process over the entire cross section of the MIM cell. Two major types of MIM-like RS devices exist: i) conducting bridge-based RAM (CBRAM), which involves metal cation motion in a electrochemical metallization (ECM) process and ii) metal-oxide-based RAMs (OxRAM), which involve oxygen ions/vacancies motion in the so-called Valence Change Memories (VCM) (INTERNATIONAL ROADMAP FOR DEVICES AND SYSTEMS: BEYOND CMOS, 2021). These different MIM-like RS devices are further discussed in the following subsections.

2.2.1 Electrochemical Metallization (ECM)

The basic ECM cell is a metal-insulator-metal (MIM system). The cell consists of an electrode made from an electrochemically active metal, such as Ag, Cu, or Ni; an electrochemically inert counter electrode, such as Pt, Ir, W, etc; and a RS medium. Figure 4 illustrates the principle of operation of an ECM memory cell during an entire I-V switching cycle (VALOV *et al.*, 2011). During this cycle, the filament is formed and then disrupted. The HRS is the natural state of the sample (Figure 4(A)), when no CF is established. The SET takes place as an increasing and positive voltage applied to the active electrode (top). Using silver as an example of active electrode, the process of silver anodic dissolution starts, resulting in the reaction $Ag \rightarrow Ag^{+} + e^{-}$ (Figure 4(B)). After that, the cation Ag^{+} drifts towards the inert electrode (Pt) due to the presence of an electric field where it is reduced, according to the cathodic deposition reaction: $Ag^{+} + e^{-} \rightarrow Ag$ (Figure 4(C)). After the metal filament has grown sufficiently to make an electronic contact to the opposite Ag electrode, the cells is assumed to switch to its LRS. (Figure 4(D)). The device holds the LRS-state until a sufficiently large voltage of opposite polarity is applied, resulting in electrochemical dissolution of the metal filment (Figure 4(E)), re-setting the cell to its HRS (RESET) (Figure 4(A)). Note that the voltage required to set the same sample in the subsequent cycles is usually smaller than the first one, as in such cases the filament it is already partially formed, (VALOV *et al.*, 2011).

2.2.2 Valence Change Memories (VCM)

Cells composed of Transition Metal Oxide (TMO) have the characteristic of bipolar RS, even when no injection of metal ions in the dielectric is observed. Unlike the ECM mechanism, in which the migration of metallic cations is observed, the VCM process is associated to the movement of anions, such as oxygen ions (or by their respective

Figure 4 – Steps to SET ((A) → (D)) and RESET (D → E) an electrochemical metallization memory (ECM) cell based on an active electrode (Ag) and an inert counter electrode (Pt).

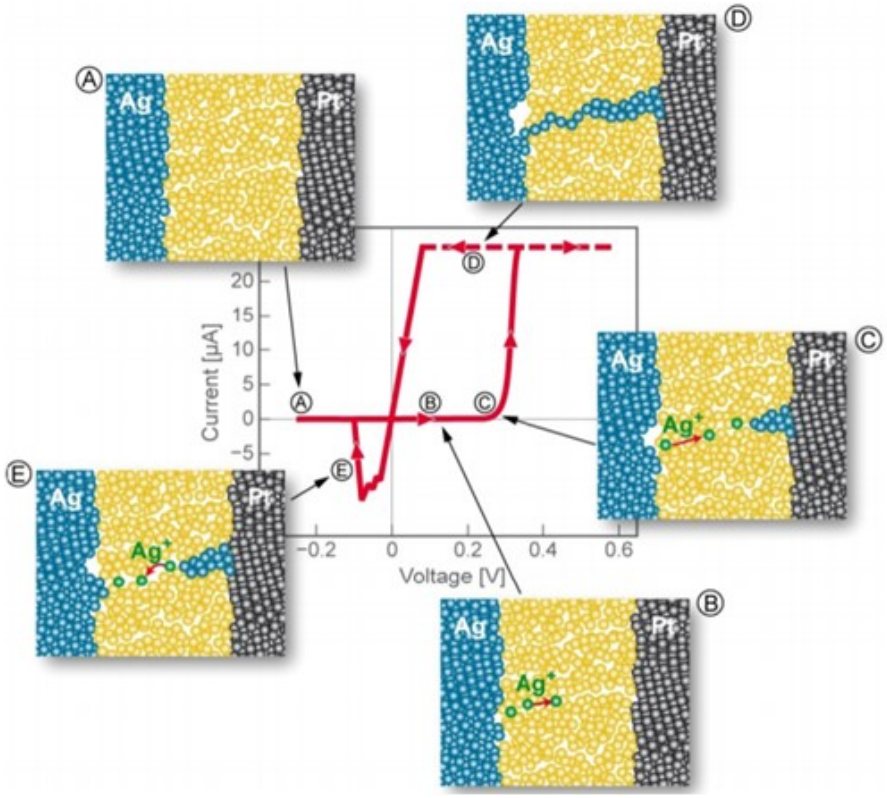

Source: (VALOV *et al.*, 2011).

positively charged oxygen vacancies). Metal oxides, such as TiO_2 and HfO_2, have this characteristic. It is important to point out that the migration of cations in RS medium composed of TiO_2 and HfO_2 is also possible, and can contribute along with oxygen vacancies in the RS process (WEDIG *et al.*, 2016). This characteristic was also verified in Ti/h-BN/Cu samples, which are similar, except for the metallic electrodes, to those characterized in this work (SHI *et al.*, 2018). In Figure 5, an analysis via electron energy-loss spectroscopy (EELS) is presented to compare the chemical species present in a region of the sample without (on the left) and with (on the right) the presence of a formed CF. It is verified by the chemical species present in h-BN samples that the formation of the CF occurs due to a significant migration of boron (B) towards the titanium electrode, and also from the penetration of titanium towards the h-BN stack. It is noteworthy that the SET process occurred by applying a positive voltage to the titanium electrode keeping the Cu electrode grounded (SHI *et al.*, 2018).

Figure 5 – EELS analysis in Ti/h-BN/Cu cell in regions without (left) and with (right) formed conductive filaments.

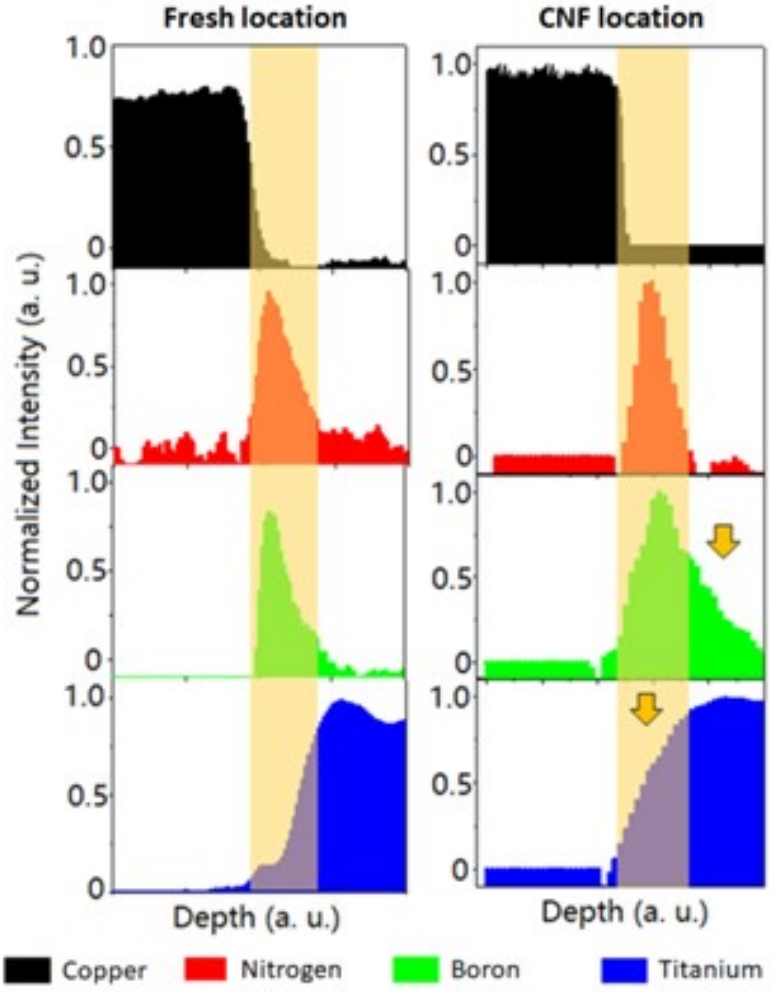

Source: (SHI *et al.*, 2018).

Figure 6 (SHI *et al.*, 2018) summarizes the aforementioned mechanisms of growing

conductive filaments in MIM-like RS devices: on the left, in a Cu/HfO_2/Pt cell, the penetration of copper metallic ions in the dielectric medium dominates the process (as in the ECM cells). In the center, in a Pt/HfO_2/Pt cell, the filament is formed by the migration of oxygen ions and the consequent generation of oxygen vacancies in the dielectric medium (as in the VCM cells). Finally, on the right, in a Ti/h-BN/Cu device, the combination of both effects is verified, as both the movement of Boron ions and the consequent generation of Boron vacancies, as well as the migration of Ti ions form the filament are observed. The mechanisms involved in TiO_2 and HfO_2 cells are very similar, since in both cells the oxygen vacancies are the defects that participate in the formation/dissolution of the filament.

Figure 6 – Different MIM-like RS devices and the correspondig mechanisms to form and dissolve conductive filaments depending on the materials of the cell.

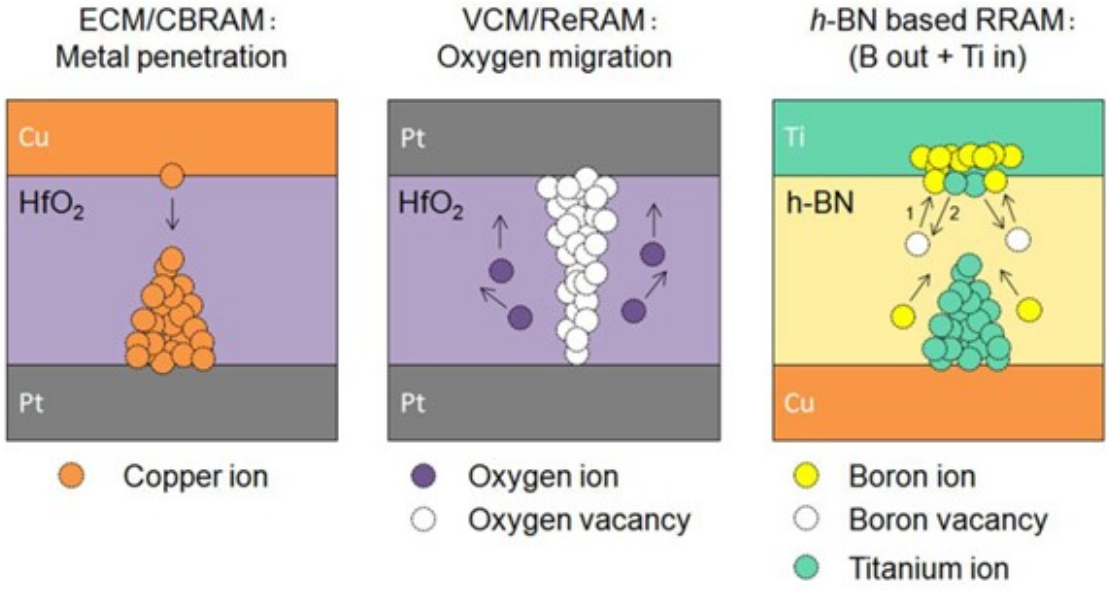

Source: (SHI *et al.*, 2018).

3 RANDOM TELGRAPH NOISE

3.1 RTN Fundamentals

Random telegraph noise in MOS transistors has been widely reported and extensively studied due to its important effects on IC reliability (SIMOEN; CLAEYS, 2016). Novel technologies, however, lag behind both in characterization and modeling of RTN (PUGLISI *et al.*, 2017). In the context of MOSFETs, in its simplest form, RTN consists of the temporal switching of the drain current ΔI_D between two well-defined levels, as illustrated in Figure 7. The discrete nature of the RTN fluctuations has been understood in terms of trapping of a single electron (in nMOSFET) or hole (in pMOSFET) by a defect at the Si/SiO_2 interface or in the oxide next to the inversion layer, also called border traps (FLEETWOOD, 1992) or switching oxide traps (OLDHAM, 2004) . Also, it has been demonstrated that the 1/f noise in MOSFETs is caused by the summation of many RTNs, with different trapping/de-trapping time constants first describe by MCWHORTER *et al.* (1955) and also discussed in KIRTON; UREN (1989) and SIMOEN; CLAEYS (2016).

The RTN signal generated by a single trap is generally expressed by the random variation of a measurable electrical quantity (e.g., current, voltage, conductance) between two well-defined discrete levels (2 states). In the context of trapping and de-trapping of charge carriers by defects, the RTN is statistically described by three parameters: the amplitude fluctuation of the electrical quantity, usually ΔI (current switching amplitude), and the average time required to emit (τ_e) and capture (τ_c) a charge carrier, as illustrated in Figure 8, (PUGLISI *et al.*, 2017). According to (KIRTON; UREN, 1989), it can be demonstrated that the times spent at the high and low current states (τ_e and τ_c, respectively) are exponentially distributed, resulting in a Poisson process related to the stochastic nature of the trap. Figure 9 exemplifies a typical frequency histogram of times to emit measured for a single trap (KIRTON; UREN, 1989).

Several works in the literature (PUGLISI *et al.*, 2017; GONG *et al.*, 2018; PUGLISI; PAVAN, 2013) also report the observation of multilevel RTN signals, which are definined as the superposition of multiple independent two-level RTN signals, each produced by a different trap. A multilevel RTN presents 2^N levels, where N is the number of active traps.

Figure 7 – Random telegraph signals in small MOSFET measured at the indicated gate voltages.

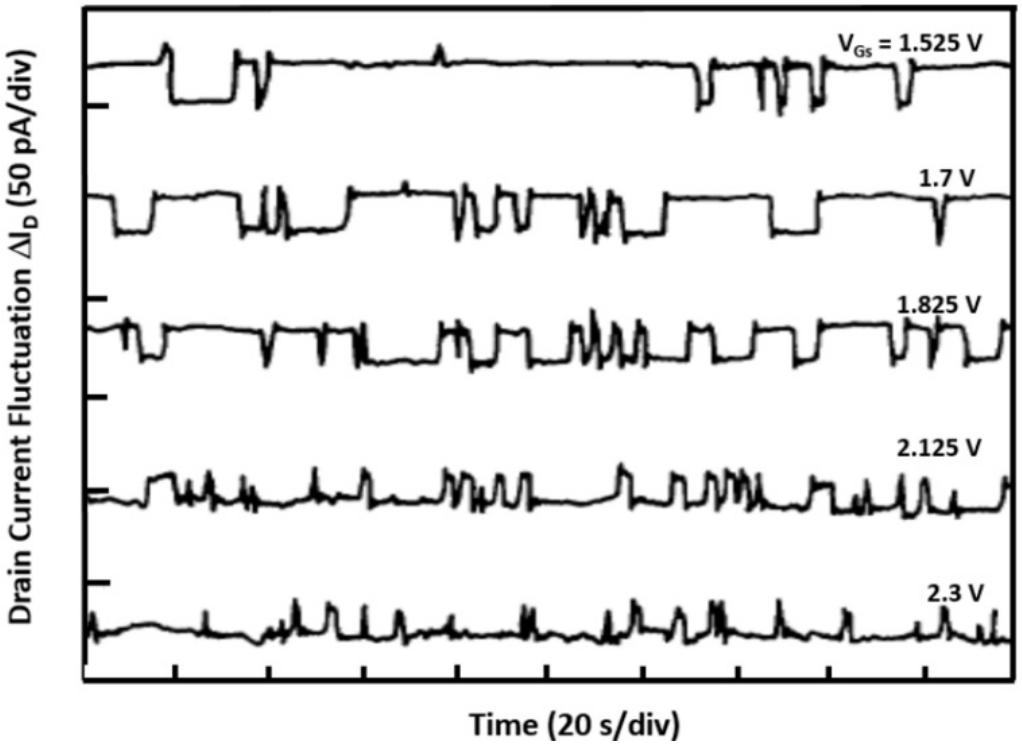

Source: (KIRTON; UREN, 1989).

Figure 8 – Random telegraph signal observed in a MIM-like RS device due to capture and emission of carriers by a single trap.

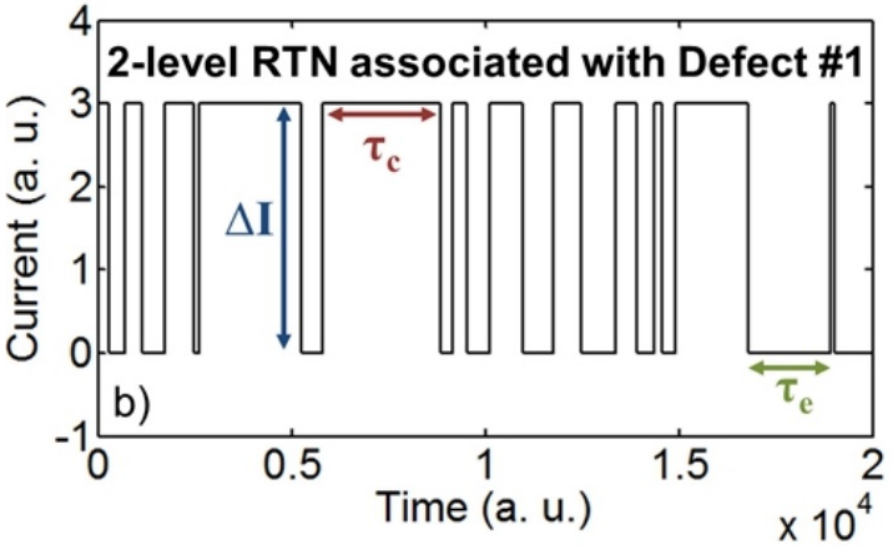

Source: Adapted of (PUGLISI *et al.*, 2017).

Figure 9 – Emission time constant of the trap exponentially distributed.

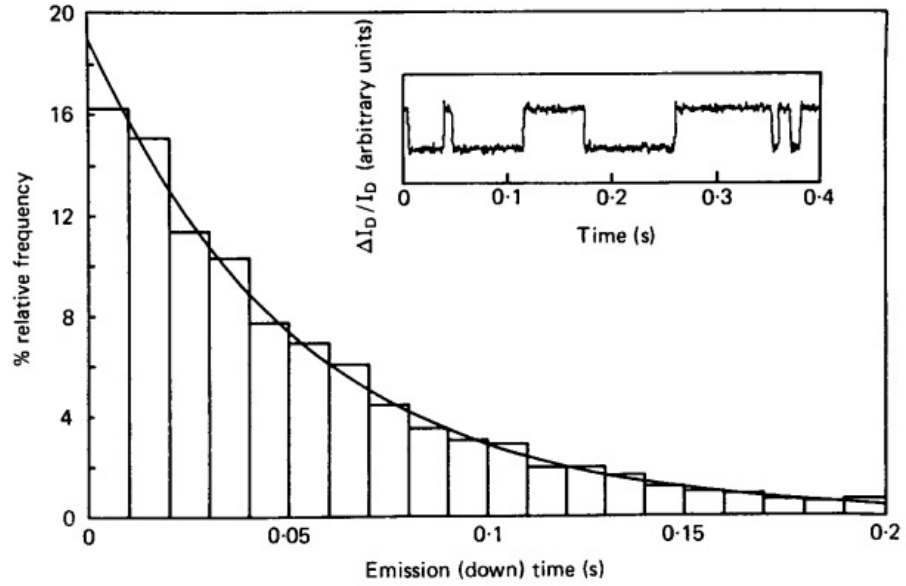

Source: (KIRTON; UREN, 1989).

In Figure 10 a RTN with 4 well-defined levels is presented, comprised by the independent sum of the signals produced by Defect#1 and Defect#2, each with its own characteristics (ΔI, τ_e and τ_c).

3.2 RTN in MIM-like RS devices

The RTN phenomenon is an important metric regarding the robustness of MIM-like RS devices, and it is intrinsic to any dielectric with defects (traps) (IELMINI; WASER, 2015). For MIM-like RS devices, RTN is more relevant at read voltage conditions ($\sim$ 0,1V), potentially inducing soft errors during read operations (especially when the memory window between HRS and LRS is relatively small). Therefore, RTN is more relevant at read voltage conditions ($\sim$ 0.1 V); it does not cause irreversible damage in devices, but affects the variability of the resistance and the magnitude of the current noise (IELMINI; WASER, 2015). Moreover, detection of RTN signals enable the identification of trap properties, which may provide valuable information about the reliability of materials and devices (i. e., the vertical distance of a trap responsible for the RTN from dielectric/electrode interface and the trap energy depth below conduction band of dielectric) (LEE *et al.*, 2011).

There are two major types of RTN signals observed: the steady-state fluctuations involving trapping/de-trapping with their corresponding time constants (depending on applied voltage and trap proprieties); and the non-steady-state fluctuations that appears from the structural disturbances in the CF due to removal or addition of oxygen or other vacancies (RAGHAVAN *et al.*, 2013). Figure 11 exemplifies two distinct signatures with

Figure 10 – (a) A multilevel RTN (in blue), originating from the activity of two defects, resulting in 4 well-defined discrete levels. (b,c) Decomposition of the multilevel signal shown in panel (a) into two independent two-level RTN signals, each associated to a specific trap.

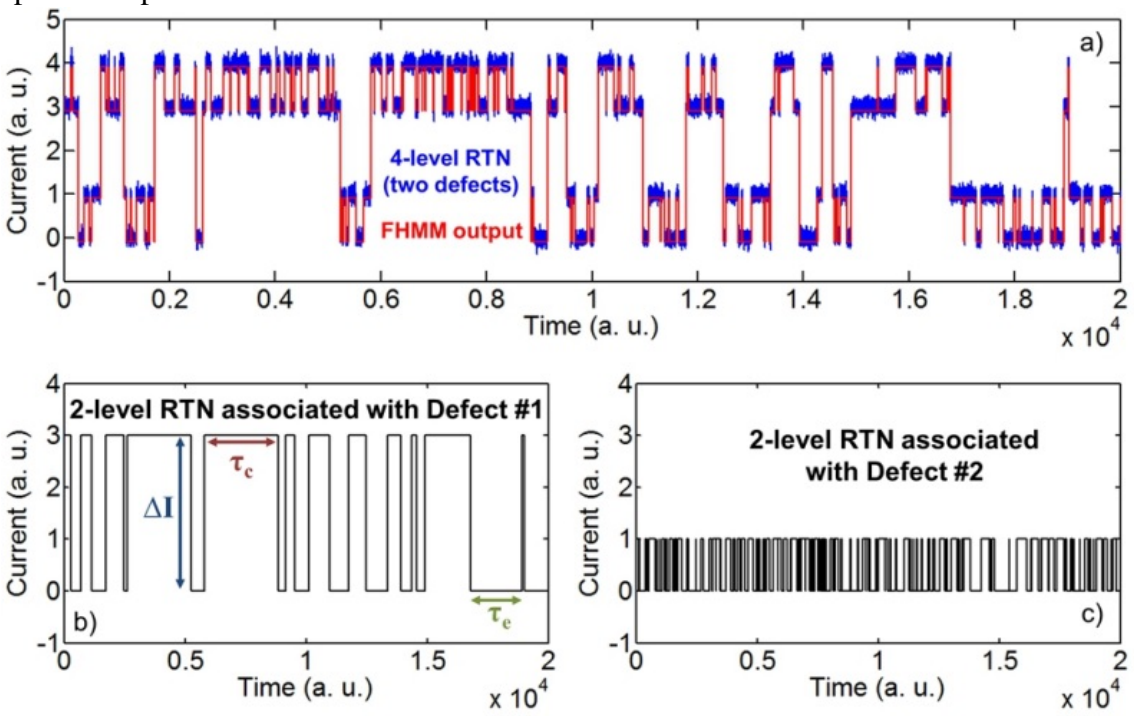

Source: (PUGLISI *et al.*, 2017).

different current amplitude shifts at different instants of measurement that suggests that they could be induced by the typical trapping and de-trapping process and by the vacancy transport inducing filament conductivity fluctuation.

Figure 11 – Observation of RTN signals during a positive ramp sweep in the HRS. The large current jumps (indicated by red dots and arrows) correspond to vacancy induced conductivity fluctuations and the smaller jumps correspond to electron trapping/detrapping.

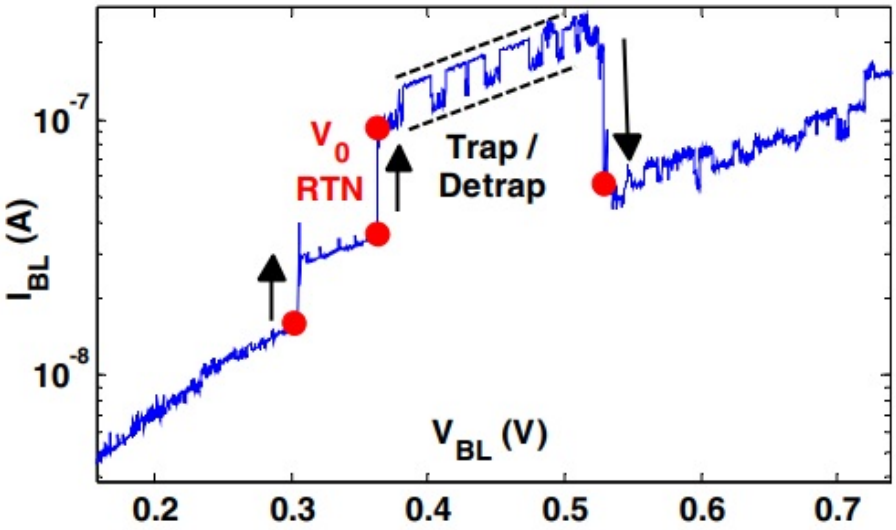

Source: (RAGHAVAN *et al.*, 2013).

In the following subsection, RTN-like behavior in emerging MIM-like RS devices are presented. Since different charge transport mechanisms are presented in the high resistance state (HRS) and low resistance state (LRS) (PUGLISI *et al.*, 2018), these effects will be analyzed separately for each operation mode.

3.2.1 RTN in the Low Resistance State

In the LRS state, the conduction mechanism is the drift of charge carriers in conductive filaments (CF) formed during the SET process. The charge-transport in this state exhibits quasi-ohmic characteristics (PUGLISI *et al.*, 2014) and the filament is normally organized by the alignment of a high density of defects and/or metal ions in the insulator medium. Considering the bulk model of resistance change (IELMINI; NARDI; CAGLI, 2010), trapping activity in the vicinity of a CF can locally reduce its conductance by a shielding effect on a portion of the CF. Considering this, when a trap emits/occupies it increases/decreases the filament conductivity. The model describes a cylindrical CF with length t_{ox} and diameter ϕ, resulting in a CF resistance of $R = \rho t_{ox}/S_{UF}$, where ρ is the filament bulk resistivity and S_{UF} is the CF cross-section in a uniform filament. To estimate the area in the CF cross section affected by trapping activity, the Debye length, given by equation $\lambda_D = (\epsilon kTq^{-2}n^{-1})^{1/2}$ is used, where ϵ is the CF dielectric constant, k is the Boltzmann's constant, T is the temperature, q is the elementary charge, and n is

the carrier density. The model accounts for a partial or total depletion by defect relaxation at the CF surface, and elucidate the size-dependent RTN in NiO RRAM (IELMINI; NARDI; CAGLI, 2010), Cu-based RRAM (SONI *et al.*, 2010), HfO_x-RRAM (AMBROGIO *et al.*, 2014) and the resistance drift in GeS_2 CBRAM (CHOI *et al.*, 2012). The model is outlined in Figure 12.

Figure 12 – Schematic picture of the RTN mechanism due to a defect with fluctuating charge at the CF surface. The CF diameter ϕ and the CF height, tox, equal to the oxide layer thickness, are shown. When the defect is negatively charged, the CF is depleted from carriers within approximately a Debye length.

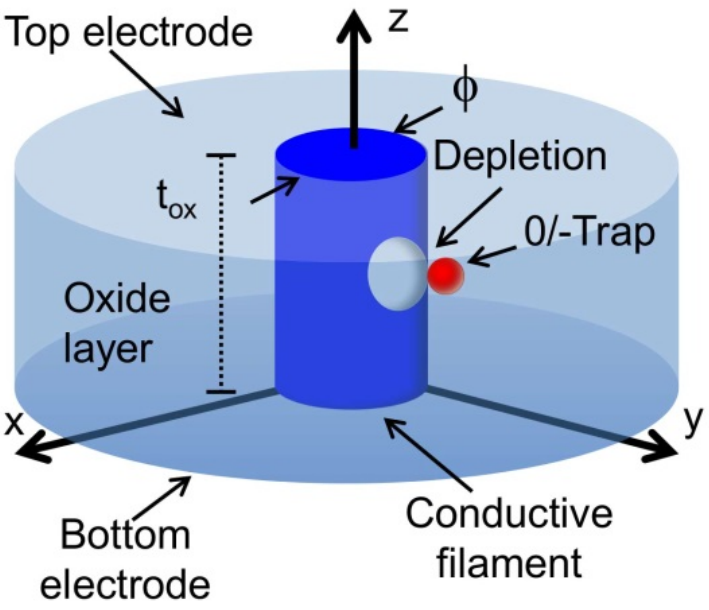

Source: (AMBROGIO *et al.*, 2014).

In this context, RTN shows a dependence on CF size, where the relative amplitude ΔR/R increases with increasing R (the filament resistance), thus decreasing the CF cross section. This situation is described in Figure 13a: increasing the compliance current (I_C) the impact on resistance fluctuation becomes smaller, because the higher the compliance current, the lower the resistance (R) and the thinner the filament (AMBROGIO *et al.*, 2014). In Figure 13b the relation between ΔR/R and R is presented. Note that the resistance change, ΔR, incrases with the resistance levels for all data (NiO-based RRAM, Cu-based electrochemical RRAM, Cu nanobridges, and HfO_x-RRAM). This universal dependence on R is understood by the aforementioned size-dependent depletion model (AMBROGIO *et al.*, 2014; IELMINI; NARDI; CAGLI, 2010).

PUGLISI *et al.* (2018) presented this discussion considering the charge transport in LRS for a HfO_2 RRAM. In this case, the conductive filament is formed by a multitude of oxygen vacancies (Vo), meaning the two electrodes are connected by them. The charge transport will occur due to charge carriers drift along the CF in an ohmic behavior, char-

Figure 13 – (a) Measured (on the left) and b) calculated (on the right) resistance depending on the current compliance (I_C). Note in a) and b) that the relative amplitude $\Delta R/R$ increases at increasing R. Calculations were made tunning the carrier density, N_D.

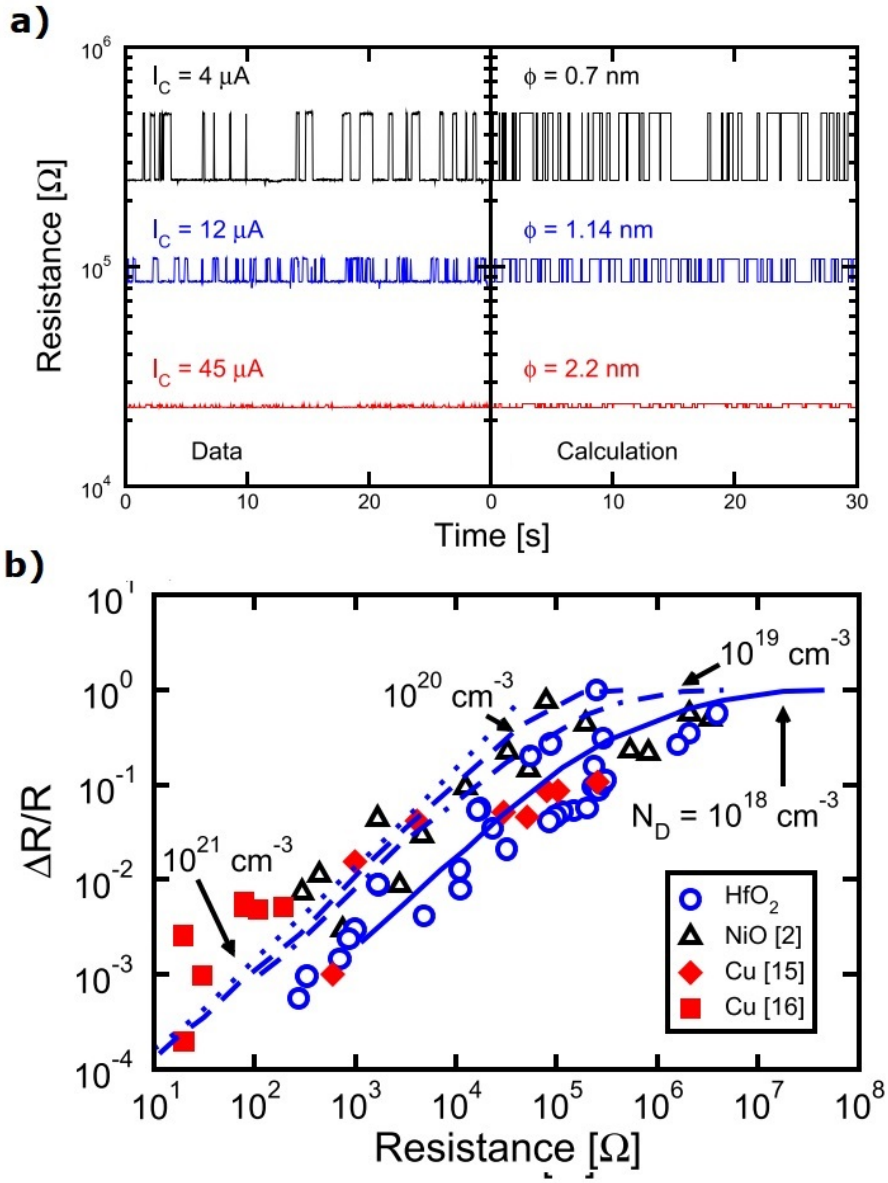

Source: (AMBROGIO *et al.*, 2014).

acterizing the LRS state, with a given low resistive value, R_{LRS}. The activity of a trap in the vicinity of the filament produces the shielding effect and a variation in its resistance. The relative resistance variation (ΔR) will depend on the filament geometry, its radius (r_{CF}) and its thickness (t_{CF}) when a cylindrical shape is assumed for the CF. For a wide filament, (r_{CF}) $>> \lambda$, the portion of the depleted filament is significantly smaller than the area of the conductive filament, $A_{CF}=\pi(r_{CF})^2$, resulting in a small resistance variation. Consequentely, the thinner the analyzed filament, the greater the impact of trapping activity will be on the relative variation of the filament resistance. If the voltage is kept constant, the greater impact on ΔR/R implies a higher impact on current switching (BALATTI *et al.*, 2014; AMBROGIO *et al.*, 2014).

3.2.2 RTN in the High Resistance State

The physical mechanism responsible for RTN in HRS is still under debate (PUGLISI *et al.*, 2018; VEKSLER *et al.*, 2014), but it is widely attributed to the activation and deactivation of defects promoting trap-assisted tunneling (TAT) transport in the oxidized gap of the conductive filament formed in HRS. The most accepted theory, for the case of metal oxides, explains the RTN by two mechanism. 1: the coulomb interaction between a fast defect, as the oxygen vacancies that assist the charge transport, and a slower defect, as the electron charge trapped at interstitial oxygen defects; 2: the metastable defect configuration of oxygen vacancies that allow the charge transport in HRS (PUGLISI *et al.*, 2015).

Figure 12a illustrates a MIM-like RS device in its HRS and the two most likely mechanisms responsible for RTN in metal oxides in this operation mode (PUGLISI *et al.*, 2015). The first hypothesis is shown in Figure 12b and d: the charge trapping at neutral oxygen interstitial (a slow defect), in the vicinity of an oxygen vacancy (faster defect), can prevent the oxygen vacancy (Vo) to support the TAT transport due to the Coulomb blockade effect. In this case, when the slower defect is occupied, the effective current drops; and when the slow defect emits, the effective current grows abruptly. The second hypothesis, presented in Figure 12c and e, considers the existence of metastable states in oxygen vacancy defects (GRASSER, 2012). In this framework, the transition of the oxygen vacancy defect from a metastable (i.e., faster state) to a stable (i.e., slower state) state configuration can interrupt and provide the charge transport through the defect. The defects time constant will be very short when the defect is in its metastable configuration, and so contributing to the charge transport. However, when the defect is in its stable configuration, the capture and emission times became much longer, which prevents the defect from contributing to the current flow.

Figure 14 – (a) Illustration of a TiN/Ti/HfO_2/TiN RRAM in HRS operation mode. The barrier thickness (t_b) and the conductive filament (CF) are highlighted. b) and d) When a slow defect (oxygen insterstitial) is occupied, in the vicinity of a fast defect (oxygen vacancy), it may induce a Coulomb blockade effect preventing the TAT transport. X_T is the trap location. c) and d) The TAT current depends on the charge transition between the neutral and the positive metastable state of an oxygen vacancy. When the defect is in its stable configuration the TAT transport is inhibited, and the opposite occurs when the defect is in its metastable state. These transistions cause RTN.

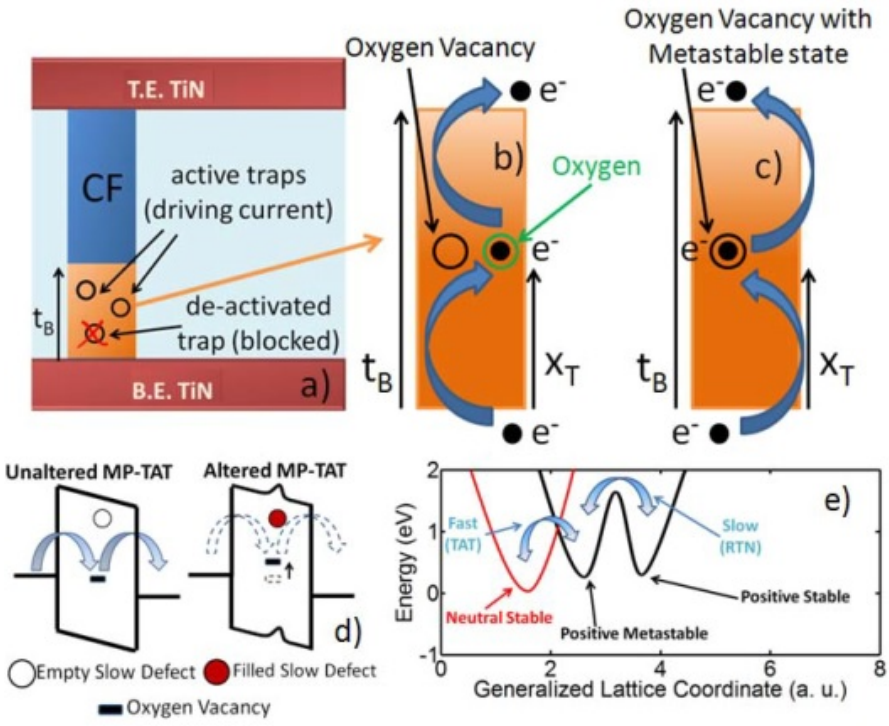

Source: (PUGLISI *et al.*, 2015).

3.3 RTN in h-BN based cells

Most studies, as shown in previous subsections, describe RTN in the context of metal oxides. Recently, however, RTN has been analyzed for other dielectrics, with particular interest in 2D-materials as RS medium in MIM-like RS devices (SHI *et al.*, 2018; LANZA *et al.*, 2019). Considering h-BN, recent studies have shown that RTN is also a factor when this RS medium is applied in the MIM cells (SHI *et al.*, 2018; LANZA *et al.*, 2019; RANJAN *et al.*, 2018).

In SHI *et al.* (2018), the authors identify the trapping and de-trapping of charges in a Au/Ti/h-BN/Cu device in reading operations. In RANJAN *et al.* (2018), the measured RTN in h-BN-based cells presented a combination of both two-level and multi-level RTN signals, corresponding to the trends commonly observed for metal oxides. During these measurements, many instabilities and anomalous current fluctuations were found. In these measurements, exponential distributions for τ_e and τ_c were reported, which is related to the stochastic nature of the traps located in the vicinity of the filament, as presented in Figure 15. Also, this work also reported flucutations that were consistent with the existence of metastable defect states in h-BN. In RANJAN *et al.* (2018b), the authors indicate the presence of low frequency Lorentzian RTN traces in the LRS state, showing that charge transport is governed by the defects as Boron vacancy/ions formed in the h-BN layer during the SET process.

Figure 15 – (a) Multi-level RTN measured for an h-BN/Cu based sample. (b) Section of the measurement presenting a stable two-level RTN. (c) and (d) Exponential plot of the extracted τ_c and τ_e values for the signal between 10 and 20 s. e) Illustration showing a multiple defects interacting in the vicinity of the percolation path of the formed filament and the electrostatic defect interactions.

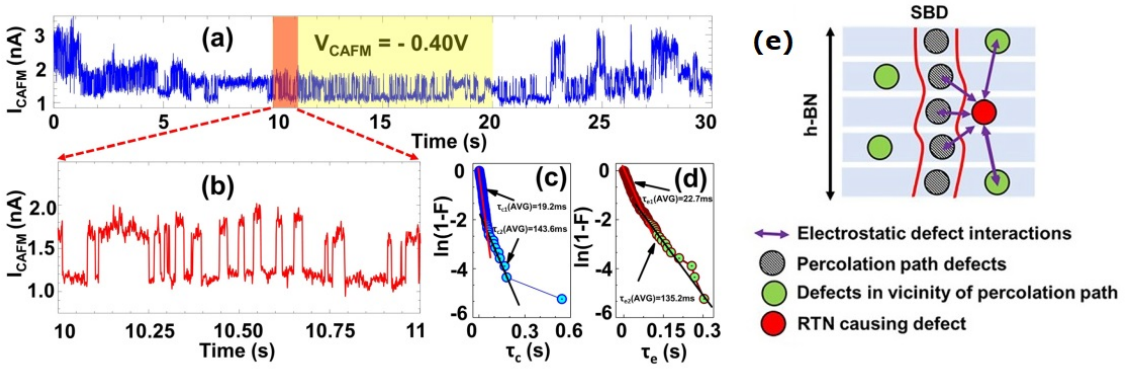

Source: Adapted of RANJAN *et al.* (2018).

3.4 RTN dependence on bias voltage

RTN has become an important tool to assess the reliability of emerging devices, given its potential in characterizing the defects by extracting the energy level of traps, as well as their physical location, average density, and their respective relaxation and activation energies. In this sense, obtaining these parameters is only possible when the properties of the defect are related to known variables, such as the applied read voltages (V_{READ}), the sample temperature, the amplitudes and the average capture and emission times of the measured RTN signal. In this context, GONG *et al.* (2018b) developed a technique for characterizing defects based on the behavior of the capture times, τ_c and τ_e, as a function of the applied V_{READ}. This process is described in Figure 16, which presents the four typical observed behaviors for the measured time constants in RS devices as a function of the bias voltage. The dependence of τ_c and τ_e on bias can determine whether the analyzed trap interacts with the top (TE) or bottom (TE) electrode: if the rate $ln((\tau_c)/(\tau_e)$ is negative, it means that the defect interacts with the bottom electrode (Figure 16b-c), if positive, the defect interacts with the top electrode (Figure 16d-e). Note that in Figure 16c-e the emission has a constant trend, meaning that it is independent of the applied voltage. This indicates that the trap capture the electrons from the bottom or the top electrode, respectively, and emits it through thermionic emission.

Figure 16 – (a) RTN defect characterization in a TaO_2/HfO_2 cell by increasing the polarization voltage of the MIM cell. Inset shows the RTN signal of LRS at 2.5 V. The red line is the fitted RTN signal. (b-c) If the polarity of the time constant variation rate is negative, the defect interacts with the bottom electrode. (d-e) If the polarity of the time constant variation rate is positivee, the defect interacts with the top electrode. Note that in (c-e), the emission time is constant, indicating that the trap emit the electrons through thermionic emission.

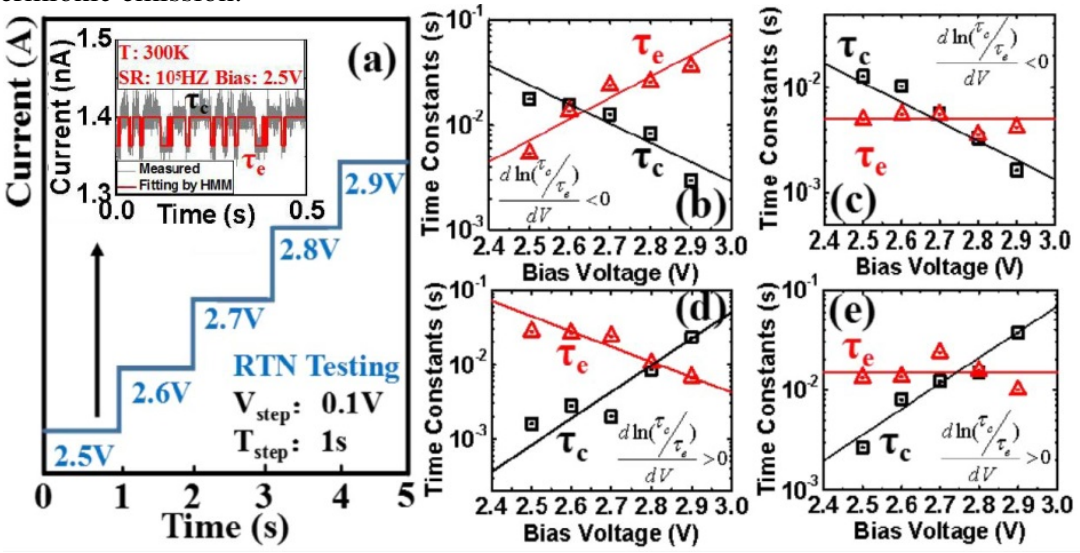

Source: (GONG *et al.*, 2018b).

Both the defect's vertical position, x_T, and the trap energy, E_T, can be estimated. The occupancy of the trap is governed by Equation 1 (GONG *et al.*, 2018b):

$$E_T - E_F = \frac{K_B T}{q} ln(\frac{\tau_c}{\tau_e}) \tag{1}$$

where E_F is the Fermi energy level, K_B is the Boltzman constant, T is the temperature, q is the fundamental charge of the electron, and τ_c and τ_e represent the average capture and emission times measured, respectively, of the trap. In addition, the vertical location of the trap, x_T, can be obtained from the relationship presented in Equation 2:

$$\frac{x_T}{T_{OX}} = \frac{K_B T}{q} \frac{dln(\frac{\tau_c}{\tau_e})}{dV} \tag{2}$$

where, x_T is the distance of the trap in relation to the respective electrode, T_{OX} is the thickness of the oxide and V is the applied voltage.

A similar result is obtained in PUGLISI *et al.* (2015), which agrees with the behavior presented in Figure 16e. Note in Figure 17a that the current fluctuation, ΔI, increases along with the applied reading voltage, due to the increase in the tunneling and relaxation probability in an multiphonon trap-assisted tunneling (MP-TAT) process. However, the relative variation of the current, ΔI/I, is independent of the reading voltage, demonstrating that the increase in conduction is related to a greater probability of tunneling (trap activity). The exponential dependence of τ_c on V_{READ} is mainly due to the higher energy released by electrons to the lattice at every capture event. In contrast, the constant trend shown by τ_e is because the electron emission occurs preferentially from the ground state of the trap and the relaxation probability does not depend on the applied voltage

Although the literature is more comprehensive for HfO_2 based devices, it is noteworthy that this dicussion is also valid for TiO_2 based cells, as presented in PIRROTTA *et al.* (2014) and FRÖHLICH (2013).

Figure 17 – (a) Experimental current variation, ΔI (in blue), in a HfO_2 based device and the current variation over the average current, ΔI/I (in red), over the applied reading voltage. (b) Experimental average capture (in blue) and emission (in red) times over the applied reading voltage. τ_c exponentially depends on V_{READ}, while τ_e shows a constant trend.

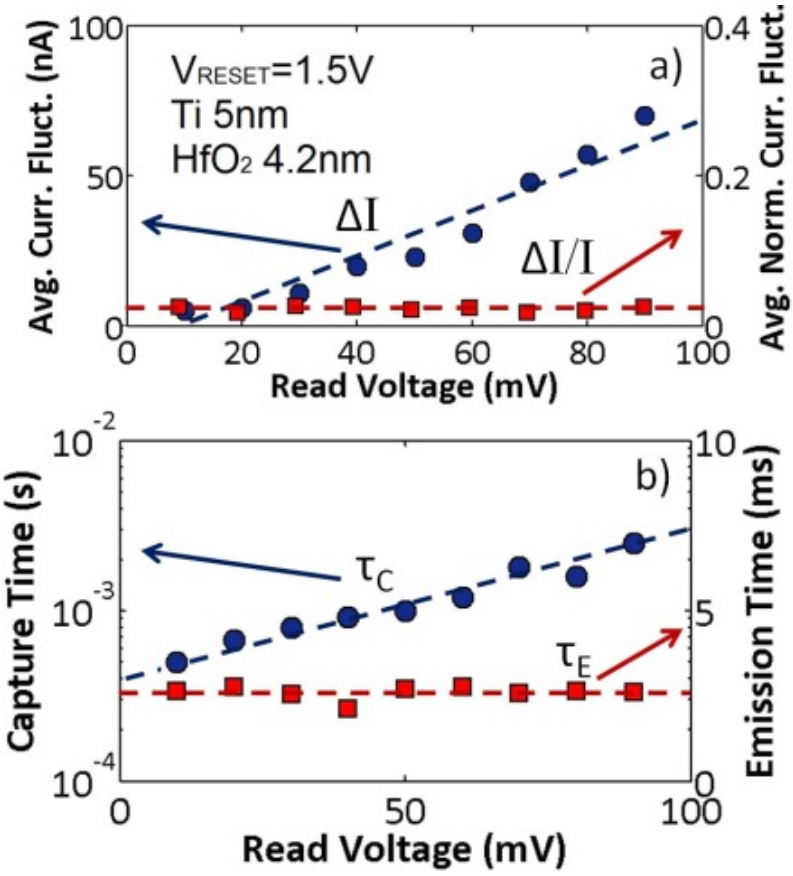

Source: (PUGLISI *et al.*, 2015).

4 NON-STANDARD RTN PATTERNS

As discussed in previous chapter, important progress has been made in recent years towards understanding the physical mechanisms resposible for RTN in MIM-like RS devices. Nevertheless, additional efforts are required to refine the understanding of irregular RTN patters, such as time-dependent RTN and anomalous RTN (aRTN) (GRASSER, 2020). Anamalous RTN is the set of multilevel RTN-like signals that cannot be modeled as the simple sum of independent two-level RTN signals, in which the components that sum up to the observed aRTN signal can present certain degree of correlation, although this behavior is still far from being understood (GRASSER, 2020). Temporary RTN, on the other hand, is related to the abnormal temporal changes of the RTN parameters (PUGLISI *et al.*, 2016). In this chapter, experimental data available in the literature on aRTN and temporary RTN are presented and discussed.

4.1 Trap Coupling Effect

Anomalous RTN signals, sometimes also identified in the literature as complex RTN, are reported not only in the context of MIM-like RS devices, but also for other devices, such as MOSFETs (WANG *et al.*, 2018) and FINFETs (ZHANG *et al.*, 2018). In these works, the observed anomalous RTN behavior is associated to a *coupling effect* between different traps in the same device. This coupling effect means that the amplitude and time constants of one trap are affected by the occupancy state of another trap.

This coupling effect is exemplified in the context of MOSFETs (WANG *et al.*, 2018) in Figure 18. The time trace in Figure 18 exhibits two distinct RTNs; a slow RTN and a fast RTN. Careful analysis of the time trace indicates that both the measured trap impact (ΔId/Id) as well as the average time-to-capture (τ_c) of the fast trap are correlated to the slow trap state, being A and B the time traces of the fast trap when the slow trap is empty and occupied, respectively. Following WANG *et al.* (2018), aRTN with coupled amplitude, i.e., the current deviation produced by one trap is affected by the occupancy of another trap, can be classified into two categories: i) if the current amplitude deviation (ΔI) increases when another trap is occupied the coupling effect is positive; ii) if the

current amplitude deviation (ΔI) decreases, the coupling effect is negative.

Figure 18 – An example of anomalous RTN induced by two coupled traps in a MOSFET device, referred to as coupling effects complex RTN (CE-cRTN). Note that the slower trap impacts on both he average time-to-capture (τ_c) and the relative amplitude (ΔId/Id) of the faster trap. In situation A: the slow trap is empty. In situation B: the slow trap is occupied.

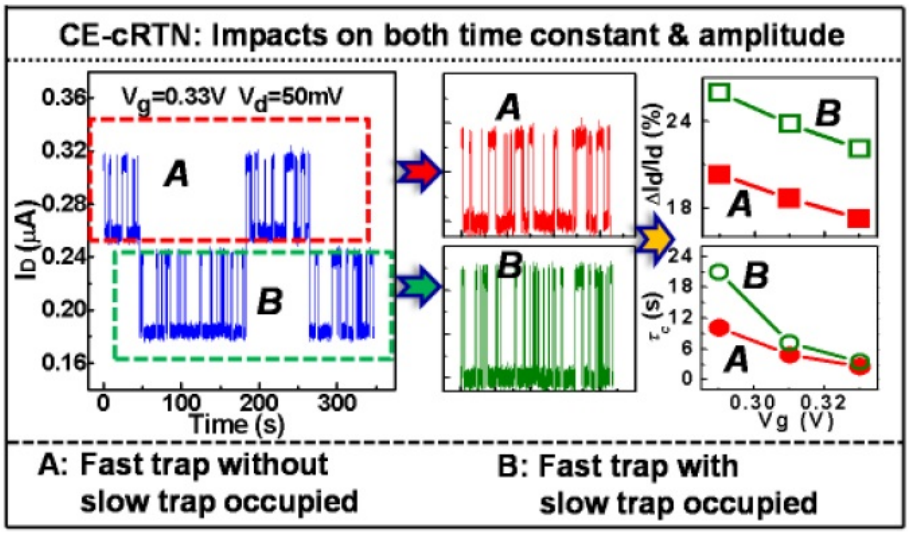

Source: (WANG *et al.*, 2018).

WANG *et al.* (2018) present two microscopic mechanisms of trap interaction to sustain this theory: one is the Coulomb repulsion effect between different traps; and the other, presented in Figure 19 is the channel percolation effect, through an important local carrier density change induced by trapping activity. This mechanism is presented by the authors as the dominant trap interaction mechanism in single nanoscale devices. For instance, in the case of MIM-like RS devices, when the CF across the insulator is not homogeneous, the electrical field may not be constant over the dielectric. Then the electrical potential at the trap site is not solely a function of trap distance from the electrodes. Furthermore, the electrical potential at a trap site may change if occupation of other trap sites changes.

The trap coupling mechanism has been discussed in the context of FINFETs by ZHANG *et al.* (2018) and GUO *et al.* (2018). ZHANG *et al.* (2018) demonstrated that the traditional RTN is not totally dominant in the measured samples, since the RTN signals associated to trap coupling exceeded 40% of the cases in their FINFETs samples. Furthermore, there is a significant amount of 3-level RTN, with a strong coupling effect between traps, despite the 4-level RTN being the most recurrent behavior. Both situation are presented in Figure 20.

It is important to remark that in a traditional multilevel RTN, the signal presents 2^N levels, where N is the number of active traps. In the case of 3-level RTN, an expected current discrete level is lost (masked) due to different effects, such as coupling between

Figure 19 – Mechanism of trap interaction behaviours: traps on the same percolation path will impact each other's characteristic parameters.

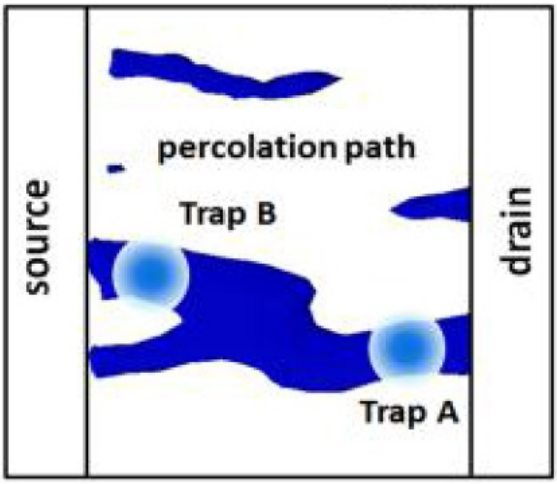

Source: Adapted of WANG *et al.* (2018).

Figure 20 – RTN-like signal measurments in a FINFET device: a RTN with a missing level (strong coupling effect) and a RTN induced by two coupled traps (note that the fast trap switches with a larger amplitude when the slow trap emits).

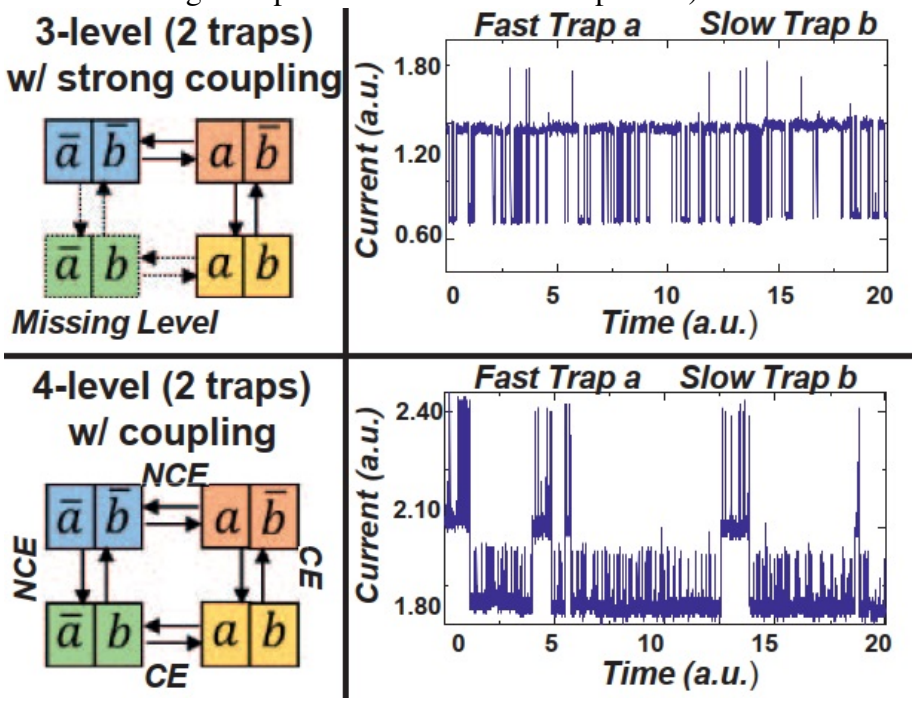

Source: Adapted of ZHANG *et al.* (2018).

the traps. The situation is verified when the current level when a fast trap (A) is occupied and another slow is empty (B) is very similar to the current level observed when A is empty and the B occupied. According to GUO *et al.* (2018), the coupling effect is related to the fact that the charged trap can change the distribution of channel percolation path (PP) in the FINFET and thus change the RTN induced by another trap. 3-level RTN signal are also recorded in MIM-like RS devices, as presented in an Oxide-Based Resistive Switching Memory (GONG *et al.*, 2018).

GUO *et al.* (2018) also presents the trap coupling effects on measured RTN in a FINFET, shown in Figure 21. The current variation produced by the fast trap (a) is impacted by the switching activity of the slow trap (b). It is possible to observe that the impact of (a) is significantly smaller when (b) is occupied, thus being refereed to as a negative coupling. The authors also conclude the RTN amplitudes are mainly impacted by the formed percolation paths.

Figure 21 – (a) The illustration of the measured FinFET. (b-c) The typical RTN measured data with coupling effect. Note that the amplitude of the faster RTN (A) is reduced while the slow trap (B) is occupied. This is called negative coupling effect.

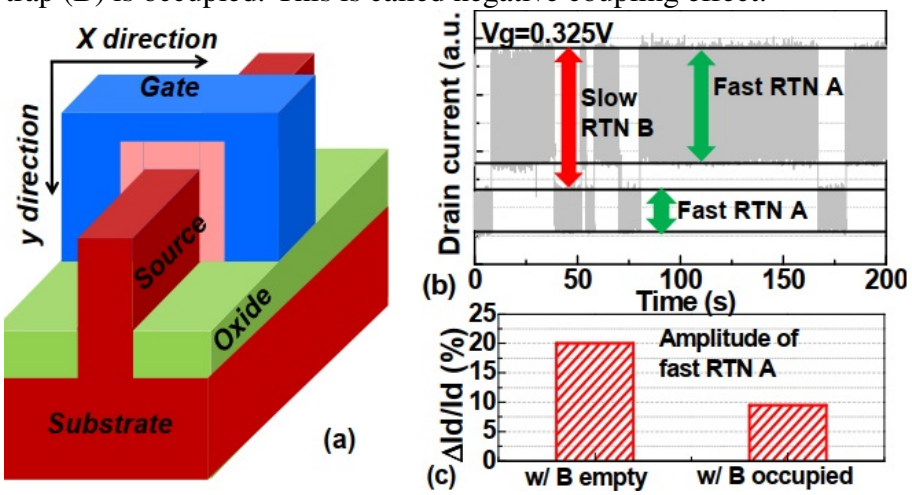

Source: (GUO *et al.*, 2018).

4.2 Temporary RTN

Besides two-level, multilevel, and anomalous RTN fluctuations, experimental observations (PUGLISI *et al.*, 2016) show the occurrence of temporary RTN-like behaviors. These phenomena are usually classified as follows: 1) Transient RTN (tRTN): a two-level RTN fluctuation that appears and disappears during the measurement in a random and time-dependent fashion. This fluctuations shows no correlation with another two-level RTN components, as presented in the aRTN context. 2) Mutant RTN (mRTN): a two-level RTN-like behavior that randomly and temporarily changes its statistical characteristics, i. e., amplitude deviation (ΔI) and/or its time constants (τ_c and τ_e). This temporary beha-

vior was also discussed in the context of MOSFETs by GRASSER (2012), which reported RTN signals that were visible for a relatively short period of time before vanishing.

PUGLISI *et al.* (2016) proposes a model for measured tRTN (see Figure 22a) in HRS in reading condition for a MIM-like RS device based on HfO_2. This signal is characterized by a dominant two-level RTN fluctuation from the beginning of the measurement until time $>$ 9 s. Then, this two-level RTN temporarily vanished and reappeared at time $>$ 18 s. The authors attribute this behavior to the defect drift-diffusion mechanism. It was demonstrated through simulation that diffusion of O (oxygen) interstitial defects also occurs in reading conditions, although this is not the case for oxygen vacancy (Vo) defects. PUGLISI *et al.* (2016) also consider that both the Coulomb interaction between charged defects and the possible O interstitial diffusion allow reproducing both the tRTN and mRTN presented in Figures 22 and 23, respectively. In the context of Figure 22a, the authors conclude the RTN statistical properties are affected by changes of the O interstitials position and energy. Figure 22b show the Coulomb interaction between the oxygen vacancy (Vo) that assist the charge transport (red spheres) and the interstitial O (blue spheres), in a light red zone. In this model, if the new location of the diffused O interstitial becames too far from the Vo defect assisting the TAT current, then the RTN fluctuation will vanish with the reduction of their Coulomb interaction.

The same model used to describe transient RTN can be adapted to explain mutant RTN (PUGLISI *et al.*, 2016). For instance, as described in the previous chapter, an O interstitial in the vicinity of a Vo defect can cause RTN. Thus, if this defect slightly changes its position as a result of interstitial diffusion (but still having a Coulomb interaction with the Vo), Figure 23b, then the change in the RTN properties will be correspondingly small. This scenario corresponds to the measured mRTN presented in Figure 23a. The differences on the model interpration between tRTN and mRTN are restricted only by the random positions of both the Vo and the O interstitial defects. If the new location of the diffused O interstitial becames too far from the Vo, vanishing the defects Coulomb interaction, it may lead to tRTN; if its new location is close enough to maintain the Coulomb interaction, it may lead to mRTN. Both mechanisms depend on the stochastic nature of the microscopic involving drift/diffusion and charge trapping/de-trapping.

4.3 Giant RTN

Finally, other works (SONI *et al.*, 2010; BENVENUTI *et al.*, 2014) also present a different RTN-like phenomena, characterized by a huge impact on the conductance fluctuation in reading operation, usually called *Giant RTN*. For instance, in the context of MIM-like RS devices, giant RTN fluctuations characterized by relative resistance variations of up to 50%, illustrated in Figure 24, were presented in SONI *et al.* (2010). Comparatively, the same work found variations in the range of 5% in similar MIM cells under

Figure 22 – (a) Experimental tRTN measured in an HfO_2-based MIM-like RS device in HRS at V_{READ} = 60 mV. (b) Illustration of a possible diffusion scenario leading to tRTN. The O interstitial diffuses in a available interstitial site far from the Vo, temporarily modifying τ_c and τ_e and stopping the 2-level RTN.

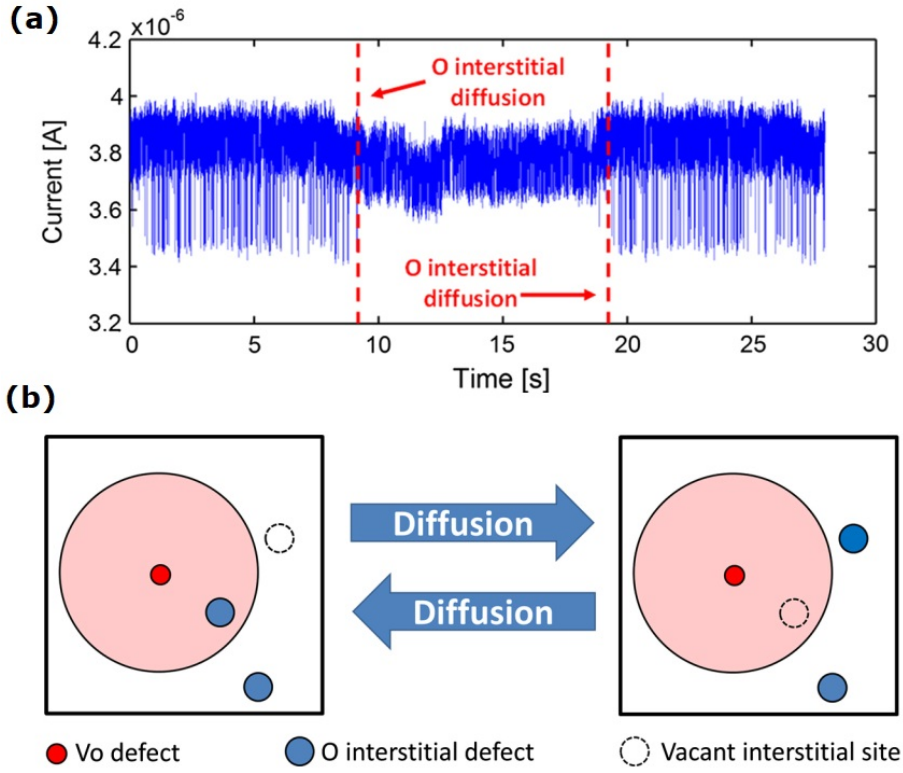

Source: Adapted of PUGLISI *et al.* (2016).

Figure 23 – (a) Experimental mRTN measured in an HfO_2-based MIM-like RS device in HRS at V_{READ} = 80 mV. (b) Illustration of a possible diffusion scenario leading to mRTN. The O interstitial diffuses in another available interstitial site close from the Vo, temporarily altering the RTN characteristics, τ_c and τ_e.

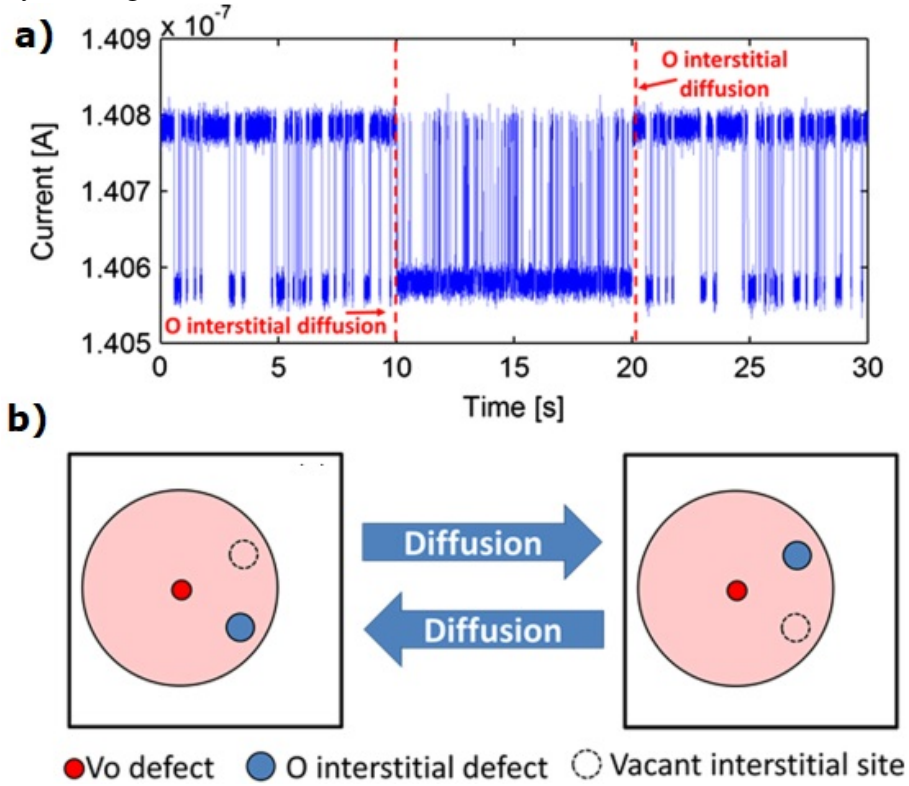

Source: Adapted of PUGLISI *et al.* (2016).

the same conditions when the giant RTN is absent. In this paper, the Giant RTN phenomenon is associated to the different geometries of the percolation paths formed in the cell. For every percolating conducting network exists an ensemble of different structures and critical weak links, i. e., regions where the filament presents small effective cross-sectional areas. Thus, very large relative resistance (conductance) swings can happen when trapping acitivity affects the conductivity of one of the weakest connections along the conducting paths. BENVENUTI *et al.* (2014) also observed, in simulation, that giant RTN may occur when a trap is placed on these critical positions on the conductive path, i. e., when the defect is able to switch-off the main percolation path for a dopant/grain configuration with a highly non-uniform conduction. Such large resistance fluctuations can induce significant bit-error rates during reading cycles in memory applications. This can be an important issue for the industrial applications of MIM-like RS devices (SONI *et al.*, 2010).

Figure 24 – Experimental giant RTN signal with $\Delta R/R \simeq 50\ \%$ observed on a Cu doped $Ge_{0.3}Se_{0.7}$ based cell.

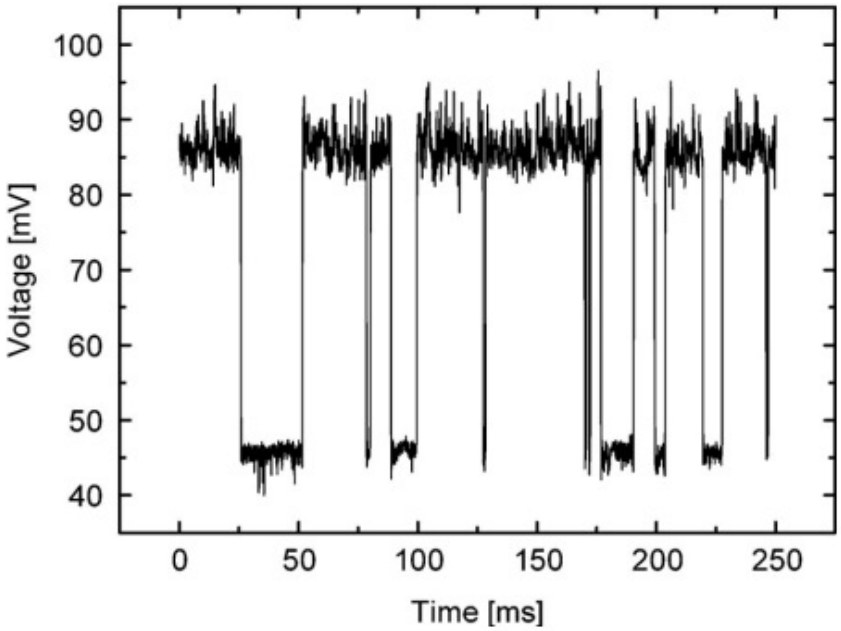

Source: Adapted of SONI *et al.* (2010).

5 DEVICES CHARACTERIZATION AND DATA ANALYSIS

The complex RTN-like patterns and characteristics presented in the previous chapter pose a significant challenge towards understanding and modelling these effects (LANZA *et al.*, 2019; PUGLISI *et al.*, 2017). In this chapter, the most commonly used methods are presented and discussed, highlighting their limitations.

5.1 Measuring RTN in MIM-like RS Devices

As discussed in chapter 3, the traditional 2-level RTN, resulting from the activity of a single trap, is described by 3 parameters: the amplitude fluctuation of the electrical quantity, usually ΔI; and the average times required to emit (τ_e) and capture (τ_c) a charge carrier. However, as the temporal parameters represent the average value of an exponential time distribution, the individual realization of the charge capture and emission events occur in a time interval that can deviate orders of magnitude from their respective average values. Regarding this matter PUGLISI *et al.* (2017) alert that the statistical analysis of the RTN parameters has to account for fundamental characteristics of the noise process, such as:

(a) Several defects may be active on the same device, and each one of them has capture and emission times that can differ by orders of magnitude;

(b) Operating conditions, especially reading voltage, modify the properties of the RTN;

(c) The RTN parameters are — prior to the measurement — unknown. Thus, the sampling window and the measurement time resolution are defined during the characterization, and cannot be pre-determined.

Considering the exponential nature of the distribution of RTN time constants, it is possible that some of their individual realization along the measurement will be shorter than the sampling time (the measurement resolution). This is an issue when the time sampling is not short enought to estimate the average value of the parameters, resulting in undersampling (PUGLISI *et al.*, 2017). This situation is exemplified in Figure 25. Note that when the sampling time (τ_s) is equal to the average time constants ($\tau_{c,e}$) = 100 ms (in

red), the signal is totally corrupted. However, when τ_s is 100 times shorter than $\tau_{c,e}$ (in blue), the RTN discrete levels are well-defined and correctly recorded.

Figure 25 – Experimental giant RTN signals recorded for different sampling time (τ_s): τ_s is 100 times shorter than $\tau_{c,e}$ (in blue); τ_s is half of $\tau_{c,e}$ (in pink); τ_s is equal to the average time constants ($\tau_{c,e}$) = 100 ms (in red). Note that in the last case the signal is corrupted. When τ_s is sufficiently shorter than $\tau_{c,e}$, the RTN discrete levels are well-defined on measurement.

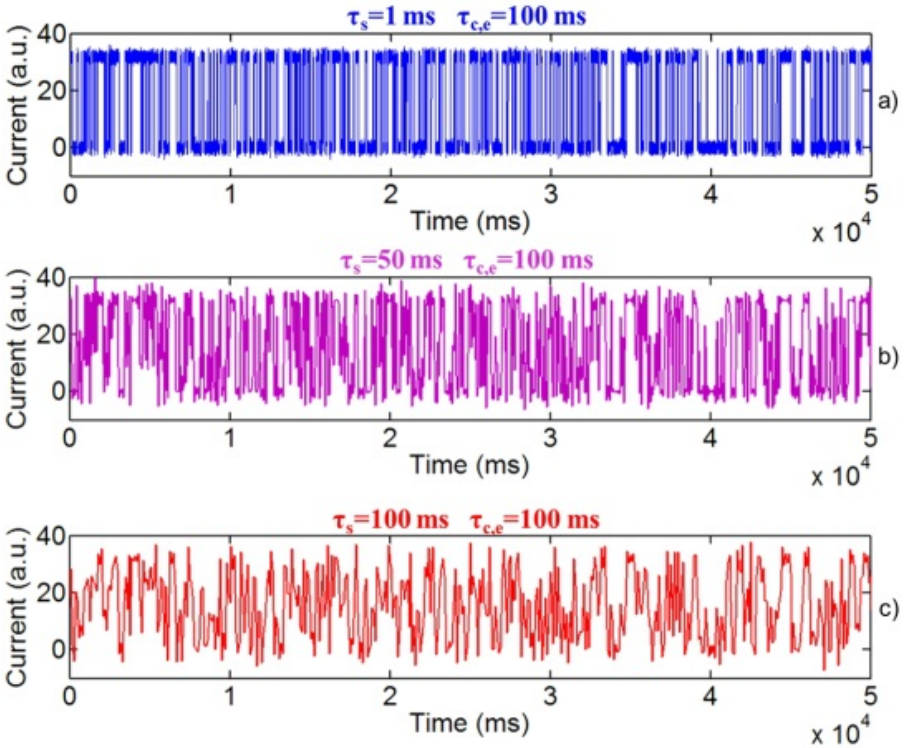

Source: Adapted of PUGLISI *et al.* (2017).

Besides undersampling, for a fixed measurement time window, reducing sampling time may result in prohibitively large measurements. Thus, a compromise between the temporal resolution (τ_s) and the measurement time window, which depends on the finite number of samples composing the measured RTN signal (N), must be achieved. In Figure 26, the relative percentage error in the estimated average capture and emission times are shown, which decrease with increasing the H ratio, ($\frac{\tau_{c,e}}{\tau_s}$). PUGLISI *et al.* (2017) define a safe operating zone from a given H, when the error becomes constant and dependent only on N. In short, during the electrical characterization, it is expected to measure an RTN signal whose average parameter values, τ_c and τ_e, are at least one order of magnitude (10 times) larger than τ_s, also observing the number of samples N.

The first step to analyse RTN signals is the extraction of the well-defined levels from the measured RTN data. The most typical approach relies on building the histogram of the measured RTN signal (REALOV; SHEPARD, 2010) assuming that the background noise superimposed to the RTN signal can be considered Gaussian. As an example, observe the

Figure 26 – The relative percentage error in the estimated average capture and charge emission times of two-level RTN signals over the ratio (H) between the actual $\tau_{c,e}$ and the sampling time τ_s. Thus, $H = \frac{\tau_{c,e}}{\tau_s}$. A safe zone from a given H is identified when the relative error is constant and dependent only on the lengh of the signal (N).

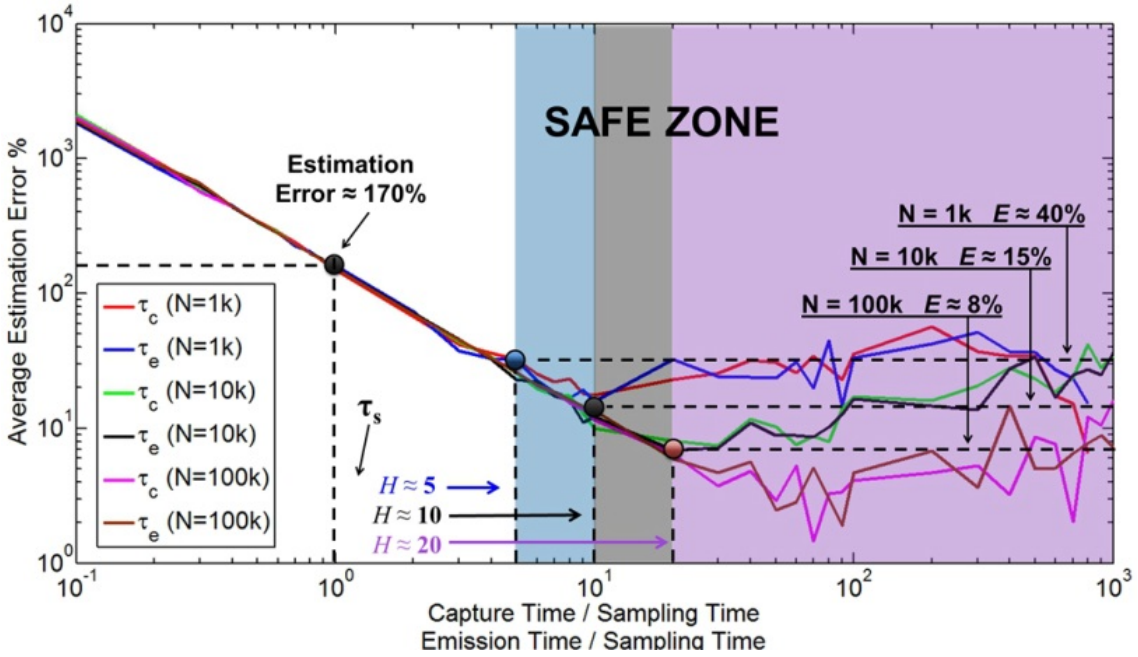

Source: Adapted of PUGLISI *et al.* (2017).

traditional multilevel RTN presented in PUGLISI *et al.* (2017) in Figure 27a, that presents 4 well-defined current levels. A gaussian model fitting with the 4 four components can be applied to estimate the average values of the Gaussian's distributions. Another tool widely used in such analysis is the time-lag plot (TLP), presented in Figure 27b. By counting the number of spots in a TLP, it is possible to estimate the number of RTN discrete levels. Figure 27c shows the current histograms and the four Gaussian's means: μ_{L1}, μ_{L2}, μ_{L3}, and μ_{L4}.

Once the discrete levels were found, the next step consists of extracting the individual realizations of $\tau_{c,e}$. The most used method to estimate the average values of time constants is the Factorial Hidden Markov Model (FHMM), (PUGLISI; PAVAN, 2013), where the state of each trap is considered a random variable, and the RTN signal is seen as a superposition of multiple two-level RTNs. A graphical representation of the FHMM concept is given in Figure 28, where S_t^m represents the hidden state of each trap under analysis, being state (m), at time (t), while Yt represents the output of the entire process (i. e., the expected value of the multilevel RTN) at time t.

It is important to remark that FHMM is used in traditional multilevel RTN analysis, but the instabilities in RTN traces, such as anomalous or time-dependent RTN, complicate the analysis. In this cases, the analysis is usually made by intervals, regarding the changes in the RTN parametters and the correlation between different defects, as in RANJAN *et al.*

Figure 27 – (a) Experimental multilevel RTN sginal. (b) Time Lag Plot showing 4 spots of well-defined current levels: L1, L2, L3, and L4. (c) The current histograms and the four Gaussian's means: μ_{L1}, μ_{L2}, μ_{L3}, and μ_{L4}.

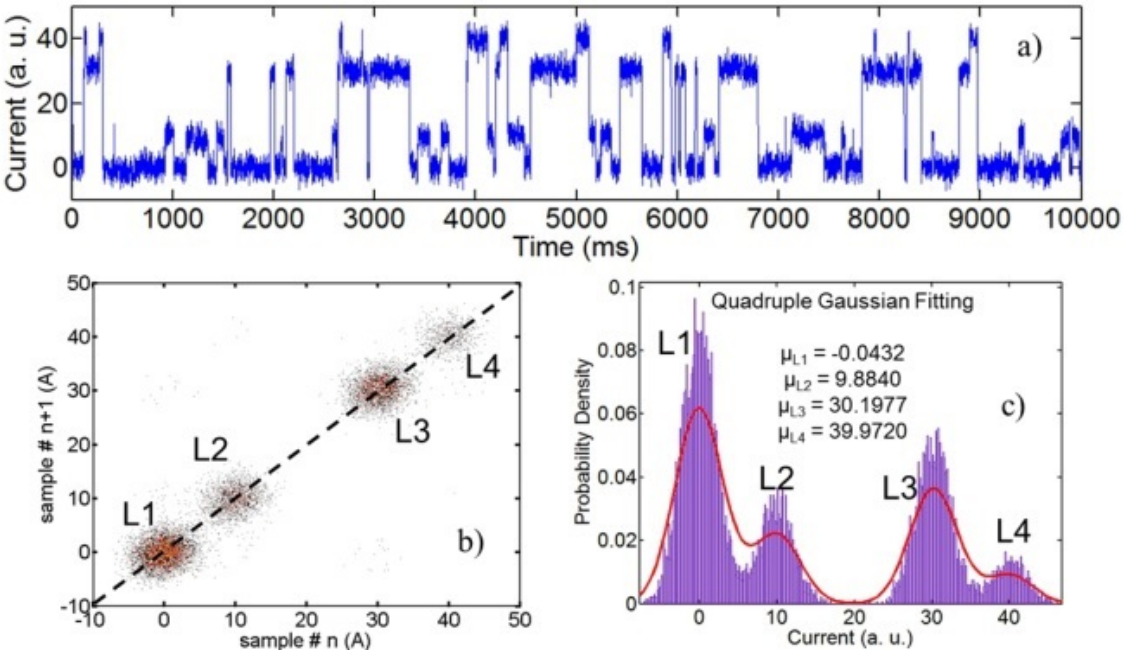

Source: (PUGLISI *et al.*, 2017).

Figure 28 – Graphic representation of an FHMM. At each instant of time t, the output Yt is related to the superposition of the states of M independent and parallel Markov chains.

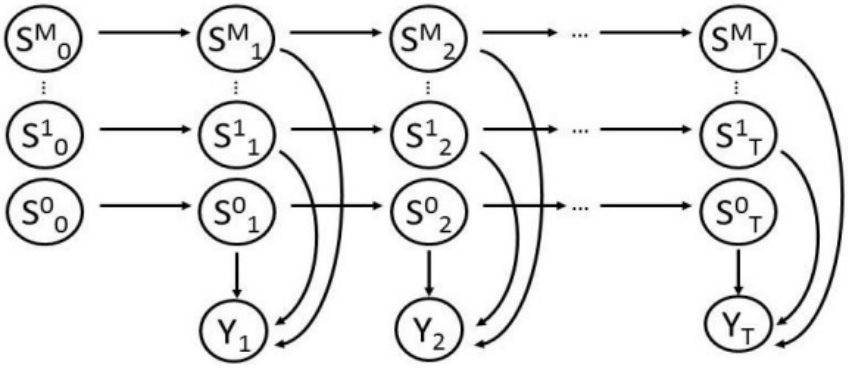

Source: (PUGLISI; PAVAN, 2013).

(2018) and PUGLISI *et al.* (2015). The correlation presented in the anomaulous 3-level RTN signal presented in Figure 29 exemplifies this challenge. In this case, the authors separately analyzed each portions of the I-time plot where the slow RTN signal is in the high-current state. Note that the behavior of the fast trap is precisely correlated to the state of the slow one. There is no established method or algorithm to analyze aRTN, although the recommendation is to separate the analysis by measurement intervals.

Figure 29 – Experimental 3-level RTN signal and the correlation between the fast and the slow trap.

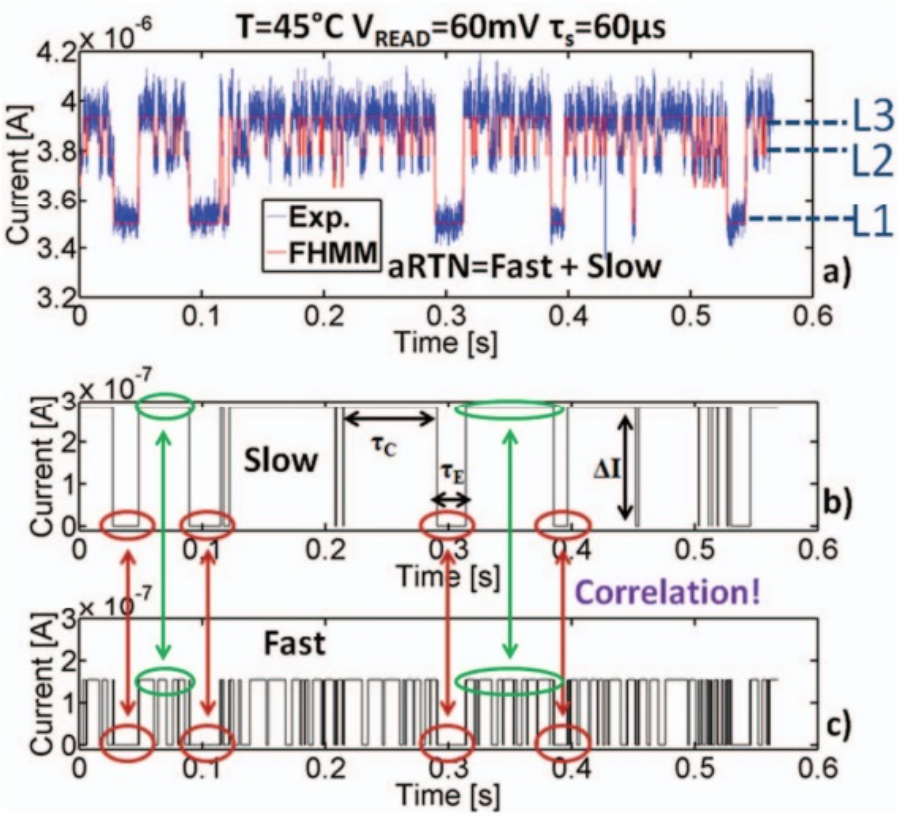

Source: (PUGLISI *et al.*, 2015).

5.2 Experiments and Analysis Setup

In this work, measurements were performed in cross-point MIM devices comprised of: Ni/TiO2/Au, Ni/HfO2/Au, and Ni/h-BN/Au MIM with active areas of 5 μm $\times$ 5 μm. The devices were fabricated by a partner group: the Institute of Functional Nano & Soft Materials at Soochow University, China. The fabrication process is as follows (LI *et al.*, 2021; SHI *et al.*, 2018). First, SiO_2 substrates of 1.5 cm $\times$ 1.5 cm were cleaned in acetone, alcohol, and deionized water, using ultra-sonication (99 W) for 20 minutes in each step. Then, 40-nm-thick Au bottom electrodes (with 10 nm Ti as adhesion layer underneath) were patterned by photolithography (Model MJB4, SUSS MicroTec), including metal deposition by electron-beam evaporator (model PVD75, Kurt J. Lesker) and lift off (rinse

the sample in acetone for 1 min to remove the photoresist). After that, in different set of samples, the TiO_2 (∼4 nm) and HfO_2 (∼4 nm) dielectrics were deposited by atomic layer deposition, and the h-BN (∼6 nm) layer was synthesized by chemical vapor deposition on a Cu foil and transferred on the bottom electrodes. Finally, 50-nm-thick Ni top electrodes were patterned via photolithography and sputtering (at 150 W for 30 minutes). The dedicated process is described in SHI *et al.* (2018) and LI *et al.* (2021). The estructure of the measured cross point devices is illustrated in Figure 30a. The samples were disposed in a matrix as shown in Figure 30b, zoomed at the devices active area, Figure 30c.

Figure 30 – (a) Schematic of cross-point MIM devices (b) A matrix of samples and (c) the optical image of a single device.

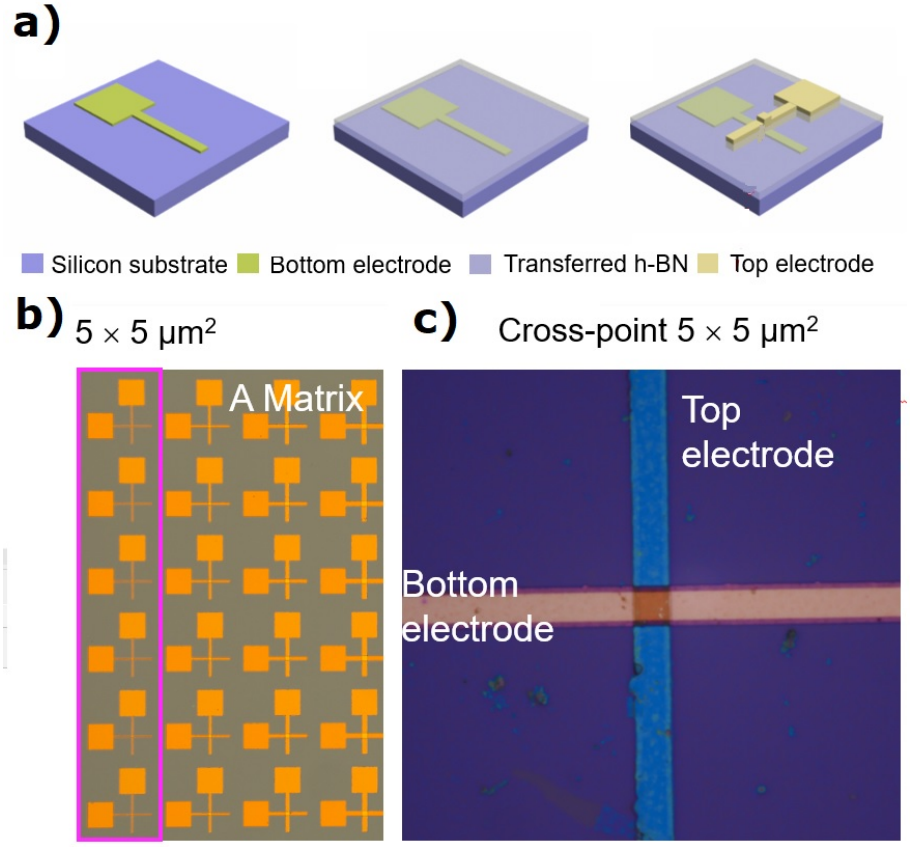

Source: Schematic Produced by the Institute of Functional Nano & Soft Materials at Soochow University.

The devices were characterized in the Laboratory of Electrical Characterization (LCE) at the University of Rio Grande do Sul (UFRGS). The MIM-like RS devices were measured using a probe station connected to a semiconductor parameter analyzer Agilent 4156A by applying a constant voltage to the top Ni electrode and measuring the current over the time. All measurements were executed in a dark environment at ambient atmosphere and at room temperature. The methodology that was employed to determine whether a device exhibits RTN was the standard recommended by the industry (LIU *et al.*, 2012). This methodology consists of applying a small voltage, after SET/RESET, that

produces a noisy current signal, and start to increase it until RTN-like behavior is observed. If no RTN signal is observed, then other stresses are applied to introduce defects in the dielectric; and after that, constant reading voltages of different magnitudes were applied again to try to observe RTN current signals. It is important to remark that the RTN properties displayed by different MIM-like RS devices cannot be compared by applying the same voltage to the different devices, as the RTN properties are strongly related to the microscopic properties of the defects involved (which differ in different material systems), and to the value of the electric field at the location of the defect involved in RTN (LI *et al.*, 2021).

To induce the SET/RESET in the samples, both procedures indicated in LANZA *et al.* (2019) were performed: (i) apply a ramped voltage stress (RVS) and observe the SET/RES in the current versus voltage (I$\times$V) sweeps; and (ii) apply a pulsed voltage stress (PVS), which matches the stresses applied to realistic devices, and simultaneously measure the drive current of the cell. As also recommended in LANZA *et al.* (2019), larger voltages were applied ($\sim$V) for the SET/RESET and reading voltages in the order of 0.1 V. In all induced SET/RESET, a current compliance (CC) in the μA-mA range was used in order to limit the energy delivered and avoid damages. These are the typical values of CC used in similar devices (RANJAN *et al.*, 2018; LANZA *et al.*, 2019; SHI *et al.*, 2018; LI *et al.*, 2021; LIN *et al.*, 2011).

5.3 Preliminar Characterization and Data Analysis

Our data showed that richer and more accurate information could be obtained if SET/RESET are performed using Constant Voltage Stress (CVS) rather than using the traditional IxV (butterfly/hysteresis) curves. In the traditional IxV curves the timing information is lost. SET/RESET point may depend on number of points in the trace (e.g.,voltage step) and measurement time (which may depend on equipament speed settings and/or current range). Since a pulse generator was not available, the CVS process was used to emulated the PVS behavior, as the constant voltage is applied in the samples with no previous bias. In the following Figure 31, examples of SET/RESET in CVS are shown, which is repeatedly seen in HfO_2, TiO_2, Figure 31a-b, and h-BN, Figure 31c-d, based samples. Note in Figure 31, for the TiO_2-based sample it takes a few hundred seconds to impose the SET, and to restore the HRS state, with the chosen applied voltages (0.6 V for the SET and -0.4 V for the RESET). Thus, in the following measurements, higher voltages were used to obtain obtain shorter SET/RESET times. HfO_2 presented a similar behavior compared to TiO_2 devices.

It is also important to remark that HfO_2- and, TiO_2-based samples presented a non-volatile character, i.e., long state retention times at reading voltage, while most h-BN presented a volatile character, i.e., short LRS retention times. This is exemplified in the

Figure 31 – SET/RESET performed using CVS (a,b) in TiO_2-based sample; SET imposed with 0.6 V and RESET imposed with -0.4 V. (c,d) in h-BN-based sample; SET imposed with 7 V and RESET imposed with -0.1 V.

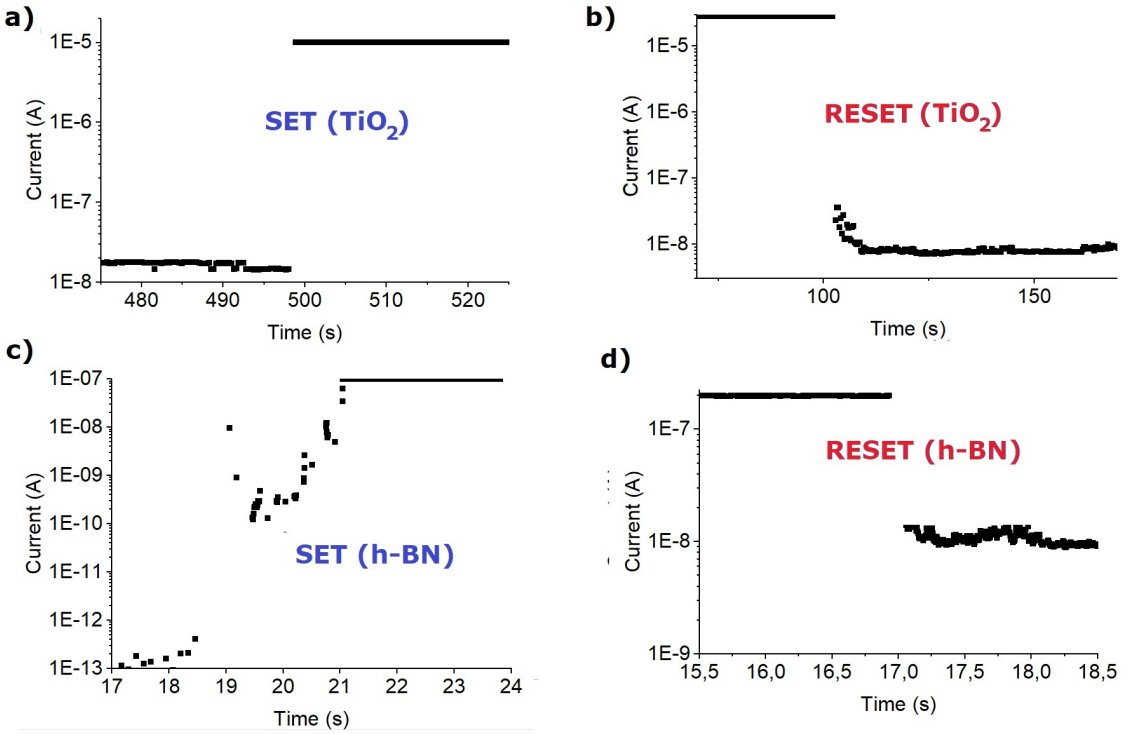

Source: The Author.

IxV (butterfly/characteristic) curve of a h-BN based sample, in Figure 32a. Note that the high-resistance state is restored when the voltage is reduced below a certain voltage magnitude, smaller than the SET write voltage. As discussed in Chapter 2, this behavior was already identified in similar h-BN based devices (SHI *et al.*, 2017; LANZA *et al.*, 2019). In this situation, a sequence of IxV SETs shown in Figure 32b can be used to continuosly SET the sample. This is another reason to use CVS rather than using the traditional IxV to SET/RESET h-BN samples.

Figure 32 – (a) The characteristic IxV curve of an h-BN based sample showing a volatile behavior.(b) Consecutive SET process applied in an h-BN based sample. Note that for each consecutive append; Append 0, Append 1, and Append 2, the LRS is continuously achieved.

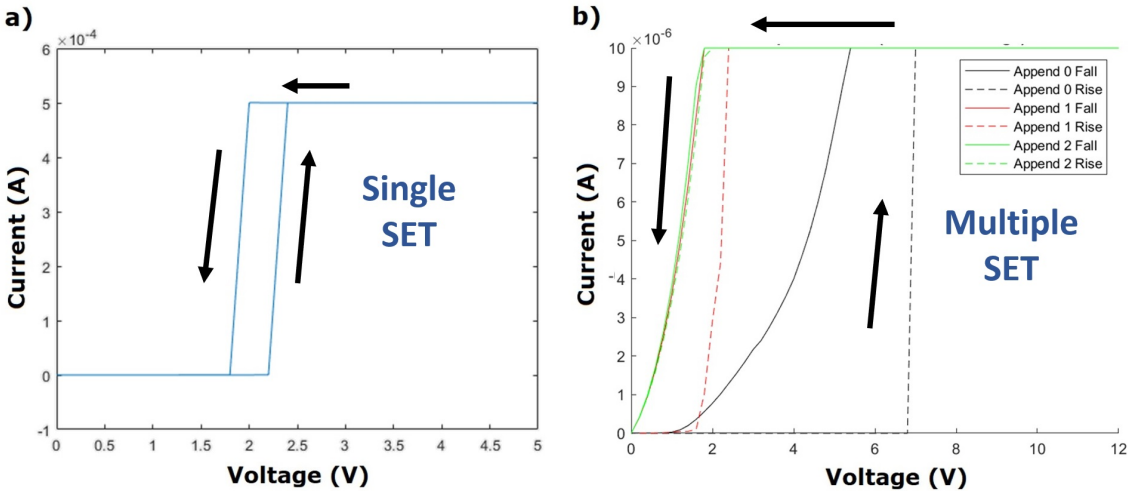

Source: The Author.

Also, TiO_2- and HfO_2-based samples displayed a non-polar behavior, i. e., SET and RESET can be achieved on both polarities, which is related to the metallic filament characteristic (LIN *et al.*, 2011; CORTESE *et al.*, 2016). In Figure 33, this is exemplified for HfO_2-based samples. Note that the SET can be obtained by a positive sweep voltage, Figure 33a, and by a negative sweep voltage, Figure 33b.

Data show that besides the *traditional RTN*, there are many concurrencies of anomalous and temporary RTN. We measured 150 samples, of which 85 presented RTN. Among those, 50 samples displayed anomalous RTN. As discussed in Chapter 3, traditional RTN is understood as the RTN in which each trap produces a 2-level RTN, see Figure 34. Note the sum of the activity of many traps may happen, but without interaction/coupling between traps. In the first set of experimental observations, coupling between traps seems to be present (see Figure 35). As discussed in Chapter 4, the coupling effect is associated to the traps that may be close to each other and interact electrostatically, or if a trap changes the percolation path interfering with the activity of a second trap on the same branch. Time-dependent RTN singals were also recorded, see Figure 36, showing traps

Figure 33 – HfO_2-based samples presenting a non-polar behavior. The sample is SET by a (a) positive sweep voltage and (b) negative sweep voltage.

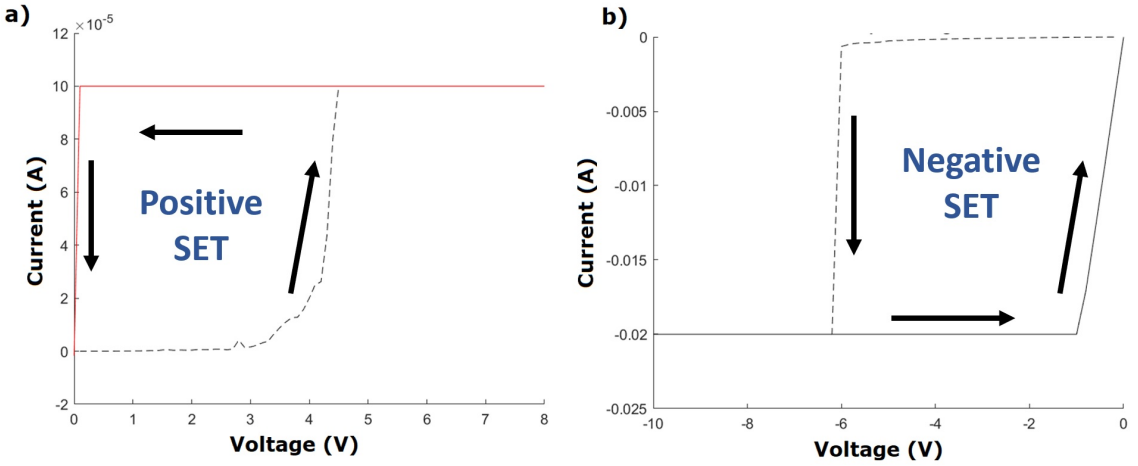

Source: The Author.

which repeatedly produce noise for random time intervals. Finally, apparent Giant RTNs were measured, showing fluctuations of multiple orders of magnitude, as shown in Figure 37. We identified 45 giant RTN measurements in 18 different samples.

It is important to remark that all the lower resistance levels measured in reading operation are not limited by the configuration of the semiconductor parameter analyser, i. e., the higher current levels are not determined or limited by the current compliance. Also, regarding the samples reliability, it was identified that the samples degrade over time, meaning that, typically, a novel SET operation is necessary to put the samples in LRS when accessed in different days. Also, it was identified that in long reading measurements (of a few hours) the SET is usually losted. This phenomenos can be related to temperature effects and joule heating.

Figure 34 – Experimental (a) traditional 2-level RTN and (b) traditional 4-level RTN in a h-BN based sample under a constant 100 mV applied voltage in LRS state.

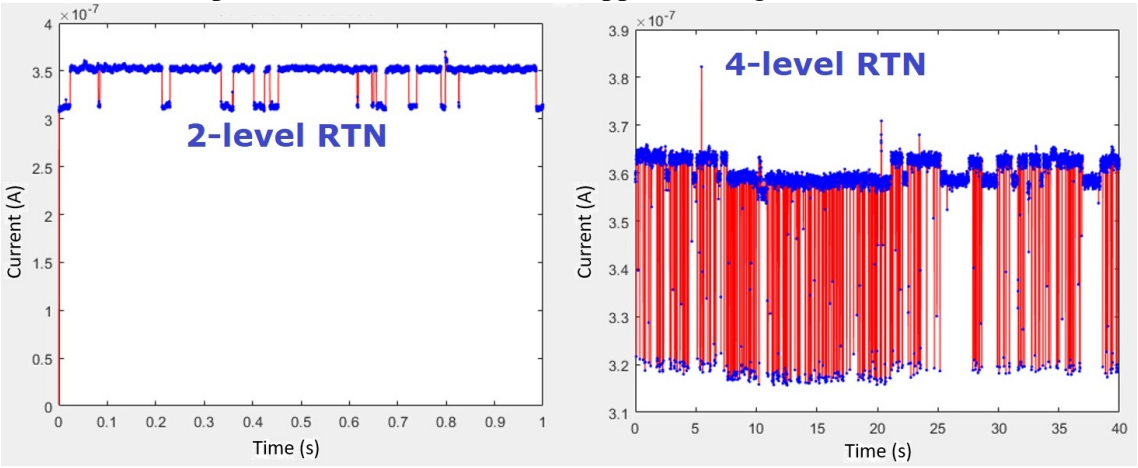

Source: The Author.

Figure 35 – (a) Experimental aRTN in a TiO_2-based sample under a constant 200 mV applied voltage in HRS state. Note that there are zones of "normal" 2-level RTN and other zones with apparent coupling trap.

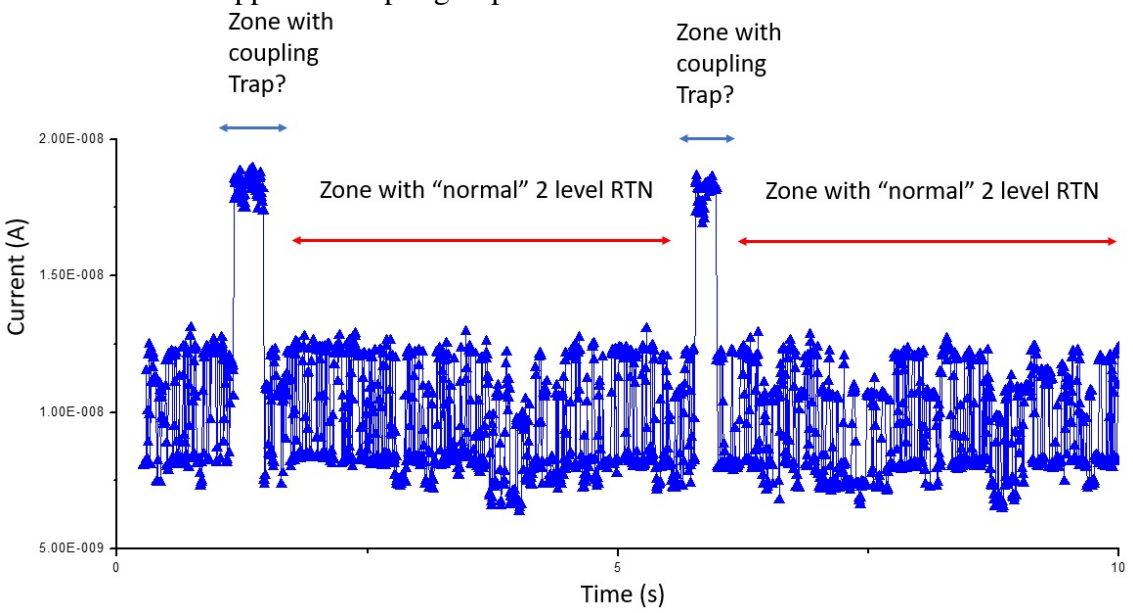

Source: The Author.

Figure 36 – (a) Experimental tRTN in a TiO_2-based sample under a constant 500 mV applied voltage in HRS state. Note that the current fluctuation appeared and dissapeared during the measurement window time.

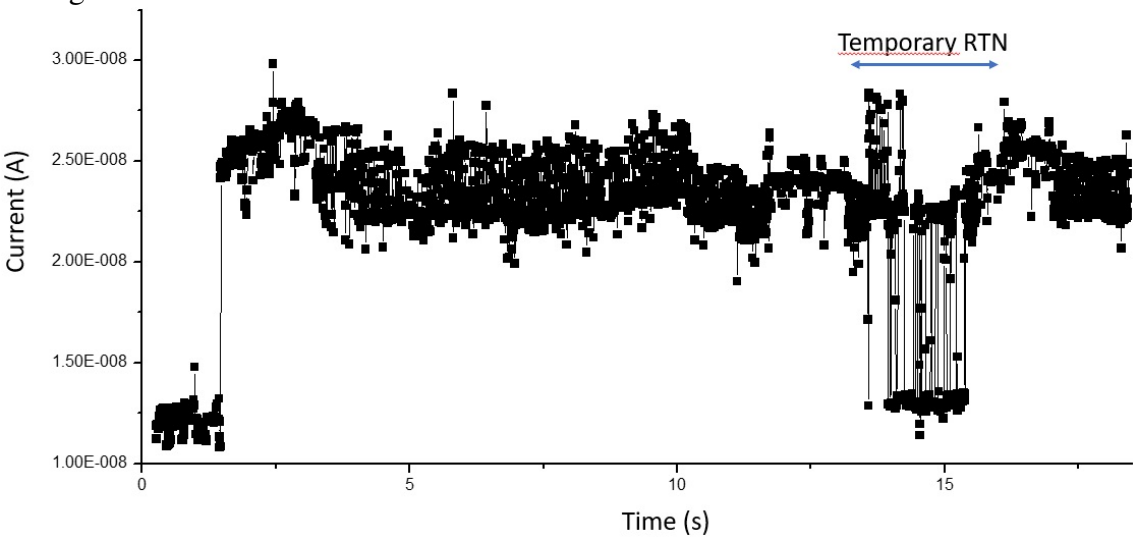

Source: The Author.

Figure 37 – (a) An apparent experimental giant RTN recorded for a HfO_2-based sample under 50 mV applied voltage. Note that a continuous increase of current is observed in the lower current level. This degradation phenomenon is not related to trapping activity and is not observed in the higher conductance level, as, in such case, the orders of magnitude of current are much higher. In this work, we are interested in the RTN phenomenon, i. e., the giant discrete jumps of conductance presented in such measurements.

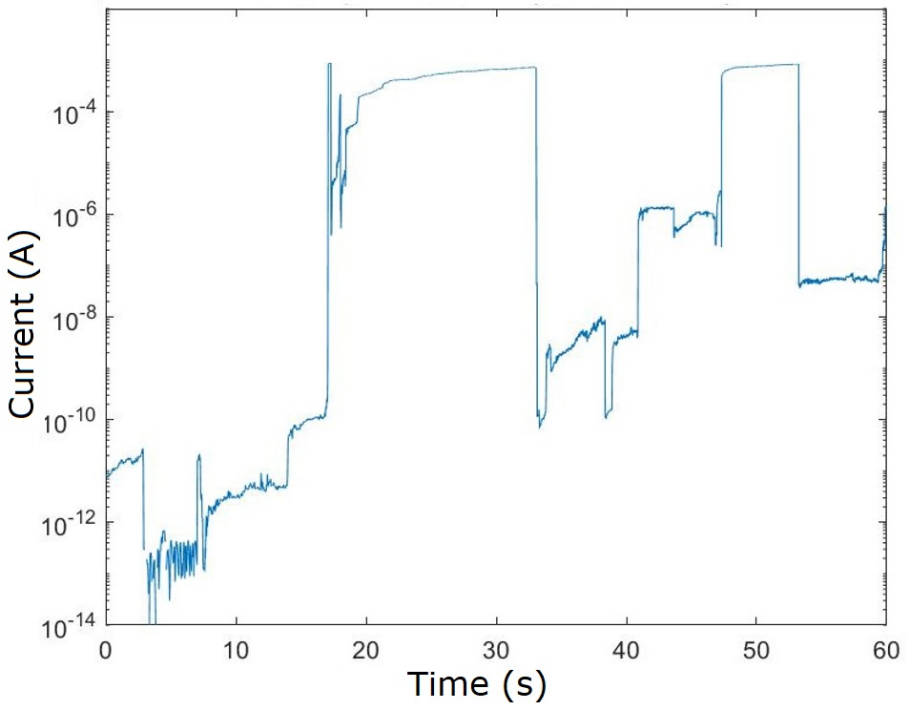

Source: The Author.

Considering this, an algorithm was developed to extract the RTN signal parameters in the presence of Gaussian (white) noise (DA SILVEIRA *et al.*, 2021). The algorithm performs the extraction of RTN signal parameters from synthetic and experimental data measured in electronic devices. At first, the well-defined levels are identified, from the gaussians in the current occurrence plot. Then, it searches for the RTN current swings to determine where the transitions start and end. Right after that, the individual realizations of $\tau_{c,e}$ are used to visually validated the RTN parameters by fitting the calculated values to the experimental data, as shown in Figure 38.

Figure 38 – Experimental 2-level RTN fitted by the algorithm that extract the RTN signal parameters.

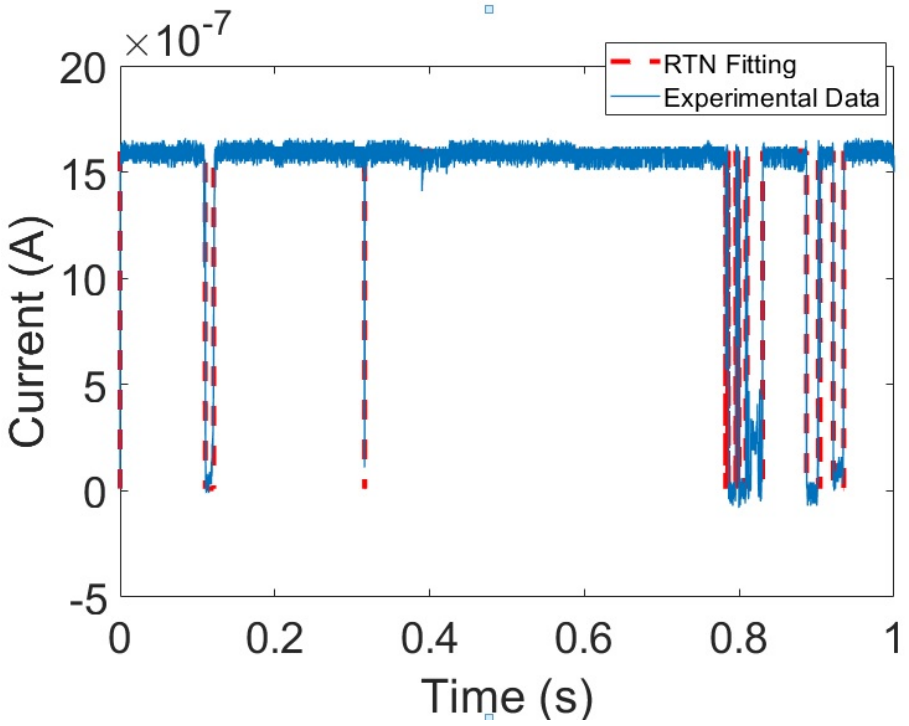

Source: The Author.

In this work, the experimental results show evident defect coupling effects. We measured 150 samples, of which 85 presented RTN. Among those, 50 samples displayed anomalous RTN. From these observations, an electrical trap coupling model was developed and compared to experimental current vs time (I-t) plots collected in Ni/TiO_2/Au, Ni/HfO_2/Au ,and Ni/h-BN/Au cross-point devices; and similar aRTN reported in the literature in the context of *MOSFET* and *FinFET* devices (WANG *et al.*, 2018; ZHANG *et al.*, 2018). Additionally, this work explored the giant RTN signal observed at reading operation, which were stable in the aforementioned cross-point devices. We identified 45 giant RTN measurements in 18 different samples. We also modeled this behavior, in chapter 7, assuming the surface-relaxation model in narrow conductive filaments (IELMINI; NARDI; CAGLI, 2010).

6 TRAP COUPLING MODEL

6.1 Experimental

I-t plots at different constant voltages were collected in cross-point Ni/TiO_2/Au and Ni/h-BN/Au MIM devices with active areas of 5μm $\times$ 5μm, fabricated using photolithography, electron beam evaporator (for Au deposition) and sputtering (for Ni deposition). The TiO_2 film was 4-nm thick and was synthesized by atomic layer deposition, and the h-BN sheet was 5-nm thick and was synthesized via chemical vapor deposition on Cu and transferred on the target wafers. The MIM-like RS devices were measured using a probe station connected to a semiconductor parameter analyzer Agilent 4156A by applying a constant voltage to the top Ni electrode and measuring the current over the time.

6.2 Coupling Trap Model

The goal is to present the simplest possible model that captures the essence of defect coupling in a percolation path. It is particularly useful and instructional that the minimalist model correctly reproduces the observations and several data in the literature. In devices that display this characteristic, the current should flow preferably through paths of low electrical resistance. This is the typical situation for the current flow in dielectrics, such as those employed in MIM-like RS devices. This should also be the case in MOSFETs and FinFETs, in which the effects of Random Dopant Fluctuations (RDF) and RTN are present(ASENOV *et al.*, 2001; FAN *et al.*, 2014).

From this, a simple model is proposed for trap coupling in CFs formed across the insulator of MIM-like RS devices. First, we assume that the electrical field may not be constant over the dielectric. Then the electrical potential at the trap site is not solely a function of trap distance from the electrodes. Furthermore, the electrical potential at a trap site may change if other traps are occupied, as presented in the trap coupling models in the next subsections. If the CF across the insulator is not homogeneous, percolation paths may be formed and abstracted as a network of electrical resistances, which can be dynamically affected by capture and emission activity. Particularly, the different branches may be arranged in series (see T_{S1} and T_{S2} in Figure 39a) or in parallel (see T_{P1} and

T_{P2} in Figure 39b). The measured MIM-like RS devices displayed RTN behavior that not only is consistent with trap coupling, but also could be modeled using the proposed methodology. It is worth noting that the proposed model is not restricted to the case of two traps and MIM-like RS devices. As discussed in Chapter 4, similar behavior has been recorded in *MOSFET* and *FinFET* devices.

Figure 39 – Schematics displaying the proposed models for (a) series coupling of traps (T_{S1} and T_{S2}), i.e., **Series Coupling Traps Model (SCTM)**, and (b) parallel coupling of traps (T_{P1} and T_{P2}), i.e., **Parallel Coupling Traps Model (PCTM)**. R_{S1} and R_{S2} refer to the series resistances at the branches of traps T_{S1} and T_{S2} (respectively), and R_{P1} and R_{P2} refer to the parallel resistance at the branches of traps T_{P1} and T_{P2} (respectively). The orange spheres represent active defects. The suffixes *EMP* and *OCC* refer to the value of the resistances (either series or parallel) when the active defect is empty and occupied (respectively). This is the simplest electrical model that can handle two coupling traps, with the smallest number of resistances.

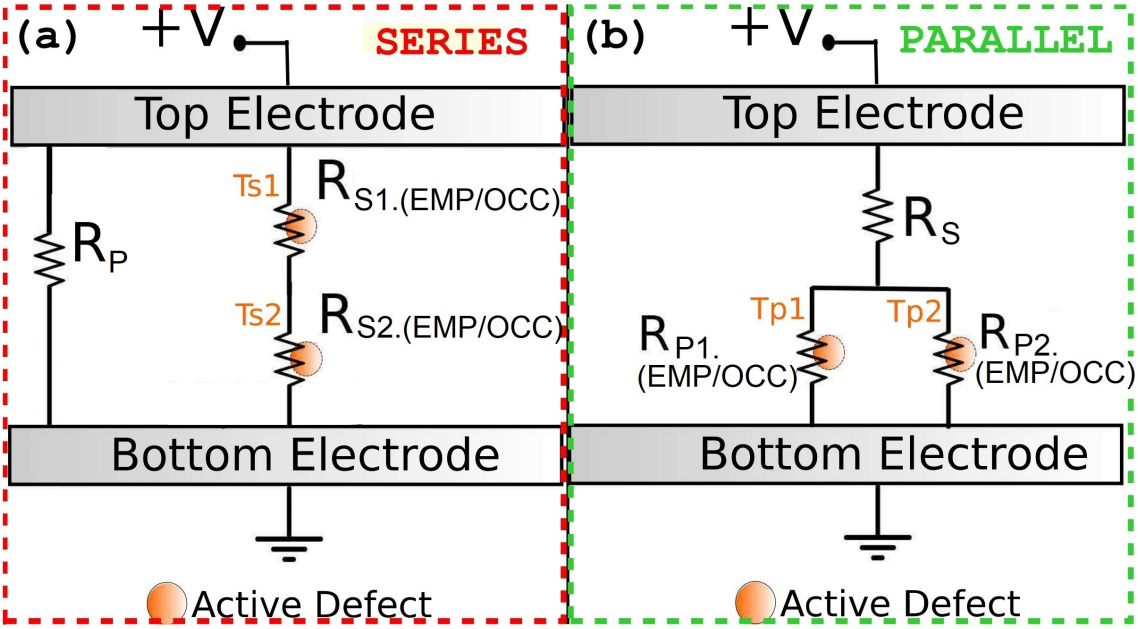

Source: The Author.

In essence, we investigate aRTN with coupled amplitude, i.e., when the amplitude of one trap is affected by the occupancy state of another. If the amplitude decreases, we consider it to be a **negative coupling effect**, see Figure 40a, and if the trap amplitude increases, we consider it to be a **positive coupling effect**, see Figure 40b.

6.2.1 Series Coupling Traps Model

The states of T_{S1} and T_{S2} may modify the filament resistances R_{S1} and R_{S2}, due to Coulomb blockade of a portion of the filament in LRS, and due to multiphonon-trap-assisted tunneling mechanism in HRS, as presented in Chapter 3. The resistance $R_{S1.EMP}$, related to T_{S1} in its empty state, is lower than $R_{S1.OCC}$, related to T_{S1} in its occupied state.

Figure 40 – a) When T_{S2} occupies, its resistance increases. Therefore, the voltage drop in T_{S1} decreases and consequently the current oscillation (ΔI) produced by T_{S1} is smaller when T_{S2} is occupied (ΔIHigh $>$ ΔILow). (b) When T_{P2} occupies, its resistance increases. Thus, the voltage drop in T_{P1} also increases. Therefore, the current oscillation (ΔI) produced by T_{P1} is higher when T_{P2} is occupied (ΔILow $>$ ΔIHigh). T_{S1} and T_{P1} are the faster traps.

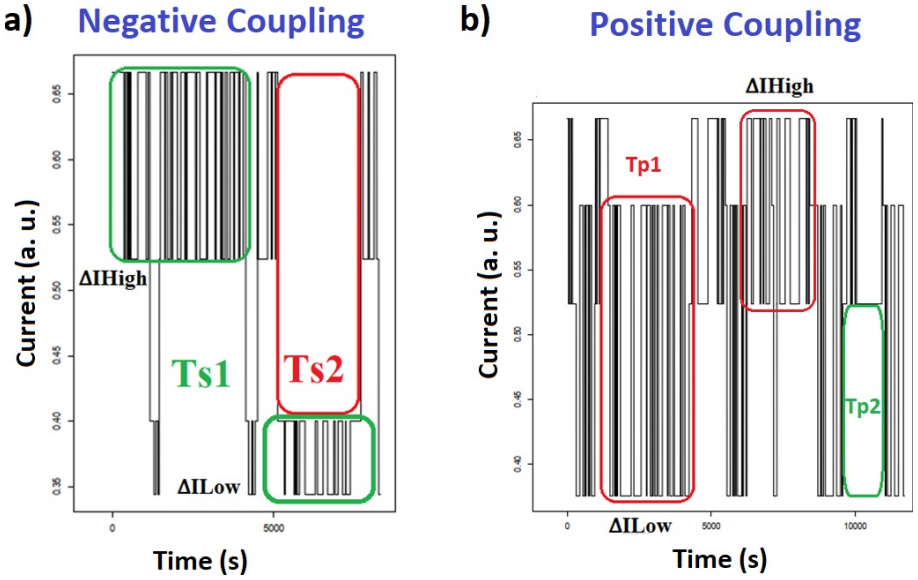

Source: The Author.

The same occurs for T_{S2} and its associated resistances, i.e. $R_{S2.EMP} < R_{S2.OCC}$. Let us now assume that T_{S1} switches faster than T_{S2} for analysis purposes. When T_{S2} changes from *EMP* state to *OCC* state, R_{S2} increases, as well as its voltage (VR_{S2}). At the same time, this state transition reduces the total current flowing along the CF and the voltage of R_{S1} (VR_{S1}). Therefore, the current variation produced by T_{S1} is impacted by the switching activity of T_{S2}, and it is less significant when T_{S2} is occupied. This case can be referred as negative coupling amplitude effect.

The described behavior has been experimentally observed in Ni/TiO_2/Au devices. As Figure 41a shows, the current fluctuates between four well-defined levels. Figure 41b shows the current histograms and the four Gaussian means: μ1, μ2, μ3, and μ4. Considering the applied voltage, it is possible to estimate the equivalent resistance histogram, and its four Gaussian means: μR1, μR2, μR3, and μR4, depicted in Figure 41c. The negative coupling behavior is verified because the value of ΔI_{HIGH} = 59 nA, is approximately *20*% greater than ΔI_{LOW} = 49 nA. This contradicts the established regular multi-level RTN definition, presented in Chapter 3, where we expect the two Gaussian pairs to have the *same* difference between their averages.

It is also important to remark that previous works report irreversible current jumps, caused by ion migration in the insulator of MIM-like RS devices. Such events occur even when the MIM cell operates under a low read voltage. This effect is recurrently referred

to as Random Walk (AMBROGIO *et al.*, 2015; CHAI *et al.*, 2017) and differs from our experimental observations in which the currents oscillate between well-defined levels, as seen in Figure 41a, showing reversible RTN signals.

Figure 41 – (a) Experimental aRTN in a TiO_2 based sample under a constant 200 mV applied voltage in HRS state. (b) Current discrete levels estimation and (c) Resistance discrete levels estimation for the plot in panel (a). (d) SCTM Current Fitting.

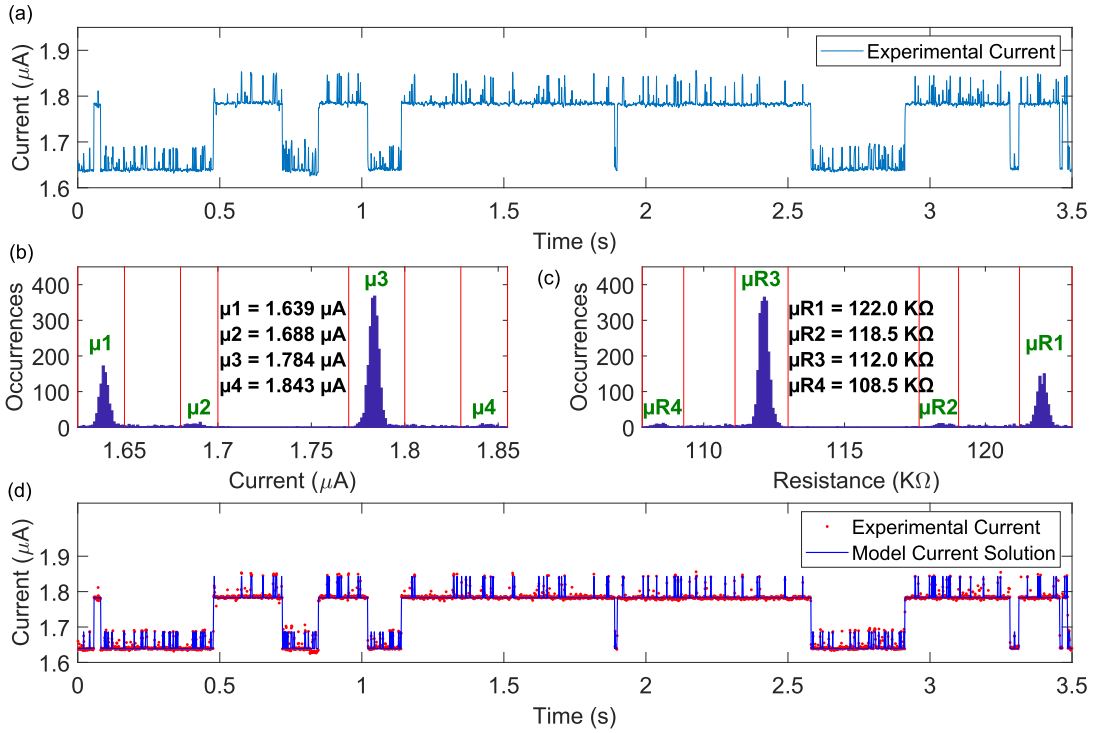

Source: The Author.

Considering the four well-defined current states are associated to the applied voltage (V) and the possible states $R_{S1.OCC}$, $R_{S1.EMP}$, $R_{S2.OCC}$, and $R_{S2.EMP}$, the current can be obtained from the system of equations in (3).

$$I_{StateS1/StateS2} = \frac{V}{Req_{StateS1/StateS2}} = \frac{V}{(R_{S1.(EMP/OCC)} + R_{S2.(EMP/OCC)})//R_P} \quad (3)$$

The equation system derived from (3) is comprised of (4), (5), (6), and (7).

$$Req_{OCC/OCC} = \mu R1 = R_{S1.OCC} + R_{S2.OCC}//Rp \quad (4)$$

$$Req_{OCC/OCC} = \mu R2 = R_{S1.EMP} + R_{S2.OCC}//Rp \quad (5)$$

$$Req_{OCC/OCC} = \mu R3 = R_{S1.OCC} + R_{S2.EMP}//Rp \quad (6)$$

$$Req_{OCC/OCC} = \mu R4 = R_{S1.EMP} + R_{S2.EMP}//Rp \quad (7)$$

For the general case, the equation system composed of the four possible states of (3) is numerically solved to estimate the resistance parameters: $R_{S1.EMP}$, $R_{S2.EMP}$, $R_{S1.OCC}$, and $R_{S2.OCC}$. Successive iterations are performed until a solution that satisfies a lowest mean deviation (εM) from the experimental parameters is found. The iteration goes on until it converges to a solution with εM orders of magnitude lower than the smallest output resistance. Please note that multiple solutions may exist. Values presented here are the ones used to fit data to model, which does not mean they are better than the other possible solutions. In the particular case in which the resistance changes ΔR_{HIGH} = (μR3 - μR4) and ΔR_{LOW} = (μR1 - μR2) are equal, as in Figure 41c, $R_P -> \infty$ (R_P becomes an open circuit), and the SCTM model is simplified removing R_P. In this context, the equation system derived from (3) becomes linear and also has multiple solutions. The algorithm and the adopted procedures are better described in Annex A.

Despite being impossible to define a unique solution for the resistance parameters, in the framework of Figure 41, we can determine directly from the equivalent resistance histogram, Figure 41c, both resistances changes univocally, ΔR_{S1} = $R_{S1.OCC}$ - $R_{S1.EMP}$ = μR3 - μR4 and ΔR_{S2} = $R_{S2.OCC}$ - $R_{S2.EMP}$ = μR2 - μR4. Also, in this scenario, it is possible to establish ranges (upper and lower bounds) for the resistance parameters. Through this, for Figure 41c, we got ΔR_{S1} = 3.5 KΩ and ΔR_{S2} = 10 KΩ. From the extracted parameters the experimental I-t curve (Figure 41a) was successfully fitted using our model (Figure 41d) by the solution set $R_P -> \infty$ KΩ, $R_{S1.EMP}$ = 48.5 KΩ, $R_{S1.OCC}$ = 52 KΩ, $R_{S2.EMP}$ = 60 KΩ, and $R_{S2.OCC}$ = 70 KΩ.

In the next subsection the positive coupling amplitude effect is discussed.

6.2.2 Parallel Coupling Traps Model

The states of T_{P1} and T_{P2} also modify the filament resistances R_{P1} and R_{P2}. Let us now assume T_{P1} switches faster than T_{P2} for analysis purpose. When T_{P2} changes from *EMP* state to *OCC* state, R_{P2} increases. Consequently, the voltages on both R_{P1} and R_{P2} (VR_{P1} and VR_{P2}, respectively) also increase. Therefore, the current deviation produced by T_{P1} is impacted by T_{P2} activity and is more significant when T_{P2} is occupied. This case can also be referred as positive coupling amplitude effect. The described behavior has been experimentally observed in Ni/TiO_2/Au devices, as shown in Figure 42a. Once again a reversible current jump is presented, characterizing a RTN signal. The current histograms and the four Gaussian means: μ1, μ2, μ3 and μ4, are shown in Figure 42b. The positive coupling amplitude is verified because ΔI_{LOW} = μ2 - μ1 = 3.44 nA is almost five times greater than ΔI_{HIGH} = μ4 - μ3 = 0.69 nA. Considering the four well-defined current states are associated to the applied voltage V and the possible states $R_{P1.OCC}$, $R_{P1.EMP}$, $R_{P2.OCC}$, and $R_{P2.EMP}$, the current can be obtained from the system of equations derived

from (8).

Figure 42 – (a) Experimental aRTN in a TiO_2 based sample under a constant 20 mV applied voltage in HRS state. (b) Current discrete levels estimation. (c) SCTM Current Fitting and (d) Concurring equivalent resistances discrete levels for the same sample under constant 20 mV and 30 mV applied voltages.

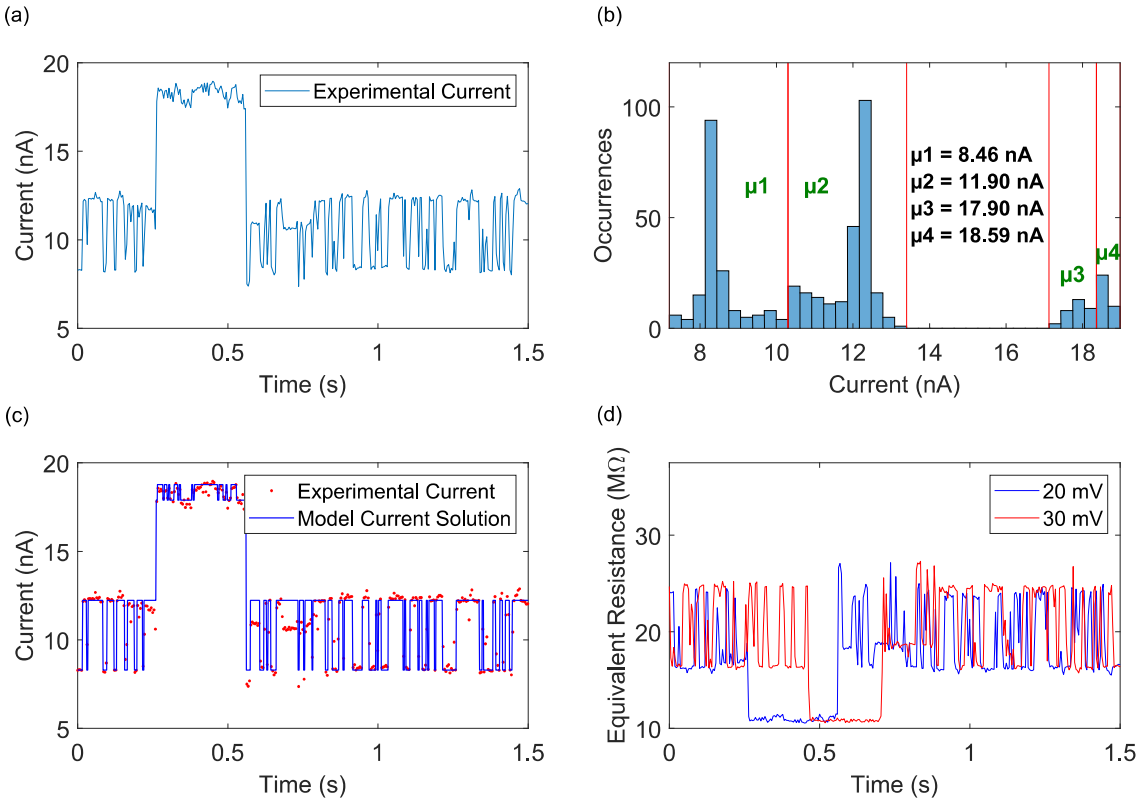

Source: The Author.

$$I_{StateS1/StateS2} = \frac{V}{Req_{StateS1/StateS2}} = \frac{V}{R_S + (R_{P1.(EMP/OCC)} // R_{P2.(EMP/OCC)})} \quad (8)$$

The equation system derived from (8) is comprised of (9), (10), (11), and (12).

$$Req_{OCC/OCC} = \mu R1 = Rs + (R_{P1.OCC} // R_{P2.OCC}) \quad (9)$$

$$Req_{OCC/OCC} = \mu R2 = Rs + (R_{P1.EMP} // R_{P2.OCC}) \quad (10)$$

$$Req_{OCC/OCC} = \mu R3 = Rs + (R_{P1.OCC} // R_{P2.EMP}) \quad (11)$$

$$Req_{OCC/OCC} = \mu R4 = Rs + (R_{P1.EMP} // R_{P2.EMP}) \quad (12)$$

The equation system composed of the four possible states of (8) was numerically solved to estimate the resistance parameters: $R_{P1.EMP}$, $R_{P2.EMP}$, $R_{P1.OCC}$, and $R_{P2.OCC}$..

Successive iterations were performed and the iteration goes on until it converges to a solution with εM orders of magnitude lower than the smallest output resistance. In the PCTM, the solution for R_S is unique, and the other ones have multiple solutions, being possible to establish ranges (upper and lower bounds) for their values. Values presented here are the ones used to fit data to model, which does not mean they are better than the other possible solutions. The algorithm and the adopted procedures are better described in Annex A.

From the aforementioned process we obtained two possible solution intervals. The first interval is given by ΔR_{P1} = ($R_{P1.OCC}$/$R_{P1.EMP}$) > ΔR_{P2} = ($R_{P2.OCC}$/$R_{P2.EMP}$)), which leads to εM = 1 nΩ and the solution set R_S = 809 KΩ, $R_{P1.EMP}$ = 1.978 MΩ, $R_{P1.OCC}$ = 745.242 MΩ, $R_{P2.EMP}$ = 308 KΩ, and $R_{P2.OCC}$ = 1.558 MΩ. The second interval is given by $\Delta R_{P2} > \Delta R_{P1}$, which leads to εM = 50 nΩ and the solution set R_S = 809 KΩ, $R_{P1.EMP}$ = 872 KΩ, $R_{P1.OCC}$ = 1.55 MΩ, $R_{P2.EMP}$ = 384 KΩ, and $R_{P2.OCC}$ = 653 MΩ. Even though a unique solution set is impossible, we remark that in this case, ΔR_{P1} and ΔR_{P2} present similar orders of magnitude in the two counterpart intervals. From the extracted parameters the experimental I-t curve Figure 42a was successfully fitted using our model (Figure 42c). Also, for the same sample the current was recorded under 30 mV. Figure 42d presents a strong evidence that the same defects are active during both measurements since the resistance oscillates between the same defined levels.

6.2.3 Temporary RTN

If the series trap resistance is significantly larger than the parallel branch under empty traps, an apparent temporary RTN may be observed, as seen in Figure 43a. This can be modeled by PCTM (39b) in the context that all the equivalent resistance levels are very similar to R_S, except by μR1, which must be larger. To achieve that, R_S must be be orders of magnitude larger than both empty resistances ($R_{P1.EMP}$ and $R_{P2.EMP}$). Through this, it is possible to estimate the parameters to build the I-t fitting curve, as presented in Figure 43b by the solution set: R_S = 1.82 MΩ, $R_{P1.EMP}$ = 32 KΩ, $R_{P1.OCC}$ = 2.28 MΩ, $R_{P2.EMP}$ = 32 KΩ, $R_{P2.OCC}$ = 2.44 MΩ.

Also, considering that a series resistance branch drastically increases by trapping activity, it may almost block the current flow through the whole branch. In this case a second trap (eventually located downwards or upwards the branch) may have negligible effect on current conduction. This may lead to an apparent transient RTN as presented in Figure 43c. This situation can be modeled by the SCTM (Figure 39a) in the context that μR4 (both traps are empty) are much smaller than the other resistances levels. Therefore, both $R_{S1.OCC}$ and $R_{S2.OCC}$ must be orders of magnitude larger than $R_{S1.EMP}$ and $R_{S2.EMP}$. Finally, in this same framework, but considering that a parallel resistance exists, i. e., R_P is significantly smaller than the serial branch under occupied traps, this may lead to an apparent transient RTN as seen in Figure 43d. This situation can be modeled by the

Figure 43 – (a) Experimental I-t curves measured in the Ni/TiO_2/Au devices under V = 20 mV, in HRS. (b) shows the fitting of (a) using the PCTM. (c) and (d) Experimental I-t curves measured in the Ni/h-BN/Au devices under V = 100 mV, in LRS. (e) shows the fitting of (c) and (f) shows the fitting of (d) using the SCTM.

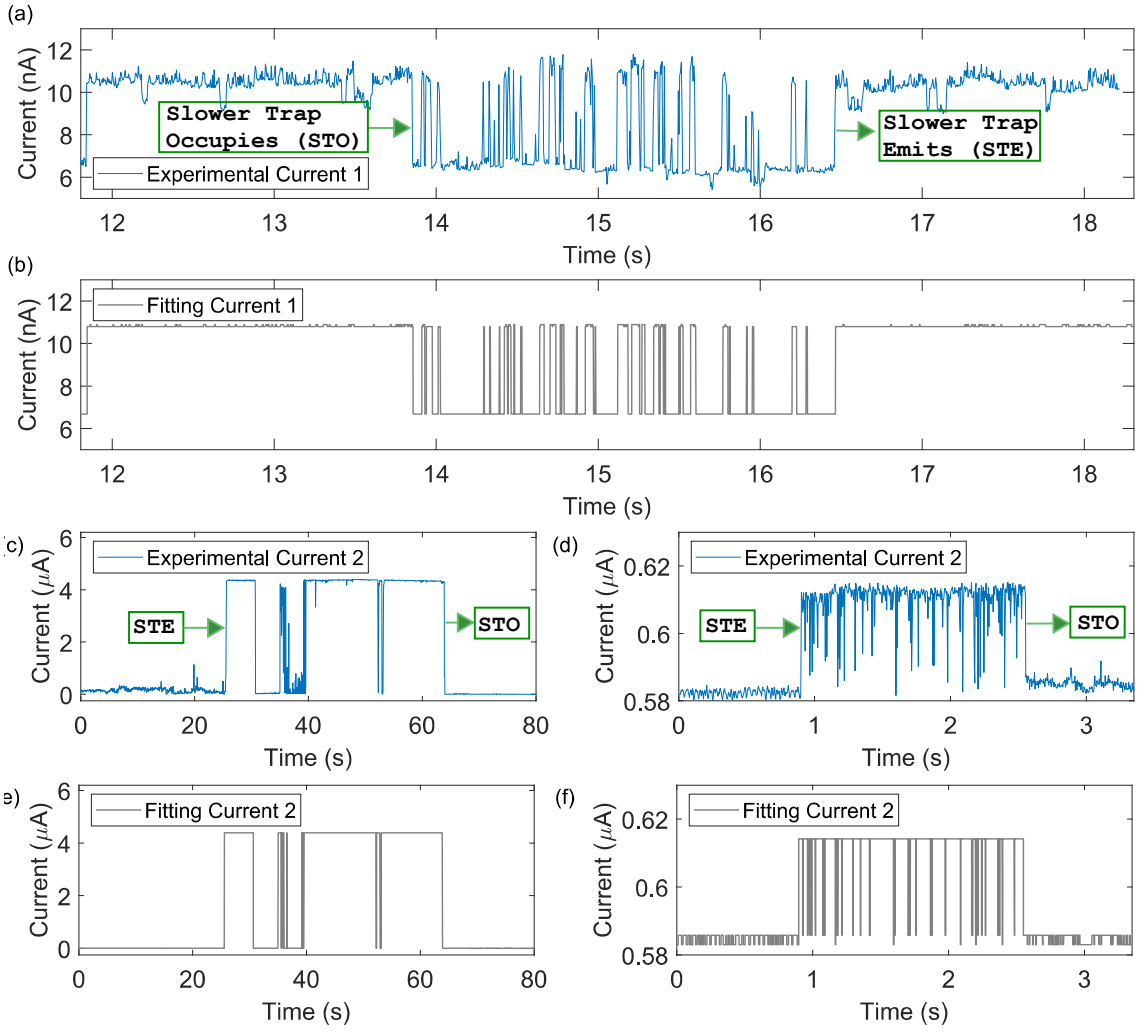

Source: The Author.

SCTM (Figure 39a), in the context that both occupied resistances ($R_{S1.OCC}$ and $R_{S2.OCC}$) are orders of magnitude larger than R_P. Through this, it is possible to estimate the parameters to achieve the behavior of the aforementioned cases and to build the I-t fitting curves, as presented in Figure 43e and Figure 43f by the respective solution sets: $R_P -> \infty$ Ω, $R_{S1.EMP}$ = 4.8 KΩ, $R_{S1.OCC}$ = 10 MΩ, $R_{S2.EMP}$ = 18 KΩ, and $R_{S2.OCC}$ = 50 MΩ; R_P = 172.5 KΩ, $R_{S1.EMP}$ = 1.4 MΩ, $R_{S1.OCC}$ = 15 MΩ, $R_{S2.EMP}$ = 1.5 MΩ, and $R_{S2.OCC}$ = 15 MΩ.

6.2.4 3-level RTN

Defect coupling has also been observed by other groups in the context of 3-level RTN. These results from the literature will be here discussed in this section under the framework of the proposed trap coupling electrical model.

Such behavior appears in PUGLISI *et al.* (2016), in which a RTN with 3 different well-defined levels was obtained (see Figure 44). This behavior is not explained by traditional multilevel RTN definition, as discussed in Chapter 4. In PUGLISI *et al.* (2016), this measurement is modeled by charges diffusion resulting in a physical interaction between oxygen vacancies (Vo) and neutral oxygen interstitial (NOI). The assumption is that the activity of a fast defect, such as Vo, could be suddenly interrupted by a Coulomb blockade effect, caused by the occupied NOI. We show that this behavior can also be modeled by a simple series trap arrangement, such as presented in Figure 39a. In this case, Level 1 can be the result of a negative coupling, i.e., the amplitude of a trap (ΔI) decreases if if a neighbor trap is occupied.

Figure 44 – Experimental Anomalous RTN in a HfO_2 based sample under a constant 60 mV applied voltage.

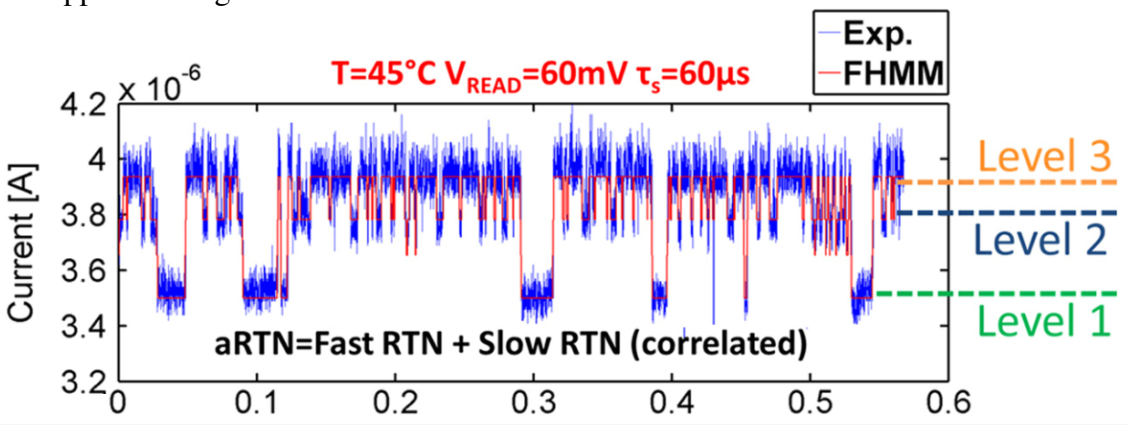

Source: Adapted of PUGLISI *et al.* (2016).

The equivalent resistances (Req), measured between the top and bottom electrode, are obtained by the relation between the applied voltage and the current levels presented in Figure 44: $I_{EMP/EMP}$ = 3.9 μA, $I_{EMP/OCC}$ = 3.8 μA, $I_{OCC/EMP}$ = 3.56 μA, and $I_{OCC/OCC}$ = 3.55 μA. The equation system composed of the four possible states derived

of (3) is numerically solved. Please note that multiple solutions exists. In Table I, two examples of solution sets are presented. Even though a unique solution set is impossible, we remark that in this case, $R_{S2.OCC}$ is always orders of magnitude larger than Rp, which always converges to a similar value that corresponds to the higher equivalent resistance level, related to Level 1 (Figure 44). Values presented in Solution 1, with a mean error εM= 100Ω, are the ones used to fit data to model, which does not mean they are better than other possible solutions.

Table 1 – Solution Parameters for 3 level RTN measuered in HfO_2-based sample.

Parameter	**Solution 1**	**Solution 2**
Rp	17 KΩ	17 KΩ
$R_{S1.EMP}$	102,7 KΩ	149 KΩ
$R_{S1.OCC}$	160,0 KΩ	209 KΩ
$R_{S2.EMP}$	57.9 KΩ	12.9 KΩ
$R_{S2.OCC}$	1.75 MΩ	2.42 MΩ

From the extracted parameters it was possible to plot the current-over-time fitting curve, Figure 45, that corresponds, in terms of amplitude fluctuation, to the experimental data observed in Figure 44. Notice the data in this analysis was obtained from the literature; hence, the time constants of the fitting current had to be arbitrarily approximated considering a fitting standpoint and assumed to be in an exponential distribution, making T_{S2} emission/capture time constants (165 ms/ 66 ms) greater than T_{S1} ones (3 ms/ 16 ms).

Figure 45 – Series Coupled Traps Model Current Fitting that corresponds, in terms of amplitude fluctuation, to the experimental data observed in Figure 44.

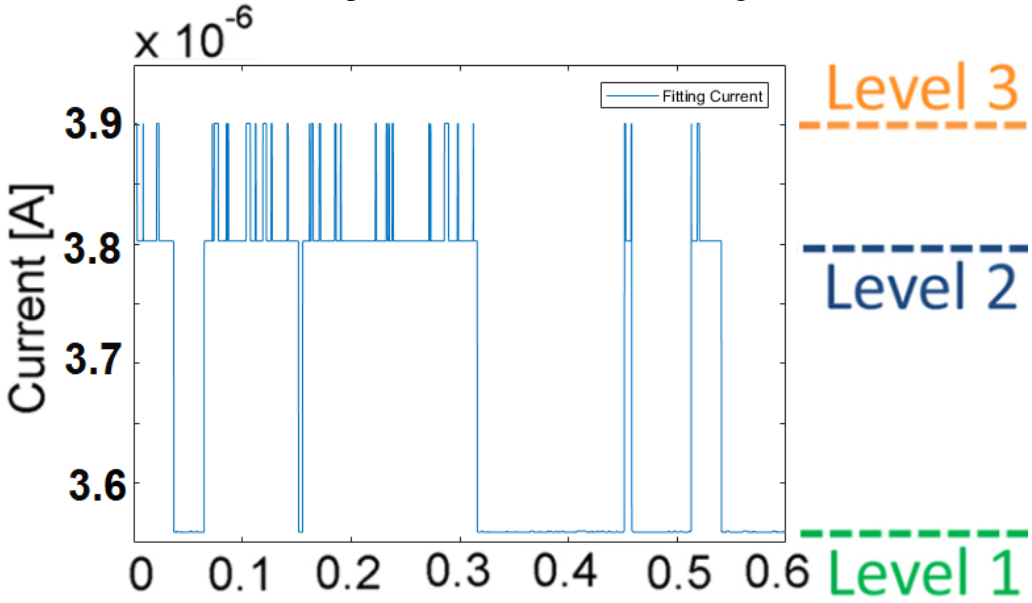

Source: The Author.

A similar behavior is also exemplified by a measurement presented in GONG *et al.*

(2018) for a TMOx-based resistive switching memory (TMOxRAM), shown in Figure 46a. In this case, however, a positive coupling amplitude effect is verified, since the current fluctuation in the higher level, ΔI1 = 7 nA, is more significant than the current swings in the lower level, ΔI2 = 4 nA (see Figure 46b).

Similarly, the estimated equivalent resistances states values are obtained by the relation between the applied voltage and the well-defined current levels approximated in Figure 46: $I_{EMP/EMP}$ = 3.1 nA, $I_{EMP/OCC}$ = 2.8 nA, $I_{OCC/EMP}$ = 2.805 nA, and $I_{OCC/OCC}$ = 2.1 nA. The equation system composed of the four possible states derived of (8) is numerically solved. Please note that, again, multiple solutions exist. Values presented in the Solution 1 of Table II, with a mean error εM = 1 $\mu\Omega$, are the ones used to fit data to model, which does not mean they are better than the other possible solutions. From the aforementioned process, we obtained two possible solution intervals: one showing ΔR_{P1} = ($R_{P1.OCC}$/$R_{P1.EMP}$) > ΔR_{P2} = ($R_{P2.OCC}$/$R_{P2.EMP}$)) and other considering ΔR_{P2} > ΔR_{P1}. Even though a unique solution set is impossible, we remark that in this case, ΔR_{P1} and ΔR_{P2}, present similar orders of magnitude in the two counterpart intervals. Also, the algorithm always converges to the same Rs. From the extracted parameter it was possible to plot the I-t fitting curve, see Figure 47, that corresponds in terms of amplitude fluctuation to the experimental data observed in Figure 46 making T_{P2} emission/capture time constants (165 ms/ 66 ms) greater than T_{P1} ones (3 ms/ 16 ms).

Figure 46 – (a) Experimental Anomalous RTN in a TMOxRAM-based sample under a constant applied voltage of 100 mV and (b) the respective current discrete levels.

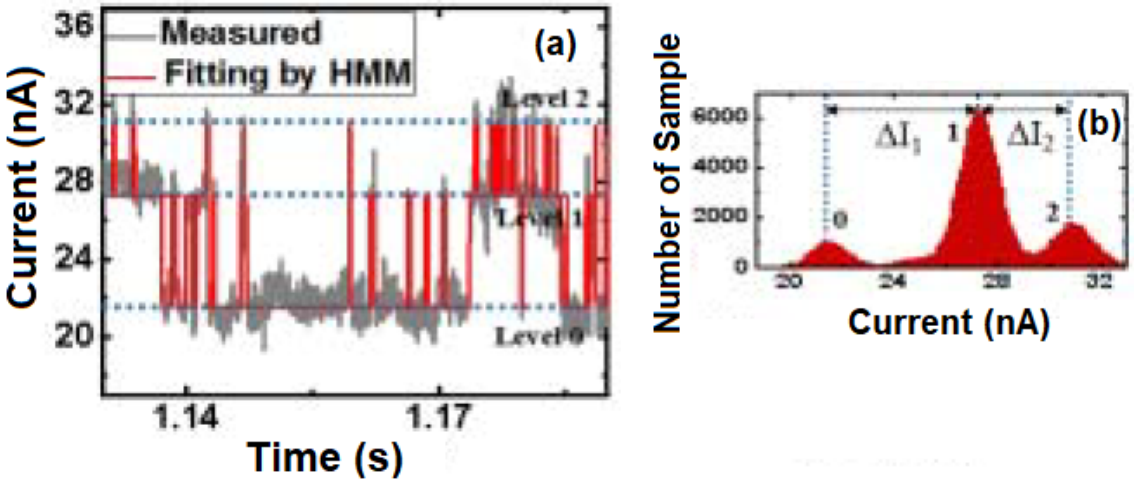

Source: Adapted of Gong et al., (2018).

Table 2 – Solution Parameters for Anomalous RTN in a TMOxRAM-based sample.

Parameter	**Solution 1**	**Solution 2**
Rs	2.61 MΩ	2.61 MΩ
$R_{P1.EMP}$	1.74 MΩ	963 kΩ
$R_{P1.OCC}$	4.46 GΩ	5.15 MΩ
$R_{P2.EMP}$	957 KΩ	1.72 MΩ
$R_{P2.OCC}$	2.15 MΩ	2.63 GΩ

Figure 47 – Parallel Coupled Traps Model current fitting that corresponds, in terms of amplitude fluctuation, to the experimental data observed in Figure 46.

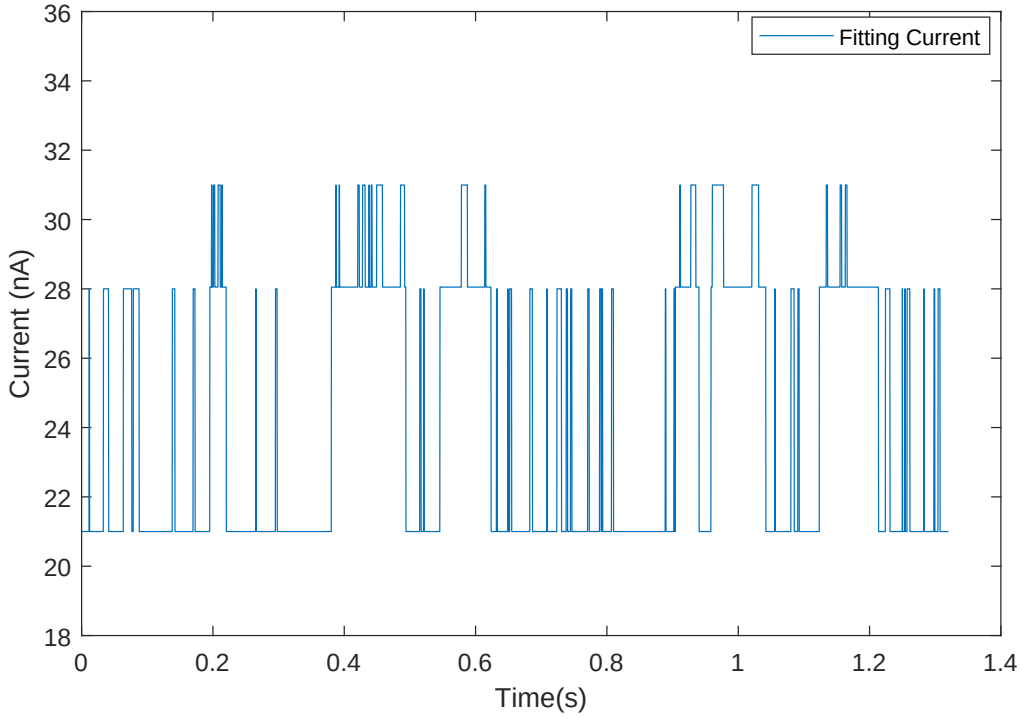

Source: The Author.

7 GIANT RTN

In this chapter, a novel observation of giant random conductance flutuations in MIM-like RS devices is presented. These fluctuations of up to 3 orders of magnitude strongly resemble RTN in RS devices based on TiO_2, HfO_2 and hexagon boron nitide (h-BN) under reading voltages ($\sim$ 0.1 V). These events appeared reproducible for all the aforementioned RS device types in sequential measurements and under different bias conditions. This behavior is very beneficial to ensure recognition of the device's two-state in applications such as stochastic computing integrated circuits (ICs).

Initially, we set the Ni/TiO_2/Au devices using a current compliance (CC) of 30 μA, and the conductance over time was recorded for 2000 seconds. As Figure 48 shows, the conductance swings multiple times by 3 orders of magnitude between two well-defined levels in consecutive measurements (blue, black and yellow, respectively) under a constant bias of 200 mV, for Device 1, and by tuning the applied voltage, for Device 2, under 100 mV (in blue) and 50 mV (in black and green). This consistent behavior indicates that the same structure and the same defects exist during all measurements for the same device. Also, monitoring the conductance magnitude at its higher conductance level (HCL), we remark that their maximum and stable value, 150 μS for Device 1 and 140 μS for Device 2, are higher than the Quantum Conductance constant, G_0 = 77.5 μS, highlighted with the horizontal dashed red line in Figure 48 (LONG *et al.*, 2013; ZHU *et al.*, 2019). This is a strong evidence that the charge transport in HCL is produced by the formation of an effective conductive nanofilament (CNF) across the TiO_2 film, and that during the least conductive level (LCL) the filament is interrupted.

So far, all the RTN current signals across MIM-like devices did not exhibit reversible conductance fluctuations of orders of magnitude for HCL $> G_0$ at reading voltages (AMBROGIO *et al.*, 2014; IELMINI; NARDI; CAGLI, 2010; RAGHAVAN *et al.*, 2013; PUGLISI *et al.*, 2018; YI *et al.*, 2016). It is important to remark that observations of fluctuations of the order of G_0 were already presented (Raghavan et al., 2013 and Yi et al., 2016). In such cases, however, the substantial conductance variations (> 20 %) happened in the range of ten nanoamperes (RAGHAVAN *et al.*, 2013), which correspond to a HCL in the order of 100 nS for the applied reading voltage: 0.1 V; and the conductance

jumps presented in YI *et al.* (2016), in reading operation, do not present a RTN behavior, i.e., reversible jumps of conductance.

Figure 48 – Giant experimental conductance fluctuation in TiO_2 based samples, Device 1, under a constant applied voltage of 200 mV and, Device 2, under 100 mV (in blue) and 50 mV (in black and green) reading voltage. The HCL in each measurement is reproducible and surpasses the G_0 magnitude (in red).

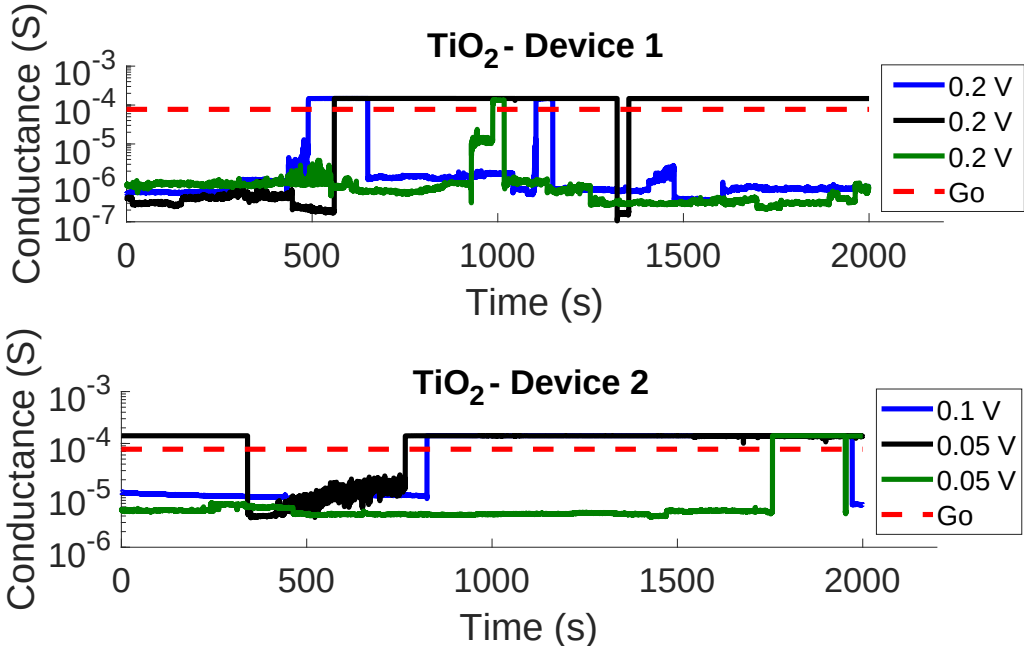

Source: The Author.

In Figure 49a, we present the typical conductance behavior for a HfO_2-based sample, under 25mV (in blue) and 100 mV (in orange) bias voltages. After imposing a SET with CC = 100 μA, the curves demonstrate the giant conductance fluctuations between the same well-defined levels, several times, for both applied voltages. The HCL, 826.7 μS, measured in Figure 49a also surpasses G_0. The behavior presented in Figure 49a was reproducible and the extracted time constants required to swing from HCL/LCL to LCL/HCL fit well with an exponential distribution, as presented in Figure 49b and Figure 49c. The average values of the emission times (τ_e) for the 25 mV and 100 mV curves are 550 ms and 517 ms, respectively, and the average values for the capture times (τ_c) for the 25 mV and 100 mV curves are 115 ms and 46.7 ms, respectively.

A corresponding behavior was also recorded for h-BN-based samples. In Figure 50a, we exemplify the conductance behavior for a h-BN-based sample, under 50 mV and 200 mV. After imposing a SET with CC = 10 μA, the curves demonstrate that the conductance oscillates and recovers to the same well-defined higher-level, several times, under both applied voltages. The behavior presented in Figure 50a was reproducible and the extracted times constants fit well with an exponential distribution, as expected for RTN capture and emission times (Kirton and Uren, 1989). We performed two additional consecutive mea-

Figure 49 – (a) Giant experimental conductance fluctuation with reproducible HCL, recorded for a HfO_2 based sample under 25 mV and 100 mV applied voltages. b) Distribution of the emission times (τ_e) for the RTN signals displayed in panel (a), and c) distribution of the capture times (τ_c) for the RTN signals displayed in panel (a).

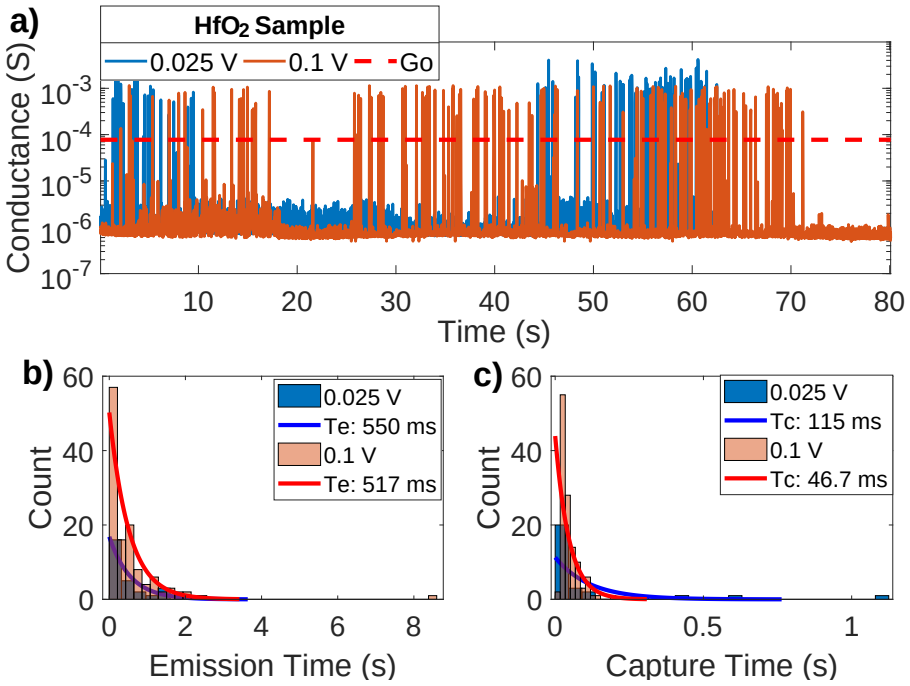

Source: The Author.

surements under 50 mV, in the same sample that displayed the same conductance levels, which are not shown in Figure 50a, in order to obtain sufficient transitions to estimate τ_c and τ_e. The average time to emit (τ_e) for the 50 mV and 200 mV curves are 24.3 ms and 22.7 ms (respectively), Figure 50b, shows that the average time to capture (τ_c) for the 25 mV and 100 mV curves are 42.7 ms and 10.2 ms (respectively), Figure 50c. Regarding the current compliance, we did not find any correlation between this parameter and the RTN amplitudes. We have also measured giant conductance fluctuations in h-BN samples surpassing G_0 up to 2 orders of magnitude, illustrated in Figure 51. Considering this behavior has been recorded for three different switching materials, we show this is a quite general phenomenon and this significant on/off ratio at reading voltage is reproducible and beneficial to ensure recognition of device's two-state in applications such as stochastic computing ICs.

In RAGHAVAN *et al.* (2013), the conductance fluctuations are explained in two different regimes: the surface-relaxation model (IELMINI; NARDI; CAGLI, 2010; AMBROGIO *et al.*, 2014; PUGLISI *et al.*, 2018), normally used to describe RTN in the low resistance state (LRS), and by the geometrical modification of the conductive filament (CF) by defect displacement. We adopted the surface relaxation model to qualitatively explain our results, as it is very unlikely that a significant number of atomic displacements

Figure 50 – Giant experimental conductance fluctuation with reproducible HCL, recorded for a) a h-BN based sample under 50 mV and 200 mV applied voltages. b) Distribution of the time intervals at low current state (τ_e) for the RTN signals displayed in panel (a), and c) distribution of the time intervals at high current state (τ_c) for the RTN signals displayed in panel (a).

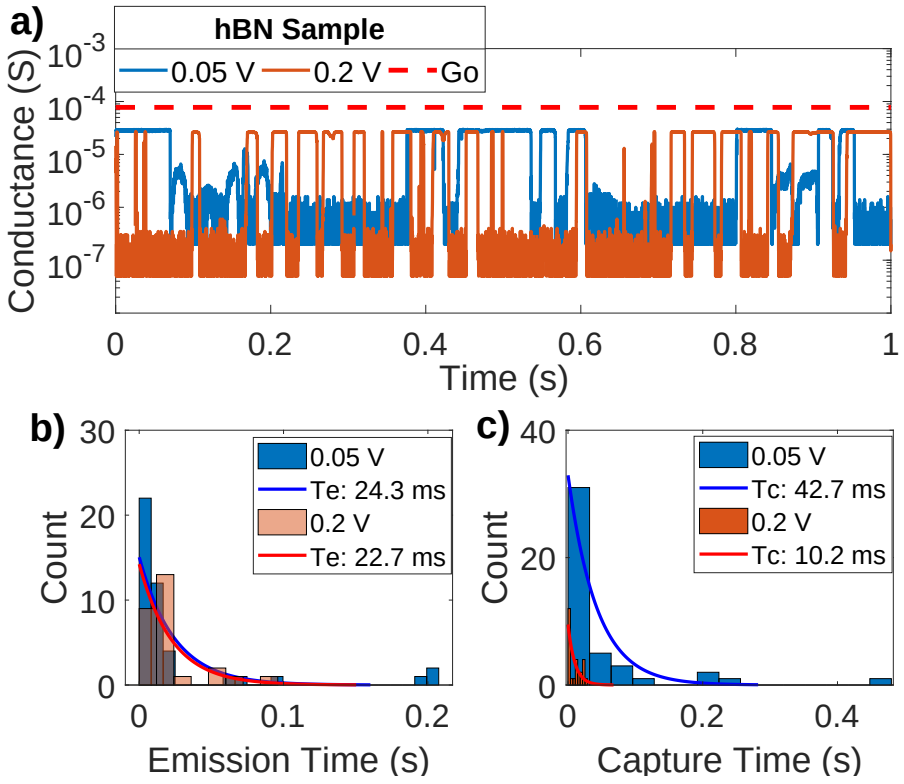

Source: The Author.

Figure 51 – Giant experimental RTN in a h-BN based sample under a constant 50 mV applied voltage, afer SET with CC = 10 μA. The HCL of 5.7 mS is reproducible and surpasses the G_0 magnitude (in red).

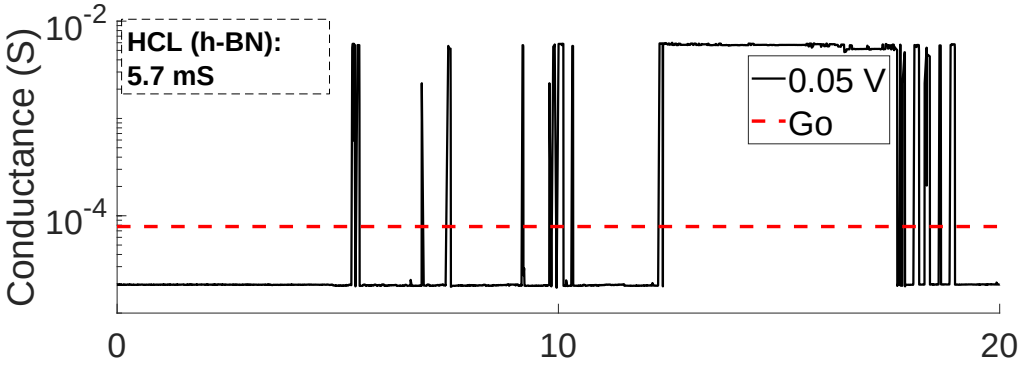

Source: The Author.

would reproduce, several times, the same measured HCLs, especially in the context of Figure 49 and Figure 51, where the reported HCLs are orders of magnitude larger than G_0. Also, the exponential distribution of time constants, presented in Figure 49 and Figure

50, is a strong indication that the described behavior correspond to trapping-detrapping of electrons (KIRTON; UREN, 1989). The model accounts for a partial or total depletion by defect relaxation at the CF surface, and elucidate the size dependent RTN in NiO RRAM (IELMINI; NARDI; CAGLI, 2010), Cu-based RRAM (SONI *et al.*, 2010), HfO_x-RRAM (AMBROGIO *et al.*, 2014; PUGLISI *et al.*, 2018) and the resistance drift in GeS_2 CBRAM (CHOI *et al.*, 2012). However, in these studies, conductance fluctuations of orders of magnitude do not appear when HCL $>$ G_0. These cells share the localized transport in the nanoscaled CF, which governs the switching mechanism in our measured samples.

Our observations occur all after SET, so we assumed a simplified cylindrical CF with length L and diameter D, resulting in a CF resistance R = ρL/Seff$_{UF}$, where ρ is the filament bulk resistivity, and Seff$_{UF}$ is the CF cross-section in a uniform filament (see Figure 52a). For the h-BN samples, at the device level, using compliance currents in the μA-mA range, the CF is inferred to be metallic in nature due to ion migration from the active electrode (Ranjan et al., 2018). Also, our TiO_2- and HfO_2-based samples displayed a non-polar behavior, which is also related to the metallic filament characteristic (LIN *et al.*, 2011; CORTESE *et al.*, 2016). Through this, as the active metal electrode of the measured samples is composed of Nickel, we consider its resistivity value of 250 $\mu.\Omega$.cm that was found for small Ni nanowires, with diameters between 12 nm and 16 nm (DAVYDOV *et al.*, 1998), knowing that for thinner filaments the resistivity should be even higher.

The aforementioned measurements are consistent with the fully depleted filament by the surface defect (see Figure 52a), thus obeying the bulk model of resistance change, ΔR, with $\Delta R \simeq R$ and the effective cross-section change, ΔS, being similar to Seff$_{UF}$ (Ielmini et al., 2010). In this case, the filament diameter, D, is consistent with a Debye length, λ_D, describing the screening in a CF, given by the equation $\lambda_D = (\epsilon kTq^{-2}n^{-1})^{1/2}$, where ϵ is the CF dielectric constant, k is the Boltzmann's constant, T is the temperature, q is the elementary charge, and n is the carrier density. In TiO_2 and HfO_2, the dielectric thickness is L = 5 nm, whereas in h-BN samples it is L = 4 nm. Assuming a relative dielectric constant of 27 for HfO_2, 60 for TiO_2, and 3.8 for h-BN (HUANG *et al.*, 2013; VENICA *et al.*, 2016) and n = 1x10^{19} cm^{-3} the λ_D are estimated considering: i) for TiO_2: S = 1.85x10^{-18} m^2, D = 1.53 nm, and λ_D = 2.79 nm; ii) for HfO_2: S = 1x10^{-17} m^2, D = 3.63 nm, and λ_D = 1.87 nm; and (iii) for h-BN S = 4.26x10^{-19} m^2, D = 0.8 nm, and λ_D = 0.7 nm. The estimated D and λ_D have similar orders of magnitude.

Finally, giant RTN fluctuations characterized by relative conductance variations of up to 50 $\%$ clearly point to the existence of weak links with small effective cross-sectional areas (Seff$_{WF}$) along the conducting paths (SONI *et al.*, 2010). Thus, the model is also applied to distinct filament arrangements, fully depleted by a defect activity in the vicinity of its weaker (narrow) part, Seff$_{WF}$, with similar magnitude to Seff$_{UF}$ in thinner cylindrical filaments, as presented in Figure 52b.

Figure 52 – Trapping activity in the vicinity of a filament, in LRS, which locally reduce or increase the CF's conductivity, by a Coulombian screening effect a) in an uniform filament and b) in the thinner section of a filament.

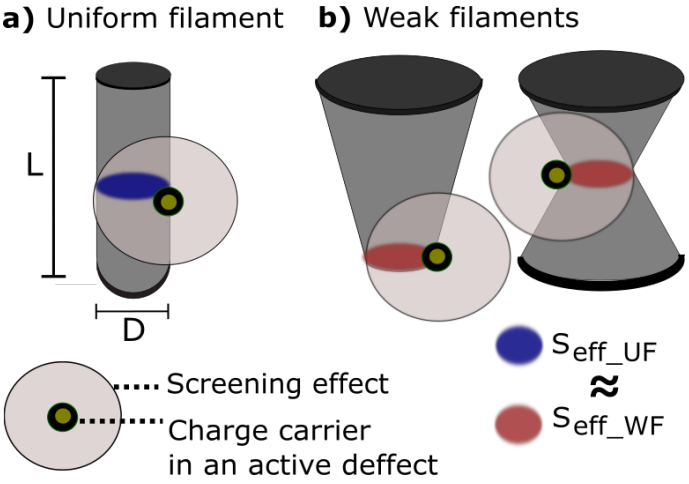

Source: The Author.

8 FINAL REMARKS

In this work, the electrical characterization and modeling of MIM-like RS devices is carried out. Investigation of device behavior is performed including resistive switching memories based on metal oxides (TiO_2- and HfO_2-based samples) and on two-dimensional (2D) material (h-BN).

In this context, the simplest possible electric model that captures the essence of defect coupling in a percolation path is presented. This minimalist model correctly reproduces the experimental observations and many common data in the literature. The model refines the understanding of RTNs in MIM-like RS devices, asserting the existence of a coupling effect among multiple traps.

Additionaly, it is demonstrated that if there are multiple traps along conductive filaments connecting top and bottom electrode, coupling may be observed. Different conductive filaments may be arranged in parallel or in series, due to percolation paths. Traps near these conductive filaments may result in positive coupling effects ($\Delta I_{LOW} > \Delta I_{HIGH}$) if filaments affected by traps are in parallel with each other, or negative coupling effects ($\Delta I_{HIGH} > \Delta I_{LOW}$) if the filaments affected by traps are in series with each other. Experimental RTN traces from RS devices with Ni/TiO_2/Au and Ni/h-BN/Au were correctly predicted by the proposed model.

Also, the presented models correctly describe others non-standard RTN patterns, such as Temporary RTN and 3-level RTN, which are extensively reported in the literature. Furthermore, it was also shown that the modeling framework developed is not restricted to the case of two traps and MIM-like RS devices. Anomalous RTN reported in MOSFET and FinFET devices also fit with the modeling assumptions.

In addition, a novel observation related to RTN in MIM-like RS devices is presented, asserting the occurrences of unusual transitions among conductance states that differ by several orders of magnitude , i.e. when small voltages are applied (~ 0.1 V). This phenomenon was measured after SET in h-BN-, TiO_2- and HfO_2-based samples. We verified multiple transitions which have similar characteristics to RTN.

Also, to model the measured Giant RTN signals we adopted an abstraction of Ielmini Relaxation Model (Ielmini et al., 2010), presenting the situation where the CF is cylindri-

cal. The model is still valid for filaments with different shapes, since the Debye Length correspond to the effective cross section of the filament, i.e., the weak links with small effective cross-sectional areas (Seff_{WF}) along the conducting paths.

Overall, the measured data from three different MIM-like RS devices provide strong support for the proposed model. The methodology presented in this work can be applied to study RTN in traditional MOSFETS, emerging technologies (such as MIM-like RS devices) and advanced CMOS technologies (such as FinFETs). Finally, our findings represent a big step towards the manufacturing of stochastic ICs based on RTN signals, having important implications in the field of post-silicon electronics.

Future works include to extend the model presented in Chaper 6 embracing the trap coupling effects on the defects time constants. Also, a detailed discussion regarding the correlation between the giant RTN amplitudes presented in Chapter 7 and other parameters (e. g., the SET current compliance) can be investigated.

9 PUBLISHED WORK

BECKER, THALES; LI, XUEHUA; ALVES, PEDRO; WANG, TAO; ZHU, KAICHEN; XIAO, YIPING; WIRTH, GILSON; LANZA, MARIO. An Electrical Model for Trap Coupling Effects on Random Telegraph Noise. **IEEE Electron Device Letters**, v.1, p.1 - 1, 2020.

BECKER, THALES; LI, XUEHUA; MOSER, EDUARDO. ALVES, PEDRO; WIRTH, GILSON; LANZA, MARIO. Resistive Switching Devices Producing Giant Random Telegraph Noise. **IEEE Electron Device Letters**, 2021.

BECKER, THALES EXENBERGER; ALVES, PEDRO AUGUSTO BÖCKMANN; MOSER, EDUARDO PELLIN; WIRTH, GILSON INÁCIO. An Electric-Based Model for Coupling Traps Effect on Random Telegraph Noise. **JICS. Journal of Integrated Circuits and Systems**, v.15, p.1 - 4, 2020.

DA SILVEIRA, CLAUDIA THEIS; EXENBERGER BECKER, THALES; BOCKMANN ALVES, PEDRO AUGUSTO; INACIO WIRTH, GILSON. Implementation and Comparison of Algorithms for the extraction of RTN Parameters. In: **2021 35th Symposium on Microelectronics Technology and Devices (SBMicro)**. Campinas, p. 1.

REFERENCES

AMBROGIO, S. *et al.* Statistical fluctuations in HfO x resistive-switching memory: part ii?random telegraph noise. **IEEE Transactions on Electron Devices**, [S.l.], v. 61, n. 8, p. 2920–2927, 2014.

AMBROGIO, S. *et al.* Noise-induced resistance broadening in resistive switching memory?Part II: array statistics. **IEEE Transactions on Electron Devices**, [S.l.], v. 62, n. 11, p. 3812–3819, 2015.

ASENOV, A. *et al.* Increase in the random dopant induced threshold fluctuations and lowering in sub-100 nm MOSFETs due to quantum effects: a 3-d density-gradient simulation study. **IEEE Transactions on Electron Devices**, [S.l.], v. 48, n. 4, p. 722–729, 2001.

ASWATHY, N.; SIVAMANGAI, N. Future Nonvolatile Memory Technologies: challenges and applications. *In*: INTERNATIONAL CONFERENCE ON ADVANCES IN COMPUTING, COMMUNICATION, EMBEDDED AND SECURE SYSTEMS (ACCESS), 2021., 2021. **Proceedings [...]** [S.l.: s.n.], 2021. p. 308–312.

BALATTI, S. *et al.* Voltage-dependent random telegraph noise (RTN) in HfO x resistive RAM. *In*: IEEE INTERNATIONAL RELIABILITY PHYSICS SYMPOSIUM, 2014., 2014. **Proceedings [...]** [S.l.: s.n.], 2014. p. MY–4.

BENVENUTI, A. *et al.* Current status and future prospects of non-volatile memory modeling. *In*: INTERNATIONAL CONFERENCE ON SIMULATION OF SEMICONDUCTOR PROCESSES AND DEVICES (SISPAD), 2014., 2014. **Proceedings [...]** [S.l.: s.n.], 2014. p. 5–8.

CHAI, Z. *et al.* Probing the critical region of conductive filament in nanoscale HfO 2 resistive-switching device by random telegraph signals. **IEEE Transactions on Electron Devices**, [S.l.], v. 64, n. 10, p. 4099–4105, 2017.

CHEN, A. Forming voltage scaling of resistive switching memories. *In*: DEVICE

RESEARCH CONFERENCE, 71., 2013. **Proceedings [...]** [S.l.: s.n.], 2013. p. 181–182.

CHEN, C. *et al.* Endurance degradation mechanisms in TiN\Ta2O5\Ta resistive random-access memory cells. **Applied Physics Letters**, [S.l.], v. 106, n. 5, p. 053501, 2015.

CHOI, S. *et al.* Size-dependent drift of resistance due to surface defect relaxation in conductive-bridge memory. **IEEE electron device letters**, [S.l.], v. 33, n. 8, p. 1189–1191, 2012.

CORTESE, S. *et al.* On the origin of resistive switching volatility in Ni/TiO2/Ni stacks. **Journal of Applied Physics**, [S.l.], v. 120, n. 6, p. 065104, 2016.

DA SILVEIRA, C. T. *et al.* Implementation and Comparison of Algorithms for the extraction of RTN Parameters. *In*: SYMPOSIUM ON MICROELECTRONICS TECHNOLOGY AND DEVICES (SBMICRO), 2021., 2021. **Proceedings [...]** [S.l.: s.n.], 2021. p. 1–4.

DAVYDOV, D. *et al.* Nonlithographic nanowire-array tunnel device: fabrication, zero-bias anomalies, and coulomb blockade. **Physical Review B**, [S.l.], v. 57, n. 21, p. 13550, 1998.

FAN, M.-L. *et al.* Single-trap-induced random telegraph noise for FinFET, Si/Ge Nanowire FET, Tunnel FET, SRAM and logic circuits. **Microelectronics Reliability**, [S.l.], v. 54, n. 4, p. 698–711, 2014.

FLEETWOOD, D. M. 'Border traps' in MOS devices. **IEEE transactions on nuclear science**, [S.l.], v. 39, n. 2, p. 269–271, 1992.

FRÖHLICH, K. TiO2-based structures for nanoscale memory applications. **Materials science in semiconductor processing**, [S.l.], v. 16, n. 5, p. 1186–1195, 2013.

GONG, T. *et al.* Classification of three-level random telegraph noise and its application in accurate extraction of trap profiles in oxide-based resistive switching memory. **IEEE Electron Device Letters**, [S.l.], v. 39, n. 9, p. 1302–1305, 2018.

GONG, T. *et al.* Unveiling the switching mechanism of a TaO x/HfO 2 self-selective cell by probing the trap profiles with RTN measurements. **IEEE Electron Device Letters**, [S.l.], v. 39, n. 8, p. 1152–1155, 2018b.

GRASSER, T. Stochastic charge trapping in oxides: from random telegraph noise to bias temperature instabilities. **Microelectronics Reliability**, [S.l.], v. 52, n. 1, p. 39–70, 2012.

GRASSER, T. **Noise in Nanoscale Semiconductor Devices**. [S.l.]: Springer Nature, 2020.

GUAN, B.; LI, J. A compact model for RRAM including random telegraph noise. *In*: IEEE INTERNATIONAL RELIABILITY PHYSICS SYMPOSIUM (IRPS), 2016., 2016. **Proceedings [...]** [S.l.: s.n.], 2016. p. MY–5–1–MY–5–4.

GUO, S. *et al.* Investigation on the amplitude coupling effect of random telegraph noise (RTN) in nanoscale FinFETs. *In*: IEEE INTERNATIONAL RELIABILITY PHYSICS SYMPOSIUM (IRPS), 2018., 2018. **Proceedings [...]** [S.l.: s.n.], 2018. p. P–TX.

GUPTA, V. *et al.* Resistive random access memory: a review of device challenges. **IETE Technical Review**, [S.l.], v. 37, n. 4, p. 377–390, 2020.

HUANG, J.-W. *et al.* The effect of high/low permittivity in bilayer HfO2/BN resistance random access memory. **Applied Physics Letters**, [S.l.], v. 102, n. 20, p. 203507, 2013.

IELMINI, D.; NARDI, F.; CAGLI, C. Resistance-dependent amplitude of random telegraph-signal noise in resistive switching memories. **Applied Physics Letters**, [S.l.], v. 96, n. 5, p. 053503, 2010.

IELMINI, D.; WASER, R. **Resistive switching**: from fundamentals of nanoionic redox processes to memristive device applications. [S.l.]: John Wiley & Sons, 2015.

INTERNATIONAL Roadmap for Devices and Systems: beyond cmos. [S.l.]: IEEE, 2020. 127 p. Disponível em: <https://irds.ieee.org/images/files/pdf/2020/2020IRDS_BC.pdf>. Acesso em: 20 set. 2020.

INTERNATIONAL Roadmap for Devices and Systems: beyond cmos. [S.l.]: IEEE, 2021. 129 p. Disponível em: <https://irds.ieee.org/images/files/pdf/2021/2021IRDS_BC.pdf>. Acesso em: 20 set. 2020.

JAMESON, J. *et al.* Conductive-bridge memory (CBRAM) with excellent high-temperature retention. *In*: IEEE INTERNATIONAL ELECTRON DEVICES MEETING, 2013., 2013. **Proceedings [...]** [S.l.: s.n.], 2013. p. 30–1.

KIRTON, M.; UREN, M. Noise in solid-state microstructures: a new perspective on individual defects, interface states and low-frequency (1/?) noise. **Advances in Physics**, [S.l.], v. 38, n. 4, p. 367–468, 1989.

LANZA, M. *et al.* Recommended methods to study resistive switching devices. **Advanced Electronic Materials**, [S.l.], v. 5, n. 1, p. 1800143, 2019.

LEE, J.-K. *et al.* Extraction of trap location and energy from random telegraph noise in amorphous TiO x resistance random access memories. **Applied Physics Letters**, [S.l.], v. 98, n. 14, p. 143502, 2011.

LEE, M.-J. *et al.* A fast, high-endurance and scalable non-volatile memory device made from asymmetric Ta 2 O 5- x/TaO 2- x bilayer structures. **Nature materials**, [S.l.], v. 10, n. 8, p. 625–630, 2011.

LI, K.-S. *et al.* Utilizing sub-5 nm sidewall electrode technology for atomic-scale resistive memory fabrication. *In*: SYMPOSIUM ON VLSI TECHNOLOGY (VLSI-TECHNOLOGY): DIGEST OF TECHNICAL PAPERS, 2014., 2014. **Proceedings [...]** [S.l.: s.n.], 2014. p. 1–2.

LI, X. *et al.* Random Telegraph Noise in Metal-Oxide Memristors for True Random Number Generators: a materials study. **Advanced Functional Materials**, [S.l.], p. 2102172, 2021.

LIN, K. L. *et al.* Electrode dependence of filament formation in HfO2 resistive-switching memory. **Journal of Applied Physics**, [S.l.], v. 109, n. 8, p. 084104, 2011.

LIU, W. H. *et al.* Triggering voltage for post-breakdown random telegraph noise in HfLaO dielectric metal gate metal-oxide-semiconductor field effect transistors and its reliability implications. **Journal of Applied Physics**, [S.l.], v. 111, n. 2, p. 024101, 2012.

LONG, S. *et al.* Quantum-size effects in hafnium-oxide resistive switching. **Applied Physics Letters**, [S.l.], v. 102, n. 18, p. 183505, 2013.

MCWHORTER, A. L. *et al.* 1/f noise and related surface effects in germanium. , [S.l.], 1955.

OLDHAM, T. R. Switching oxide traps. **International journal of high speed electronics and systems**, [S.l.], v. 14, n. 02, p. 581–603, 2004.

PIRROTTA, O. *et al.* Multi-scale modeling of oxygen vacancies assisted charge transport in sub-stoichiometric TiO x for RRAM application. *In*: INTERNATIONAL CONFERENCE ON SIMULATION OF SEMICONDUCTOR PROCESSES AND DEVICES (SISPAD), 2014., 2014. **Proceedings [...]** [S.l.: s.n.], 2014. p. 37–40.

PUGLISI, F. M.; PAVAN, P. RTN analysis with FHMM as a tool for multi-trap characterization in HfO x RRAM. *In*: IEEE INTERNATIONAL CONFERENCE OF ELECTRON DEVICES AND SOLID-STATE CIRCUITS, 2013., 2013. **Proceedings [...]** [S.l.: s.n.], 2013. p. 1–2.

PUGLISI, F. M. *et al.* Analysis of RTN and cycling variability in HfO 2 RRAM devices in LRS. *In*: EUROPEAN SOLID STATE DEVICE RESEARCH CONFERENCE (ESSDERC), 2014., 2014. **Proceedings [...]** [S.l.: s.n.], 2014. p. 246–249.

PUGLISI, F. M. *et al.* A complete statistical investigation of RTN in HfO 2-based RRAM in high resistive state. **IEEE Transactions on Electron Devices**, [S.l.], v. 62, n. 8, p. 2606–2613, 2015.

PUGLISI, F. M. *et al.* Anomalous random telegraph noise and temporary phenomena in resistive random access memory. **Solid-State Electronics**, [S.l.], v. 125, p. 204–213, 2016.

PUGLISI, F. M. *et al.* Random telegraph noise: measurement, data analysis, and interpretation. *In*: IEEE 24TH INTERNATIONAL SYMPOSIUM ON THE PHYSICAL AND FAILURE ANALYSIS OF INTEGRATED CIRCUITS (IPFA), 2017., 2017. **Proceedings [...]** [S.l.: s.n.], 2017. p. 1–9.

PUGLISI, F. M. *et al.* Random telegraph noise in resistive random access memories: compact modeling and advanced circuit design. **IEEE Transactions on Electron Devices**, [S.l.], v. 65, n. 7, p. 2964–2972, 2018.

QI, J. *et al.* Resistive switching in single epitaxial ZnO nanoislands. **ACS nano**, [S.l.], v. 6, n. 2, p. 1051–1058, 2012.

RAGHAVAN, N. *et al.* Microscopic origin of random telegraph noise fluctuations in aggressively scaled RRAM and its impact on read disturb variability. *In*: IEEE INTERNATIONAL RELIABILITY PHYSICS SYMPOSIUM (IRPS), 2013., 2013. **Proceedings [...]** [S.l.: s.n.], 2013. p. 5E–3.

RANJAN, A. *et al.* Random telegraph noise in 2D hexagonal boron nitride dielectric films. **Applied Physics Letters**, [S.l.], v. 112, n. 13, p. 133505, 2018.

RANJAN, A. *et al.* Conductive atomic force microscope study of bipolar and threshold resistive switching in 2D hexagonal boron nitride films. **Scientific reports**, [S.l.], v. 8, n. 1, p. 1–9, 2018b.

REALOV, S.; SHEPARD, K. L. Random telegraph noise in 45-nm CMOS: analysis using an on-chip test and measurement system. *In*: INTERNATIONAL ELECTRON DEVICES MEETING, 2010., 2010. **Proceedings [...]** [S.l.: s.n.], 2010. p. 28–2.

SAKAMOTO, T. *et al.* Nanometer-scale switches using copper sulfide. **Applied Physics Letters**, [S.l.], v. 82, n. 18, p. 3032–3034, 2003.

SHI, Y. *et al.* Coexistence of volatile and non-volatile resistive switching in 2D h-BN based electronic synapses. *In*: IEEE INTERNATIONAL ELECTRON DEVICES MEETING (IEDM), 2017., 2017. **Proceedings [...]** [S.l.: s.n.], 2017. p. 5–4.

SHI, Y. *et al.* Electronic synapses made of layered two-dimensional materials. **Nature Electronics**, [S.l.], v. 1, n. 8, p. 458–465, 2018.

SIMOEN, E.; CLAEYS, C. L. **Random telegraph signals in semiconductor devices**. [S.l.]: IOP Publishing Bristol, 2016. v. 357.

SONI, R. *et al.* Probing Cu doped Ge 0.3 Se 0.7 based resistance switching memory devices with random telegraph noise. **Journal of Applied Physics**, [S.l.], v. 107, n. 2, p. 024517, 2010.

VALOV, I. *et al.* Electrochemical metallization memories?fundamentals, applications, prospects. **Nanotechnology**, [S.l.], v. 22, n. 25, p. 254003, 2011.

VANDAMME, L. Opportunities and limitations to use low-frequency noise as a diagnostic tool for device quality. In: **proceeding of ICNF 2003 Prague**. [S.l.: s.n.], 2003. p. 735–748.

VEKSLER, D. *et al.* Evaluation of variability and RTN in scaled RRAM. *In*: IEEE INTERNATIONAL INTEGRATED RELIABILITY WORKSHOP FINAL REPORT (IIRW), 2014., 2014. **Proceedings [...]** [S.l.: s.n.], 2014. p. 52–52.

VENICA, S. *et al.* Graphene Base Transistors With Bilayer Tunnel Barriers: performance evaluation and design guidelines. **IEEE Transactions on Electron Devices**, [S.l.], v. 64, n. 2, p. 593–598, 2016.

WANG, R. *et al.* Complex random telegraph noise (RTN): what do we understand? *In*: IEEE INTERNATIONAL SYMPOSIUM ON THE PHYSICAL AND FAILURE ANALYSIS OF INTEGRATED CIRCUITS (IPFA), 2018., 2018. **Proceedings [...]** [S.l.: s.n.], 2018. p. 1–7.

WEDIG, A. *et al.* Nanoscale cation motion in TaO x, HfO x and TiO x memristive systems. **Nature nanotechnology**, [S.l.], v. 11, n. 1, p. 67–74, 2016.

WONG, H.-S. P. *et al.* Metal–oxide RRAM. **Proceedings of the IEEE**, [S.l.], v. 100, n. 6, p. 1951–1970, 2012.

YI, W. *et al.* Quantized conductance coincides with state instability and excess noise in tantalum oxide memristors. **Nature communications**, [S.l.], v. 7, n. 1, p. 1–6, 2016.

ZHANG, J. *et al.* Comprehensive Study on the ?Anomalous? Complex RTN in Advanced Multi-Fin Bulk FinFET Technology. *In*: IEEE INTERNATIONAL ELECTRON DEVICES MEETING (IEDM), 2018., 2018. **Proceedings [...]** [S.l.: s.n.], 2018. p. 17–3.

ZHOU, J. *et al.* Very low-programming-current RRAM with self-rectifying characteristics. **IEEE Electron Device Letters**, [S.l.], v. 37, n. 4, p. 404–407, 2016.

ZHU, K. *et al.* Graphene–boron nitride–graphene cross-point memristors with three stable resistive states. **ACS applied materials & interfaces**, [S.l.], v. 11, n. 41, p. 37999–38005, 2019.

ZIDAN, M. A.; STRACHAN, J. P.; LU, W. D. The future of electronics based on memristive systems. **Nature electronics**, [S.l.], v. 1, n. 1, p. 22–29, 2018.

ANNEX A TRAP COUPLING MODEL SOLUTIONS

A.1 Series Coupling Model ($\triangle$IHigh > $\triangle$ILow)

As discussed in Subsection 6.2.1, the equation system derived from (3) is comprised of the equations described below:

$$\mu R1 = (R_{S1.OCC} + R_{S2.OCC})//R_p$$

$$\mu R2 = (R_{S1.EMP} + R_{S2.OCC})//R_P$$

$$\mu R3 = (R_{S1.OCC} + R_{S2.EMP})//R_P$$

$$\mu R4 = (R_{S1.EMP} + R_{S2.EMP})//R_P$$

Defining ΔR = ΔRHigh - ΔRLow = (μR3 - μR4) - (μR1 - μR2):
ΔR =

$$\frac{(R_{S1.OCC} + R_{S2.EMP}) \cdot R_p}{(R_{S1.OCC} + R_{S2.EMP}) + R_p} - \frac{(R_{S1.EMP} + R_{S2.EMP}) \cdot R_p}{(R_{S1.OCC} + R_{S2.OCC}) + R_p}$$

$$-\frac{(R_{S1.OCC} + R_{S2.OCC}) \cdot R_p}{(R_{S1.OCC} + R_{S2.OCC}) + R_p} + \frac{(R_{S1.EMP} + R_{S2.OCC}) \cdot R_p}{(R_{S1.EMP} + R_{S2.OCC}) + R_p}$$

ΔR =

$$\frac{(R_{S1.OCC} + R_{S2.EMP})}{\frac{(R_{S1.OCC} + R_{S2.EMP})}{R_p} + 1} - \frac{(R_{S1.EMP} + R_{S2.EMP})}{\frac{(R_{S1.OCC} + R_{S2.OCC})}{R_p} + 1}$$

$$-\frac{R_p}{R_p}\frac{(R_{S1.OCC} + R_{S2.OCC})}{\frac{(R_{S1.OCC} + R_{S2.OCC})}{R_p} + 1} + \frac{(R_{S1.EMP} + R_{S2.OCC})}{\frac{(R_{S1.EMP} + R_{S2.OCC})}{R_p} + 1}$$

If $R_P \rightarrow \infty$ (an open circuit), so: ΔR = [($R_{S1.OCC}$ + $R_{S2.EMP}$) − ($R_{S1.EMP}$ + $R_{S2.EMP}$] − [($R_{S1.OCC}$ + $R_{S2.OCC}$) − ($R_{S1.EMP}$ + $R_{S2.OCC}$)] $\rightarrow$ 0. And the equation system is simplified as follows:

$$\mu R1 = (R_{S1.OCC} + R_{S2.OCC})$$

$$\mu R2 = (R_{S1.EMP} + R_{S2.OCC})$$

$$\mu R3 = (R_{S1.OCC} + R_{S2.EMP})$$

$$\mu R4 = (R_{S1.EMP} + R_{S2.EMP})$$

This equation system can be expressed in terms of a linear matrix system:

$$\begin{bmatrix} R_{S1.EMP} & R_{S1.OCC} & R_{S2.EMP} & R_{S2.OCC} \\ 0 & 1 & 0 & 1 \\ 0 & 1 & 1 & 0 \\ 0 & 1 & 1 & 0 \\ 1 & 0 & 1 & 0 \end{bmatrix} \begin{bmatrix} ResistanceLevel \\ \mu R1 \\ \mu R2 \\ \mu R3 \\ \mu R4 \end{bmatrix}$$

The matrix has determinant D = 0, which means that this equation system has infinite solutions. Thus, when ΔR = ΔRHigh - ΔRLow $\rightarrow$ 0, which is the case in the measurement presented in Figure 41, then $R_P \rightarrow \infty$. Also, in this scenario, it is possible to establish ranges (upper and lower bounds) for the other parameters. By defining ΔR_{S1} = $R_{S1.OCC} - R_{S1.EMP}$ and $\Delta R_{S2} = R_{S2.OCC} - R_{S2.EMP}$, the boundaries are: $R_{S1.EMP}$ = [0 to μR2], $R_{S2.EMP}$ = [0 to μR3], $R_{S1.OCC}$ = [ΔR_{S1} to μR2], and $R_{S2.OCC}$ = [ΔR_{S2} to μR3]. In Figure 41c, we got ΔR_{S1} = 3.5 kΩ and ΔR_{S2} = 10 kΩ, μR2 = 118.5 kΩ, and μR3 = 112 kΩ. Thus, the possible solution ranges are $R_{S1.EMP}$ = [0 to 118.5] kΩ, $R_{S2.EMP}$ = [0 to 112] kΩ, $R_{S1.OCC}$ = [3.5 to 118.5] kΩ, and $R_{S2.OCC}$ = [10 to 112] kΩ. Considering this, the experimental I-t curve (Figure 41a) was successfully fitted using our model (Figure 41d) by the presented solution set: $R_P -> \infty$ KΩ, $R_{S1.EMP}$ = 48.5 KΩ, $R_{S1.OCC}$ = 52 KΩ, $R_{S2.EMP}$ = 60 KΩ, and $R_{S2.OCC}$ = 70 KΩ.

From this, when ΔRHigh $\neq$ ΔRLow, as shown in the fit of Figure 43f, we indicate the presence of a parallel path (i.e., R_P is finite and equal to 172,5 kΩ).

Considering the case where a resistance branch increases drastically due to trapping activity, it may also completely block the current flow through the entire branch. In this case a second trap (eventually located downwards or upwards the branch) may have negligible effect on current conduction. When the activity of both traps significantly increases the resistance of a branch, this situation can lead to the apparent transient RTN shown in Figure 43c. In this case, μR1, μR2 and μR3 >> μR4. This condition can be expressed

mathematically as follows:

μR1 $= (\frac{1}{R_{S1.OCC}+R_{S2.OCC}} + \frac{1}{R_P})^{-1}$, μR2 $= (\frac{1}{R_{S1.EMP}+R_{S2.OCC}} + \frac{1}{R_P})^{-1}$, and μR3 $= (\frac{1}{R_{S1.OCC}+R_{S2.EMP}} + \frac{1}{R_P})^{-1} >>$ μR4 $= (\frac{1}{R_{S1.EMP}+R_{S2.EMP}} + \frac{1}{R_P})^{-1}$

As μR1, μR2 and μR3 must be large, so does R_P. Thus, the condition can be simplified as follows:
$(\frac{1}{R_{S1.OCC}+R_{S2.OCC}})^{-1}, (\frac{1}{R_{S1.EMP}+R_{S2.OCC}})^{-1}, (\frac{1}{R_{S1.OCC}+R_{S2.EMP}})^{-1} >> (\frac{1}{R_{S1.EMP}+R_{S2.EMP}})^{-1}$

Thus, $(R_{S1.OCC}+R_{S2.OCC})$, $(R_{S1.EMP}+R_{S2.OCC})$, $(R_{S1.OCC}+R_{S2.EMP}) >> (R_{S1.EMP}+R_{S2.EMP})$.

As μR4 must be much lower than the other resistance levels, then $R_{S1.OCC}$ and $R_{S2.OCC}$ must be orders of magnitude greater than $R_{S1.EMP}$ and $R_{S2.EMP}$. Considering this, the experimental I-t curve (Figure 41c) was successfully fitted using our model (Figure 41e) by the presented solution set: $R_P -> \infty$ Ω, $R_{S1.EMP}$ = 4.8 KΩ, $R_{S1.OCC}$ = 10 MΩ, $R_{S2.EMP}$ = 18 KΩ, and $R_{S2.OCC}$ = 50 MΩ.

In the measurement presented in Figure 43d, all the current levels have the same order of magnitude, but μR1 $\approx$ μR2 $\approx$ μR3 $>$ μR4, which means that the 3 occupied resistance levels are very similar and larger than μR4 (when both traps are empties). This condition is expressed mathematically as follows:

μR1 $= (\frac{1}{R_{S1.OCC}+R_{S2.OCC}} + \frac{1}{R_P})^{-1} \approx$ μR2 $= (\frac{1}{R_{S1.EMP}+R_{S2.OCC}} + \frac{1}{R_P})^{-1} \approx$ μR3 = $(\frac{1}{R_{S1.OCC}+R_{S2.EMP}} + \frac{1}{R_P})^{-1} >$ μR4 $= (\frac{1}{R_{S1.EMP}+R_{S2.EMP}} + \frac{1}{R_P})^{-1}$

The term $\frac{1}{R_P}$ is common in all parameters. Thus, to satisfy μR1 $\approx$ μR2 $\approx$ μR3 $>$ μR4 it is mandatory that $(R_{S1.OCC} + R_{S2.OCC})$, $(R_{S1.EMP} + R_{S2.OCC})$ and $(R_{S1.OCC} + R_{S2.EMP}) >> R_P$ and, at the same time, $R_P \approx$ μR1 $\approx$ μR2 $\approx$ μR3, as in the solution set used to fit data to model in Figure 43f: R_P = 172.5 KΩ, $R_{S1.EMP}$ = 1.4 MΩ, $R_{S1.OCC}$ = 15 MΩ, $R_{S2.EMP}$ = 1.5 MΩ, and $R_{S2.OCC}$ = 15 MΩ.

A.2 Parallel Coupling Trap Model (ΔILow > ΔIHigh)

The solution analysis consists of numerically solving the non-linear equation system derived from (8) described below:

$$\mu R1 = R_S + (R_{S1.OCC} // R_{S2.OCC})$$

$$\mu R2 = R_S + (R_{S1.EMP} // \ R_{S2.OCC})$$

$$\mu R3 = R_S + (R_{S1.OCC} // \ R_{S2.EMP})$$

$$\mu R4 = R_S + (R_{S1.EMP} // R_{S2.EMP})$$

In this scenario, the R_S parameter must be greater than 0 Ω and smaller than μR4, which is the lowest discrete resistance level estimated by $(\frac{V}{\mu 4})$. To find the possible solution sets, considering the measurement presented in Figure 42, the presented equation system was numerically solved by entering in the algorithm a multitude of different initial guesses (x0). The fluxogram of this algorithm is described in Figure 53. Considering the measurement presented in Figure 42, successive iterations are performed to estimate the possible parameters values or intervals. We analyzed the solution histograms of 1000 estimated output resistances. For all these 1000 cases, the mean error of the equation solution was lower than 0.1 Ω, which means at least 5 orders smaller than the lowest resistance parameter estimated. We note that R_S is very stable in all solutions sets, showing no variation in its order of magnitude, while the other parameters presented two possible ranges of solutions. From this analysis, we determine $R_S = 809.037$ kΩ, and two groups of solution sets$_{(1,2)}$ for: $R_{P1.EMP} = [800\text{ k}\Omega \text{ to } 1\text{ M}\Omega]_1$ or $[1.8\text{ M}\Omega \text{ to } 2\text{ M}\Omega]_2$, $R_{P2.EMP} = [380\text{ k}\Omega \text{ to } 390\text{ k}\Omega]_1$ or $[300\text{ k}\Omega \text{ to } 310\text{ k}\Omega]_2$, $R_{P1.OCC} = [10^{5.6}\ \Omega \text{ to } 10^{6.6}\ \Omega]_1$ or $[10^{8.6}\ \Omega \text{ to } 10^{9.6}\ \Omega]_2$, and $R_{P2.OCC} = [10^{8.6}\ \Omega \text{ to } 10^{9.6}\ \Omega]_1$ or $[10^{5.6}\ \Omega \text{ to } 10^{6.6}\ \Omega]_2$.

Figure 53 – Flowchart of the implemented algorithm to found possible solutions sets of the equation system that describes the PCTM model.

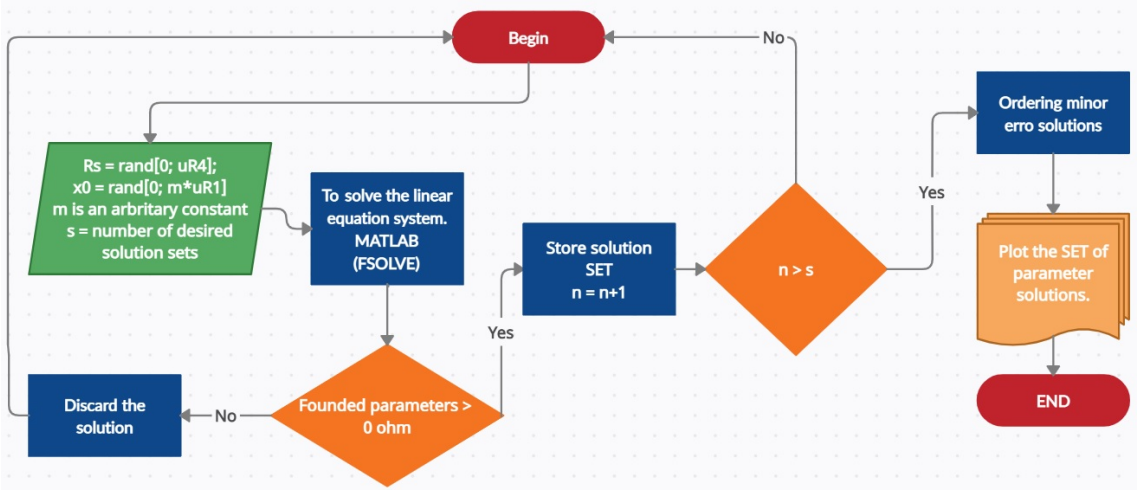

Source: The Author.

Even though is impossible to found a unique solution set, we remark that in this case, $\Delta R_{P1} = (R_{P1.OCC}/R_{P1.EMP})$ and $\Delta R_{P2} = (R_{P2.OCC}/R_{P2.EMP})$ presented similar orders of magnitude in the two counterpart intervals, characterizing the two ranges of possible solutions, as shown in Figure 54.

Finally, we explore the analysis of the temporary RTN signal presented in Figure 43a. In this context, all current levels have the same order of magnitude, but μR1 $>$ μR2 $\approx$

Figure 54 – The logaritm ratio between the occupied and empty states for both resistances parameters (R_{P1} and R_{P2}), considering 30 possible solutions that fit the model to the experimental data measured in Figure 42.

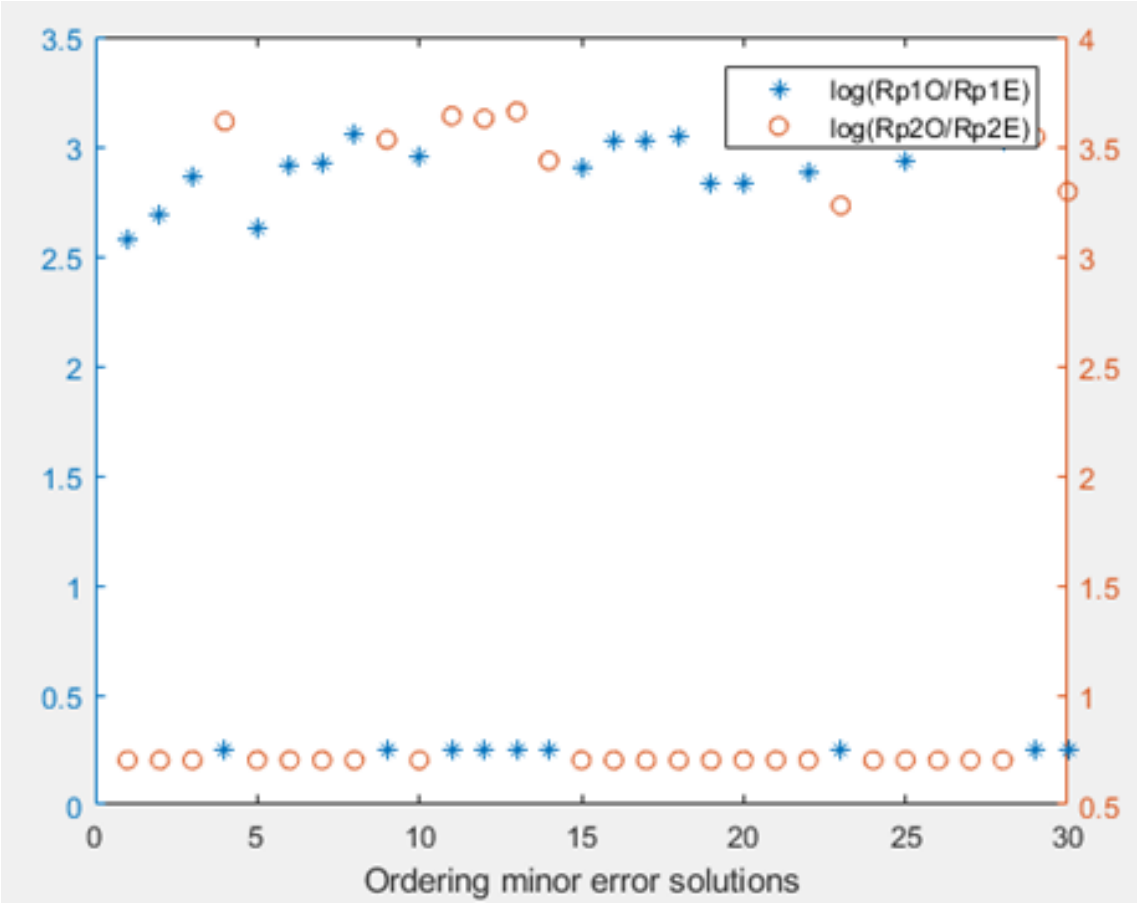

Source: The Author.

μR3 $\approx$ μR4. This condition is expressed mathematically as follows:

$$\mu\text{R1} = (\frac{1}{R_{P1.OCC}} + \frac{1}{R_{P2.OCC}})^{-1} + R_S > \mu\text{R2} = (\frac{1}{R_{P1.EMP}} + \frac{1}{R_{P2.OCC}})^{-1} + R_S \approx \mu\text{R3} = (\frac{1}{R_{P1.OCC}} + \frac{1}{R_{P2.EMP}})^{-1} + R_S \approx \mu\text{R4} = (\frac{1}{R_{P1.EMP}} + \frac{1}{R_{P2.EMP}})^{-1} + R_S.$$

To satisfy those conditions, it is mandatory that $(\frac{1}{R_{P1.EMP}} + \frac{1}{R_{P2.OCC}})^{-1}$, $(\frac{1}{R_{P1.OCC}} + \frac{1}{R_{P2.EMP}})^{-1}$, and $(\frac{1}{R_{P1.EMP}} + \frac{1}{R_{P2.EMP}})^{-1} << \text{R}_S$, so $\text{R}_S \approx \mu\text{R2} \approx \mu\text{R3} \approx \mu\text{R4}$, as in the solution set used to fit data to model (Figure 43b) of the measurement presented in Figure 43a: R_S = 1.82 MΩ, $\text{R}_{P1.EMP}$ = 32 KΩ, $\text{R}_{P1.OCC}$ = 2.28 MΩ, $\text{R}_{P2.EMP}$ = 32 KΩ, $\text{R}_{P2.OCC}$ = 2.44 MΩ.